

VISIBLE LIGHT INDUCED
PHOTOCATALYTIC
DECOMPOSITION OF ODORANT
COMPOUNDS IN DRINKING
WATER

Helen Elizabeth Casey

Ph.D. Thesis

2017

VISIBLE LIGHT INDUCED
PHOTOCATALYTIC
DECOMPOSITION OF ODORANT
COMPOUNDS IN DRINKING
WATER

Helen Elizabeth Casey

*Submitted in partial fulfilment of the
requirements of Manchester Metropolitan
University for the degree of Doctor of*

Philosophy

2017

*School of Science and the Environment
Division of Chemistry and Environmental
Science
Manchester Metropolitan University*

Visible light induced photocatalytic decomposition of odorant compounds in drinking water 1

Contents 2

Abstract 10

Acknowledgements 12

List of Tables 13

List of Figures 15

List of Equations 22

Terms and Abbreviations 24

Part I 27

Background and context 27

Chapter 1 28

Introduction 28

 1.1 Background and motivation 28

 1.2 Research Aim and Objectives 30

 1.3 Thesis structure 31

Chapter 2 34

Taste and odour compounds in drinking water 34

 2.1 Taste and odour compounds 34

2.2 Geosmin and MIB.....	36
2.3 Analytical detection of taste and odour compounds	41
2.3.1 Sensory analysis.....	41
2.3.2 Instrumental analysis.....	42
2.4 Treatment and elimination of geosmin and MIB	50
2.4.1 Treatment resistance and current technology.....	52
2.4.2 Biological treatment.....	57
2.4.3 Physical treatment and chemical oxidation.....	58
Chapter 3.....	62
Photocatalysis	62
3.1 Semiconductors.....	62
3.1.1.Titanium dioxide crystal structure	63
3.2 Titanium dioxide as a photocatalyst.....	64
3.3 Methods of improving photocatalytic activity of titanium dioxide.....	65
Chapter 4.....	69
Thin Films grown via magnetron sputtering.....	69
4.1 Physical vapour deposition	69
4.2 Physical sputtering.....	70
4.2.1 DC sputtering.....	70
4.2.2 Magnetron sputtering.....	71

4.2.3 Magnetron target.....	72
4.2.3 Deposition.....	74
4.3 Thin films.....	75
4.4 Powder targets.....	76
Chapter 5.....	77
Nanoparticles	77
5.1 Nanoparticle uses and overview	77
5.2 Surface plasmon resonance.....	78
5.3 Chemiluminescence	78
5.4 Experimental.....	80
5.4.1 Production of gold nanoparticles	80
5.4.2 Coating of gold nanoparticles.....	81
5.4.3 Production of silver nanoparticles.....	82
5.4.4 Coating of silver nanoparticles	82
5.4.5 Production of luminol doped silica nanoparticles.....	82
5.4.6 Coating of silica with gold nanoparticles.....	83
5.4.7 Production of titanium dioxide nanoparticles	83
5.4.8 Production of nitrogen doped titanium dioxide nanoparticles	84
Part II.....	85
Experimental and analytical techniques.....	85

Chapter 6.....	86
Film production.....	86
6.1 Titanium dioxide films.....	86
6.1.2 TiO ₂ coatings and doped TiO ₂ coatings.....	87
6.1.3 Nitrogen doped titanium dioxide films.....	91
6.1.4 Molybdenum doped titanium dioxide films.....	92
6.1.5 Substrate preparation.....	93
6.2 Powder Coating rig.....	94
6.2.1 Erbium doped titanium dioxide thin films.....	97
6.2.2 Preparation of powder targets.....	97
6.2.3 Operating conditions.....	99
6.2.4 Distance between substrate and target.....	100
Chapter 7.....	103
Analytical Techniques.....	103
7.1 SEM.....	103
7.2 TEM.....	105
7.3 Surface profilometry.....	107
7.4 White light surface profilometry.....	108
7.5 XRD.....	109
7.6 Raman spectroscopy.....	110

7.7 EDX	111
7.8 XPS	112
7.9 ICP-MS	113
7.10 Photocorrelation spectroscopy	114
7.11 Fluorescence spectroscopy.....	115
7.12 Band gap calculation	116
7.13 Photocatalytic testing	117
7.14 GC-MS	121
7.15 Degradation of taste and odour compounds.....	125
Part III	128
Results and Discussion	128
Chapter 8.....	129
Thin film characteristion.....	129
8.1 SEM Results.....	129
8.2 TEM Results	138
8.3 Surface profilometry results.....	139
8.4 Comparison of deposition rates for the teer and powder sputtering rigs	143
8.5 White light surface profilometry results	145
8.6 XRD results.....	153
8.7 Raman results.....	155

8.8 EDX Results.....	159
8.9 ICP Results.....	159
8.10 XPS Results	163
8.11 Band gap calculation.....	165
8.12 Conclusion	170
Chapter 9.....	173
Nanoparticle results	173
9.1 UV-VIS results.....	173
9.2 photon correlation spectroscopy results.....	175
9.2 Concentration of nanoparticles	177
9.3 Luminol doped silica nanoparticles and coating of luminol doped silica with gold nanoparticles	180
9.4 Fluorescent spectroscopy results for Luminol doped silica nanoparticles	181
9.5 Titanium dioxide nanoparticles and N-doped nanoparticles.....	183
9.6 SEM Results.....	184
9.7 Conclusion	185
Chapter 10.....	187
Photocatalysis Results.....	187
10.1 Photocatalytic activity results	187
10.2 TiO ₂ results	190

10.3 N- TiO ₂ results	191
10.4 Er- TiO ₂ results	192
10.5 Conclusion	197
Chapter 11	198
GC-MS Analysis and the degradation of geosmin and MIB Results.....	198
11.1 Geosmin retention time.....	198
11.1.1 Geosmin calibration.....	200
11.2 MIB Retention time	201
11.2.1 MIB calibration.....	203
11.3 Reproducibility of method	203
11.4 Effect of UV light treatment	204
11.5 Effect of UV and visible light with TiO ₂ treatment	206
11.6 Degradation of geosmin with TiO ₂ and n- TiO ₂ results	207
11.6.1 Degradation of MIB with TiO ₂ and n- TiO ₂ results	212
11.7 Degradation of geosmin using uv light and Er- TiO ₂ results	215
11.7.1 Degradation of geosmin using visible light and Er- TiO ₂ results.....	217
11.7.2 Degradation of MIB using UV and Er- TiO ₂ results.....	219
11.7.3 Degradation of MIB using visible light and Er- TiO ₂ results.....	220
11.8 Possible degradation pathway and mechanism	223
11.9 Testing of real reservoir samples	227

11.10 Conclusion	229
Part IV	230
Conclusions and future work	230
Chapter 12.....	231
Conclusions.....	231
12.1 Summary of completed work.....	231
12.2 Overall conclusions.....	232
12.3 Future work.....	234
References.....	235

Geosmin and 2-methylisoborneol (MIB) are two taste and odour causing compounds commonly encountered in drinking water. The analytical identification and quantification of these important taste and odour compounds is required since they affect the organoleptic properties of drinking water and therefore the consumer perception and acceptability of drinking water. This thesis provides an up-to-date summary of analytical techniques for their identification and quantification. Furthermore, recent developments in the elimination of these target compounds are overviewed; conventional treatment methods such as coagulation, sedimentation, filtration and chlorination are ineffective and alternative successful methods are being sought. There is potential for new elimination technology to be implemented into water treatment facilities due to consumer demand.

TiO₂ thin films were produced from a magnetron sputtering technique, along with N-TiO₂, Mo-TiO₂ and Er-TiO₂. All The films were characterised in terms of structure and composition using Scanning electron microscopy (SEM), Raman spectroscopy, X-ray diffraction (XRD), ultraviolet–visible spectroscopy (UV-Vis), X-ray photoelectron spectroscopy (XPS), energy-dispersive X-ray spectroscopy (EDX) and surface profilometry. Nitrogen-doped titania (N-TiO₂) photocatalytic thin films were prepared by reactive magnetron sputter deposition. Nitrogen doping was achieved by the introduction of nitrogen gas as an additional reactive gas during sputtering. There was a distinctive shift of the absorption band in the N-TiO₂ to longer visible regions of the electromagnetic spectrum. The photocatalytic performance was

evaluated by mineralisation of geosmin and MIB. XPS revealed that 1% nitrogen doping resulted in reduction of the band gap energy, enabling 80% degradation of geosmin and MIB under visible light irradiation in 150 minutes. Titanium dioxide nanoparticles and titanium dioxide nanoparticles doped with nitrogen were produced via a sol gel method for direct comparison with the thin films to break down the T&Os, unfortunately many issues arise with using nanoparticles in drinking water treatment as the nanoparticles can leach into the water. A series of erbia doped titania (Er-TiO₂) thin films photocatalysts were also deposited by powder magnetron sputtering method, this material has never been produced before. Erbia powder precursor ranging from 5 to 12.5 % were used to dope the titania films. The amount of erbia present in the TiO₂ thin film was determined using inductively coupled plasma mass spectrophotometry (ICP-MS). Raman spectroscopy showed that the films were not crystalline and the broad peak positions obtained corresponded to a mixture of anatase and brookite crystalline forms. XPS analysis revealed that erbium was present in the form of an oxide. The experiments demonstrated that geosmin and 2-MIB in aqueous solutions was successfully degraded under visible light (> 450 nm) using Er-TiO₂. The results demonstrate successful degradation of geosmin and MIB. These results show the feasibility of utilising the magnetron sputtering technique to grow films for industrial applications in new solar powered elimination technology for implementation in water treatment facilities.

Firstly, I would like to thank my project supervisors; Prof. Peter Kelly for providing support, guidance and help throughout the past 4 years of the project. I would also like to thank Dr. Mike Dempsey, Dr. Debra Whitehead and Prof. Craig banks for their help during the project.

I would like to thank the sponsoring partners EPSRC and United Utilities, for providing the funding for the project and to the NEXUS open access programme for providing use of XPS. I would also like to thank the graduate school for awarding the funding to travel to and present at, my first international conference.

I would like to thank the analytical team at Manchester Met; Dr Hayley Andrews for training me on the SEM and providing Raman spectroscopy, and Lee Harman for training me on the GC-MS and providing XRD.

I would also like to thank my fellow PhD students in both the lab and the office; I was lucky enough to work in a brilliant office with a wide variety of subject specialism leading to a great support network.

I would finally like to dedicate my thesis to my fiancé and my family. Thank you to my parents for their unconditional love and continued support throughout my university years and to my brother and sister for always being there for me. Finally, to my fiancé Ed, thank you for giving me continuous encouragement and support throughout the project.

LIST OF TABLES

TABLE 1: CHARACTERISTICS OF EARTHY ODORANTS; ADAPTED FROM REFERENCE [11].	37
TABLE 2: OVERVIEW OF THE REPORTED ANALYTICAL TECHNIQUES USED FOR THE DETECTION OF GEOSMIN AND MIB.	48
TABLE 3: REMOVAL OF TASTE AND ODOUR COMPOUNDS BY CONVENTIONAL TREATMENT (COAGULATION + FILTRATION AND CHLORINATION) IN THE UK. TAKEN FROM REFERENCE [24].	52
TABLE 4: SUMMARY OF THE TREATMENT OPTIONS TO ELIMINATE MIB AND GEOSMIN.....	55
TABLE 5: TITANIUM DIOXIDE THIN FILM SAMPLES PRODUCED.....	91
TABLE 6: N-DOPED TITANIUM DIOXIDE COATINGS PRODUCED.....	92
TABLE 7: MOLYBDENUM DOPED TITANIUM DIOXIDE COATINGS PRODUCED.....	93
TABLE 8: ATOMIC PERCENT RATIO OF THE DOPANTS FOR THE TiO ₂ : ER POWDER TARGETS.....	98
TABLE 9: THE TOTAL MASS OF THE BLENDED POWDER TARGETS.....	99
TABLE 10: INDIVIDUAL RUN CONDITIONS FOR ERBIA DOPED TITANIUM DIOXIDE FILMS.....	101
TABLE 11: GC-MS CONDITION PARAMETERS.....	124
TABLE 12: THIN FILM THICKNESS RESULTS	140
TABLE 13: ERBIUM FILM RUN CONDITIONS.....	142
TABLE 14: CALCULATION OF DEPOSITION RATES PER KW OF POWER USED.....	144
TABLE 15: THIN FILM SURFACE ROUGHNESS AND SURFACE AREA RESULTS.....	147
TABLE 16: ICP RESULTS FOR AMOUNT OF MO IN FINAL FILM	162
TABLE 17: ICP RESULTS FOR AMOUNT OF ER IN FINAL FILM COMPARED TO STARTING TARGET	162

TABLE 18: BAND GAP VALUES	170
TABLE 19: PHOTON CORRELATION SPECTROSCOPY RESULTS OF NANOPARTICLES PRODUCED, GOLD AND GOLD COATED IN SILICA AND SILVER AND SILVER COATED IN SILICA	177
TABLE 20: FLUORESCENCE SPECTROSCOPY RESULTS FOR LUMINOL DOPED SILICA	182
TABLE 21: COMPARISON OF RATE CONSTANTS FOR THE DECOMPOSITION OF METHYLENE BLUE..	196
TABLE 22: DEGRADATION RESULTS FOR GEOSMIN AND MIB UNDER UV AND VISIBLE LIGHT	206
TABLE 23: PERCENTAGE GEOSMIN DEGRADATION FOR TIO ₂ AND N-TIO ₂	209
TABLE 24: PERCENTAGE DEGRADATION OF MIB FOR TIO ₂ AND N-TIO ₂	213
TABLE 25: PERCENTAGE DEGRADATION OF GEOSMIN UNDER UV LIGHT FOR ER-TIO ₂ THIN FILMS .	216
TABLE 26: PERCENTAGE DEGRADATION OF GEOSMIN UNDER VISIBLE LIGHT FOR ER-TIO ₂ THIN FILMS	218
TABLE 27: COMPARISON OF RATE CONSTANTS FOR THE DEGRADATION OF GEOSMIN USING VARIOUS THIN FILMS UNDER UV AND VISIBLE LIGHT.....	222
TABLE 28: COMPARISON OF RATE CONSTANTS FOR THE DEGRADATION OF MIB USING VARIOUS THIN FILMS UNDER UV AND VISIBLE LIGHT	222

LIST OF FIGURES

FIGURE 1: TASTE AND ODOUR WHEEL ³	35
FIGURE 2: SIMPLIFIED PATHWAY FROM THE SOURCE OF GEOSMIN AND MIB TO THE CONSUMER DRINKING WATER.....	38
FIGURE 3: A TIMELINE REPRESENTING THE NUMBER OF GEOSMIN AND MIB RELATED PUBLICATIONS (SOURCE: WEB OF KNOWLEDGE 2016)	40
FIGURE 4: STAGES OF THE DRINKING WATER TREATMENT PROCESS	52
FIGURE 5: ENERGY BANDS IN INSULATORS, SEMICONDUCTORS AND METALS.....	63
FIGURE 6: CRYSTAL STRUCTURE OF A) ANATASE AND B) RUTILE ⁷³	64
FIGURE 7: TITANIUM DIOXIDE PHOTOCATALYSIS	66
FIGURE 8: ATOMIC COLLISION CASCADE DIAGRAM	71
FIGURE 9: SCHEMATIC OF MAGNETRON SHOWING 'RACETRACK' OF EACH TARGET ⁹²	73
FIGURE 10: UNBALANCED AND BALANCED MAGNETRONS ⁶⁶	74
FIGURE 11: REACTION SCHEME SHOWING OXIDATION OF LUMINOL	78
FIGURE 12: CATALYSIS MODEL OF AU NANOPARTICLES IN THE CL REACTION BETWEEN LUMINOL AND AGNO ₃ ⁹⁴	79
FIGURE 13: VARIOUS NANOPARTICLES SYNTHESISED: A) GOLD NANOPARTICLE B) SILVER NANOPARTICLE C) GOLD COATED WITH SILICA NANOPARTICLE D) SILVER COATED WITH SILICA NANOPARTICLE E) SILICA COATED WITH GOLD NANOPARTICLE SEEDS F) LUMINOL COATED WITH SILICA NANOPARTICLES	80

FIGURE 14: MAGNETRON SPUTTERING CHAMBER SET UP PLAN VIEW, TWO TITANIUM TARGETS AND A TARGET FOR TRANSITION METAL DOPANTS, WHEN REQUIRED	87
FIGURE 15: TEER COATINGS LTD. UDP450 MAGNETRON SPUTTERING RIG	88
FIGURE 16: A) INSIDE THE MAGNETRON CHAMBER ARGON GAS ONLY DISCHARGE WITH TI TARGET B) AFTER THE ADDITION OF OXYGEN TO THE ARGON GAS MAGNETRON CHAMBER.....	90
FIGURE 17: SCHEMATIC OF SUBSTRATE PREPARATION TO CREATE A STEP. A) TAPE COVERING PART OF THE SUBSTRATE B)SUBSTRATE AFTER THE DEPOSITION PROCESS C)REMOVAL OF THE TAPE TO CREATES A STEP BETWEEN THE SUBSTRATE AND THIN FILM	94
FIGURE 18: POWDER COATING RIG	95
FIGURE 19: POWDER TARGET, MAGNETRON SPUTTERING CHAMBER SET UP PLAN VIEW	96
FIGURE 20: GLOWING PLASMA INSIDE THE MAGNETRON SPUTTERING CHAMBER DURING DEPOSITION	96
FIGURE 21: SEM SCHEMATIC ⁷⁵	104
FIGURE 22: TEM SCHEMATIC ⁹⁰	106
FIGURE 23: DETAK II INSTRUMENT AT MMU	107
FIGURE 24: WHITE LIGHT SURFACE PROFILOMETRY SCHEMATIC ¹¹¹	109
FIGURE 25: PHOTON CORRELATION SPECTROSCOPY SET UP ¹¹⁵	115
FIGURE 26: SCHEMATIC ILLUSTRATION OF FLUORESCENCE SPECTROMETER	116
FIGURE 27: SCHEMATIC REPRESENTATION OF METHYLENE BLUE TEST	119
FIGURE 28: AGILENT TECHNOLOGIES 7890B INSTRUMENT	122
FIGURE 29: GAS-CHROMATOGRAPHY MASS SPECTROMETRY STRUCTURE ¹¹⁹	123

FIGURE 30: SET UP OF EXPERIMENT TO PHOTOCATYTICALLY DEGRADE T&O COMPOUNDS	126
FIGURE 31: TEST SET UP FOR DEGRADATION OF TASTE AND ODOUR COMPOUNDS.....	127
FIGURE 32: IMAGE OF TiO_2 THIN FILM COATING ON GLASS SUBSTRATE	129
FIGURE 33: SEM IMAGES FOR A) C1 B) C2 C) C3 D) C4 UNDOPED TITANIUM DIOXIDE THIN FILMS..	130
FIGURE 34: SEM IMAGES FOR A) NC1 B) NC2 C) NC3 D) NC4 NITROGEN DOPED TITANIUM DIOXIDE THIN FILMS	131
FIGURE 35: SCANNING ELECTRON MICROSCOPY IMAGES OF A) TiO_2 AND B) N- TiO_2 THIN FILMS....	132
FIGURE 36: SEM IMAGES FOR A) MOC1 B) MOC2 C) MOC3 D) MOC4 MOLYBDENUM DOPED TITANIUM DIOXIDE THIN FILMS.....	133
FIGURE 37: SCANNING ELECTRON MICROSCOPY IMAGES OF A) TiO_2 , B) 5% ER - TiO_2 THIN, C) 7.5% ER- TiO_2 THIN D) 10% ER - TiO_2 THIN AND E) 12.5% ER TiO_2 THIN FILMS.....	135
FIGURE 38: SCANNING ELECTRON MICROSCOPY IMAGES OF A) 5% ER- TiO_2 ON GLASS, B) 5% ER - TiO_2 ON SILICON, C) 12.5% ER - TiO_2 ON GLASS AND D) 12.5% ER - TiO_2 ON SILICON.....	136
FIGURE 39: CROSS SECTION IMAGES OF UNDOPED TiO_2 (C1)	137
FIGURE 40: CROSS SECTIONAL SCANNING ELECTRON MICROSCOPY IMAGES OF A) 7.5% ER- TiO_2 ON GLASS, B) 7.5% ER - TiO_2 ON SILICON, C) 12.5% ER - TiO_2 ON GLASS AND D) 12.5% ER - TiO_2 ON SILICON.	138
FIGURE 41: TEM IMAGE FOR TiO_2	139
FIGURE 42: SURFACE IMAGES FOR A) C1 B) C2 C) C3 D) C4 UNDOPED TITANIUM DIOXIDE THIN FILMS	148
FIGURE 43: SURFACE IMAGES FOR A) NC1 B) NC2 C) NC3 D) NC4 NITROGEN DOPED TITANIUM DIOXIDE THIN FILMS	149

FIGURE 44: SURFACE IMAGES FOR A) MOC1 B) MOC2 C) MOC3 D) MOC4 MOLYBDENUM DOPED TITANIUM DIOXIDE THIN FILMS	151
FIGURE 45: SURFACE IMAGES FOR A) 7.5% ER-TiO ₂ , B) 5% ER -TiO ₂ , C) 12.5% ER -TiO ₂ AND D) 12.5% ER -TiO ₂	152
FIGURE 46: XRD PATTERN FOR C1 TiO ₂ THIN FILM	153
FIGURE 47: OBSERVED XRD PATTERNS FOR TiO ₂ AND N-TiO ₂	154
FIGURE 48: OBSERVED XRD PATTERNS FOR VARIOUS THIN FILMS.....	155
FIGURE 49: RAMAN SPECTRA OF A) TiO ₂ AND B) N-TiO ₂ THIN FILMS.	156
FIGURE 50: RAMAN SPECTRA TAKEN FROM REFERENCE ¹¹² TO SHOW POSITIONS OF TITANIA CRYSTAL PHASES , BLACK: AMORPHOUS TiO ₂ , BLUE: ANATASE TiO ₂ , GREEN: AN/RU TiO ₂ AND RED: RUTILE TiO ₂	157
FIGURE 51: RAMAN SPECTRA OF TiO ₂ AND ER-TiO ₂ THIN FILMS ON GLASS SUBSTRATES.....	158
FIGURE 52: RAMAN SPECTRA OF OF A) ER-TiO ₂ ON DIFFERENT SUBSTRATES AND B) ER -TiO ₂ THIN FILMS ON SILICON.	159
FIGURE 53: TITANIUM ICP CALIBRATION PLOT	160
FIGURE 54: MOLYBDENUM ICP CALIBRATION PLOT	160
FIGURE 55: ERBIUM ICP CALIBRATION PLOT.....	161
FIGURE 56: XPS SPECTRA OF (A) Ti2P PEAKS AND (B) N1S OF TiO ₂ AND N-TiO ₂ THIN FILMS.	163
FIGURE 57: XPS SPECTRA OF (A) Ti2P PEAKS AND (B) ER 4D PEAKS OF TiO ₂ AND ER-TiO ₂ THIN FILMS.	165
FIGURE 58: UV-VIS ABSORPTION SPECTRA FOR TiO ₂ C1	166

FIGURE 59: A)UV–VISIBLE ABSORPTION SPECTRA AND B) TAUC PLOT OF TiO_2 AND N- TiO_2 THIN FILMS.	167
FIGURE 60: A) UV–VISIBLE ABSORPTION SPECTRA AND B) TAUC PLOT OF TiO_2 AND ER- TiO_2 THIN FILMS.	168
FIGURE 61: GOLD AND SILVER NANOPARTICLE SOLUTIONS PRODUCED.....	173
FIGURE 62: UV-VIS ABSORPTION PEAK FOR GOLD NANOPARTICLES.....	174
FIGURE 63: UV-VIS CALIBRATION PLOT FOR AU	174
FIGURE 64: UV-VIS ABSORPTION PEAK FOR SILVER NANOPARTICLES	175
FIGURE 65: UV-VIS CALIBRATION PLOT FOR AG	175
FIGURE 66: EXAMPLE SPECTRA OF GOLD NANOPARTICLE PARTICLE SIZE	176
FIGURE 67: SEM RESULTS FOR A), B) LUMINOL DOPED SILICA C) LUMINOL DOPED SILICA WITH APS AND D) LUMINOL DOPED SILICA WITH GOLD NANOPARTICLES	181
FIGURE 68: FLUORESCENCE RESULTS FOR LUMINOL AND LUMINOL DOPED WITH SILICA AND GOLD NANOPARTICLES.....	182
FIGURE 69: TiO_2 NANOPARTICLES.....	183
FIGURE 70: IMAGES A-D OF THE PARTICLES VARYING IN SHAPE AND SIZE	185
FIGURE 71: DEGRADATION OF METHYLENE BLUE IN THE DARK, UNDER UV AND VISIBLE LIGHT	188
FIGURE 72: METHYLENE BLUE PHOTOCATALYTIC RESULTS FOR TiO_2	190
FIGURE 73: METHYLENE BLUE PHOTOCATALYTIC RESULTS FOR N- TiO_2	191
FIGURE 74: METHYLENE BLUE PHOTOCATALYTIC RESULTS FOR ER 5%- TiO_2	192
FIGURE 75: METHYLENE BLUE PHOTOCATALYTIC RESULTS FOR ER 7.5%- TiO_2	193

FIGURE 76: METHYLENE BLUE PHOTOCATALYTIC RESULTS FOR ER 10%-TiO ₂	194
FIGURE 77: METHYLENE BLUE PHOTOCATALYTIC RESULTS FOR ER 12.5%-TiO ₂	194
FIGURE 78: EXAMPLE GC-MS SPECTRUM FOR GEOSMIN DISSOLVED IN METHANOL AND WATER WITH A CLEAR PEAK AT 10MINUTES	199
FIGURE 79: GEOSMIN PRODUCT IONS CLEAR M/Z 112 PEAK	199
FIGURE 80: GC-MS GEOSMIN CALIBRATION PLOT CONCENTRATION UP TO 2PPM	200
FIGURE 81: GC-MS GEOSMIN CALIBRATION PLOT CONCENTRATION UP TO 2000PPM	201
FIGURE 82: EXAMPLE GC-MS SPECTRUM FOR MIB DISSOLVED IN METHANOL AND WATER WITH A CLEAR PEAK AT 8MINUTES	202
FIGURE 83: MIB PRODUCT IONS CLEAR M/Z 95 PEAK.....	202
FIGURE 84: GC-MS CALIBRATION PLOT FOR MIB CONCENTRATIONS UP TOP 2000PPM	203
FIGURE 85: A GRAPH TO SHOW DEGRADATION OF GEOSMIN IN THE PRESENCE OF UV LIGHT AND TiO ₂	207
FIGURE 86: GEOSMIN % CONCENTRATION DEGRADATION AGAINST TIME FOR TiO ₂ AND N-TiO ₂ ...	208
FIGURE 87: GEOSMIN RATE OF DEGRADATION CALCULATION FOR TiO ₂ AND N-TiO ₂	210
FIGURE 88: COMPARISON BAR CHART OF K _A VALUES FOR THE DEGRADATION OF GEOSMIN FOR TiO ₂ AND N-TiO ₂ THIN FILMS	211
FIGURE 89: MIB %CONCENTRATION DEGRADATION VALUES AGAINST TIME FOR TiO ₂ AND N-TiO ₂	212
FIGURE 90: MIB RATE OF DEGRADATION CALCULATION FOR TiO ₂ AND N-TiO ₂	214
FIGURE 91: COMPARISON BAR CHART OF K _A VALUES FOR THE DEGRADATION OF MIB FOR TiO ₂ AND N-TiO ₂ THIN FILMS.....	214

FIGURE 92: % CONCENTRATION GEOSMIN DEGRADATION VALUES AGAINST TIME FOR ER-TIO ₂ UNDER UV LIGHT.....	215
FIGURE 93: GEOSMIN RATE OF DEGRADATION CALCULATION UNDER UV LIGHT.....	217
FIGURE 94: % CONCENTRATION GEOSMIN DEGRADATION VALUES AGAINST TIME FOR ER-TIO ₂ UNDER VISIBLE LIGHT	218
FIGURE 95: GEOSMIN RATE OF DEGRADATION CALCULATION UNDER VISIBLE LIGHT.....	219
FIGURE 96: MIB RATE OF DEGRADATION CALCULATION UNDER UV LIGHT	220
FIGURE 97: MIB RATE OF DEGRADATION CALCULATION UNDER VISIBLE LIGHT	221
FIGURE 98: CHROMATOGRAM FROM GC-MS.....	224
FIGURE 99: CHROMATOGRAM FROM GC-MS.....	225
FIGURE 100: BREAKDOWN PRODUCTS OF GEOSMIN OBSERVED FROM GC-MS ANALYSIS.....	226
FIGURE 101: MIB REARRANGEMENT OBSERVED FROM GC-MS ANALYSIS	227
FIGURE 102: RESERVOIR WATER SAMPLE BEFORE THE TREATMENT PROCESS.....	228
FIGURE 103: GC CHROMATOGRAM FOR UU UNTREATED WATER	228

$R_a = \frac{1}{N} \sum_{i=1}^N z_i - \bar{z} $	EQ. 1.....	108
$R_{RMS} = \left[\frac{1}{N} \sum_{i=1}^N (z_i - \bar{z})^2 \right]^{1/2}$	EQ.2.....	109
$n\lambda = 2d \sin\theta$	EQ. 3.....	110
$E_k = h\nu - E_b - \Phi$	EQ. 4.....	112
$\alpha h\nu = (h\nu - E_g)^{1/n}$	EQ.5	117
$K_a = \ln(A_0 / A_t)$	EQ. 6.....	121
$V_{cluster} = NV_{atom}$	EQ. 7	177
$4/3\pi (R_{cluster})^3 = N4/3\pi (R_{atom})^3$	EQ. 8.....	177
$R_{cluster} = N^{1/3} R_{atom}$	EQ. 9.....	177
$S_{cluster} = 4\pi (R_{cluster})^2$	EQ. 10	178
$N_s = (4\pi (R_{cluster})^2 / \pi(R_{atom})^2) = 4N^{2/3}$	EQ. 11	178
$N = (R_{cluster}/R_{atom})^3$	EQ. 12	178
$N_s = 4N^{2/3}$	EQ.13.....	178
$M_w = M_{gold} \times N$	EQ. 14	179

$N_{np} = N_{atom} l N$	EQ. 15.....	179
$C_{np} = N_{np} / N_a$	EQ. 16	180
$A = \epsilon c l$	EQ.17	188
$\ln(C_0 / C) K_a t$	EQ.18	188
$K_a = \ln(A_0 / A_t)$	EQ. 19.....	189
$STD = \sum \frac{(x - \bar{x})^2}{(n-1)}$	EQ. 20.....	204
$E = 60 P \eta T$	EQ. 21.....	205
$\ln(C_o / C_t) = kt$	EQ. 22	209

TERMS AND ABBREVIATIONS

<i>A</i>	Surface Area
BE	Binding Energies
<i>C</i>	Concentration
CB	Conduction Band
CVD	Chemical Vapour Deposition
DC	Direct Current
EDX	Energy-Dispersive X-ray spectroscopy
GC	Gas Chromatography
GC-MS	Gas Chromatography Mass Spectrometry
ICP	Inductively Coupled Plasma
LC-MS	Liquid Chromatography Mass Spectrometry
MASE	Membrane Assisted Solvent Extraction

MB	Methylene Blue
MIB	2-Methylisoborneol
OTC	Odour Threshold Concentration
PCS	Photon Correlation Spectroscopy
PTV	Programmed Temperature Vaporization
PVD	Physical Vapour Deposition
PVP	Polyvinylpyrrolidone
SEM	Scanning Electron Microscopy
SPE	Solid Phase Extraction
SPME	Solid Phase Micro-Extraction
SPR	Surface Plasmon Resonance
<i>t</i>	Time
<i>T</i>	Temperature
T&O	Taste and Odour

TEM	Transmission Electron Microscopy
UV/Vis	UltraViolet/Visible light spectrophotometry
VB	Valance Band
VOC's	Volatile Organic Compounds
WFD	Water Framework Directive
XPS	X-Ray Photoelectron Spectroscopy
XRD	X-Ray Diffraction

PART I

BACKGROUND AND CONTEXT

This chapter provides a sound introduction of this study starting with background and motivation of the research, followed by aims and objectives and information on the structure of this thesis.

1.1 BACKGROUND AND MOTIVATION

The project was partially funded by *United Utilities PLC* (UU), they are a company responsible for regulating and managing North West drinking and waste water in England. Taste and odour compounds are of high interest to this water company as there have been various consumer complaints of ‘off flavour’ tap water, at a number of different locations linking to the problem arising at a number of different reservoirs. Additionally to this geosmin and 2-methylisoborneol (MIB) pose a problem to water treatment facilities globally and there are an extensive range of useful analytical techniques which have been developed and applied to real samples. Once identified and detected, the treatment of geosmin and MIB poses a problem due to their resistance to conventional water treatment methods; using titanium dioxide photocatalysis to break down the pollutants in water is a new and promising approach to this field.

Many authors have investigated biological treatment procedures; however, the research concluded that the methods are too costly. In such degradation/elimination studies, researchers usually assume the T&O compounds have been eliminated without

convincing proof such as the use of mass spectrometry. This study focuses on the methods of detection and total removal of geosmin and MIB from drinking water, which would allow drinking water treatment facilities to implement the technology and to ensure they deliver drinking water to a standard acceptable by customers.

TiO₂ was synthesised by two different methods; magnetron sputtering which is a surface engineering technique to produce TiO₂ thin films. a second method of nanoparticle synthesis by a published sol-gel method was also used to produce TiO₂ nanoparticles¹. The addition of dopants was investigated via producing N-TiO₂, Mo-TiO₂, Er-TiO₂ also using magnetron sputtering methods. Characterisation of materials produced utilized the following analytical techniques; Scanning electron microscopy (SEM), Transmission electron microscopy (TEM), Surface profilometry and white light surface profilometry, Raman spectroscopy, X-ray diffraction (XRD), ultraviolet-visible spectroscopy (UV-Vis), X-ray photoelectron spectroscopy (XPS), energy-dispersive X-ray spectroscopy (EDX), ICP and finally GC-MS. Both the doped titania and the regular TiO₂ thin films were tested for photocatalytic properties by recording the photodegradation rate of methylene blue dye under UV and visible light. GC-MS was used to record the degradation of the taste and odour pollutants in water over time and a lab based set up was used to determine the best photocatayst to degrade both geosmin and MIB. Current strategies for water purification include photocatalysis using UV irradiation on a TiO₂ substrate, this method requires electrical energy for the UV lamp². In this thesis the effect of using gold and silver nanoparticles and luminol to cause fluorescence was investigated.

Research Questions:

- What is the most suitable photocatalyst for the degradation of geosmin and MIB?
- Will a magnetron sputtered coating be suitable and effective at breaking down geosmin/MIB under UV and visible light irradiation?
- What methodology can be used for quantitative analysis of geosmin and MIB at the nanogram-per litre level, which is inexpensive, rapid and suitable for laboratory scale-analysis?
- How reproducible are any findings and how suitable are they to up-scale to the drinking water industry?

1.2 RESEARCH AIM AND OBJECTIVES

The main aim of the project is to develop a material to break down geosmin and MIB in drinking water and to develop a method in order to test this breakdown.

Aim: 1: Develop a nanomaterial with photocatalytic properties

Strategy employed:

1. Growth of titanium dioxide thin films by Magnetron Sputtering
2. Growth of N-doped titania thin films by Magnetron Sputtering
3. Growth of Mo-doped titania thin films by Magnetron Sputtering
4. Growth of Er-doped titania thin films by Magnetron Sputtering
5. Growth of N-doped titania nanoparticles by sol gel.

6. Growth of N-doped titania nanoparticles by sol-gel

Aim: 2: Develop a light emitting nanomaterial to initiate photocatalytic degradation of organic drinking water pollutants upon binding.

Strategy employed:

1. Growth of core shell nanoparticles by colloidal synthesis.
2. Testing of luminol as alternative to electrical light

Aim: 3: Develop a way to eliminate and detect geosmin and MIB

Strategy employed:

1. Testing of thin film ability of photocatalytic breakdown of methylene blue
2. Detecting geosmin and MIB via GC-MS
3. Testing of thin films to degrade geosmin via visible and UV-light
4. Testing of thin films to degrade MIB via using visible and UV-light

1.3 THESIS STRUCTURE

This thesis presents an overview of detecting, using Gas Chromatography Mass Spectrometry, and eliminating, using photocatalytic titanium-based thin films produced by a magnetron sputtering method, taste and odour compounds from drinking water. The thesis, divided into four parts, further divided into 12 chapters and the appendices. Part I presents the background information and context of the research in this thesis. Part II describes analytical and experimental techniques used in this

project. Part III provides an extensive description of the results obtained from this work and discusses the findings relating to the taste and odour problem. Part IV presents the main findings of this work and conclusions with suggestions of future work.

A more detailed description of the thesis structure is as follows:

Chapter 1. Describes the background and motivation of the research along with research aims and objectives.

Chapter 2. Introduces the taste and odour problem in drinking water and discusses the analytical detection of these taste and odour compounds in addition to the current technology and treatment and elimination techniques currently used.

Chapter 3. Introduces the main principles of photocatalysis, uses of titanium dioxide as a photocatalyst and ways to improve its photocatalytic performance.

Chapter 4. Presents thin film uses and overview, and introduces the deposition technique of magnetron sputtering.

Chapter 5. Presents nanoparticle uses and an overview of nanoparticle production techniques. Chapter 5 also explains the methods used for nanoparticle production.

Chapter 6. Explains the methods used for thin film production.

Chapter 7: Presents the analytical techniques used for characterisation of the thin films and nanoparticles. This chapter also discusses the methods used to degrade and detect taste and odour compounds.

Chapter 8: Presents the characterisation results for thin films.

Chapter 9: Presents the nanoparticle results.

Chapter 10: Presents photocatalytic test results and summarises the main characteristics of the materials needed for a successful photocatalyst.

Chapter 11: Presents the GC-MS results for detection of geosmin and MIB and the use of the method to record the degradation of the compounds. Comparison of the various photocatalytic materials and their ability to break down geosmin and MIB

Chapter 12: Presents a summary of completed work, the findings and main conclusions of this thesis along with future work suggestions.

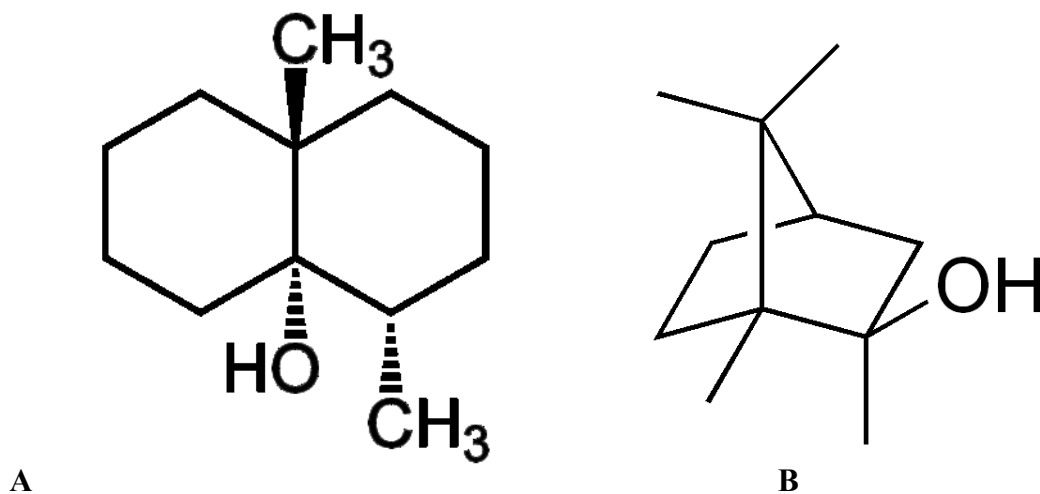
CHAPTER 2 TASTE AND ODOUR COMPOUNDS IN DRINKING WATER

This chapter introduces the taste and odour problem in drinking water supplies across the world. Discussed within this chapter is the analytical detection of taste and odour compounds and the elimination techniques available.

2.1 TASTE AND ODOUR COMPOUNDS

Earthy-musty taste and odour (T&O) compounds are a significant issue which are the origin of many consumer complaints over the “quality” of drinking water. Geosmin (trans-1,10-dimethyltrans-9-decalol) and 2-methylisoborneol (MIB) are cyclic aliphatic tertiary alcohols (see Scheme 1) that are the most common naturally occurring T&O compounds, which contribute to the organoleptic properties of drinking water and alter consumer acceptability.

Scheme 1: Chemical structures of: A, geosmin, and B, 2-methylisoborneol (MIB)



2.2 GEOSMIN AND MIB

Geosmin and MIB are produced by a range of cyanobacteria and actinobacteria in water and have odour threshold concentrations in the ng/L range⁴⁻⁸. The pathway of geosmin and MIB from source to consumer drinking water taps is a simple one (Figure 2). Geosmin has an extremely low odour threshold concentration (OTC) of 10 ng/L,⁹ consequently the human nose is extremely sensitive to its presence. Anecdotally it has been reported that if just a teaspoon of geosmin was added to 200 Olympic-sized swimming pools, it would still be possible to smell it¹⁰. The general threshold for human detection is approximately 15 ng/L¹¹. However it has been reported that people with sensitive palates can detect these compounds in drinking water when the concentration is as low as 5 ng/L¹⁰. When water containing geosmin and MIB is heated these compounds are volatized, explaining why their smell is more easily detected, for example, when in the shower or when used in hot beverages¹⁰. Most of the T&O problems in drinking water are the result of human influence; indirectly by rapid enhancement of the growth of aquatic organisms, or directly via wastewater dumping, accidental spillage as well as agricultural runoff. This pollution by nutrients enhances the growth of cyanobacteria and actinobacteria with the most problematic cause of T&O in water being from the production of earthy/muddy odours by cyanobacteria¹².

Geosmin and MIB are responsible for earthy ‘off’ flavours in public water supplies, aquaculture, and a host of other important products¹³, such as food and drink. Whereas MIB is generally associated with a muddy odour, geosmin has more of a musty or “old-book” odour¹⁴. The characteristics of these earthy odorants are presented

within Table 1. The odours of geosmin and MIB can however, be masked by chlorine¹⁵. In natural waters geosmin and MIB can occur together or separately, they are found in different types of water reservoirs and the concentrations of these substances are variable¹⁶. Fish tissue readily absorbs off-flavours from water such as geosmin and MIB, which results in serious commercial losses as the fish becomes unpalatable and therefore unmarketable¹⁷.

Table 1: Characteristics of earthy odorants; adapted from reference [11].

Compound	Chemical name	Molecular weight	Threshold odour concentration range (ng/L)	Odour description
Geosmin	Trans-1, 10-dimethyl-trans-9-decalol	182	1-10	Earthy/musty
MIB	2-methylisoborneol	168	1-10	Muddy/mouldy

There is a need to monitor the concentrations of geosmin and MIB in drinking water and, if above the threshold, decrease them via elimination strategies, as employed by water utility companies. The low OTC of geosmin and MIB in drinking water poses a problem, along with their resistance to conventional water treatment processes such as coagulation, sedimentation, filtration and chlorination¹⁸.

While T&O compounds can be unpleasant, geosmin and MIB are actually non-toxic and not harmful and they have not been associated with any health effects¹⁹;

therefore, the water remains safe to drink, though may not seem to be, due to its odour^{20, 21}. This T&O problem for water treatment companies can be much greater in the summer months, this is due to warm, nutrient rich conditions which lead to cyanobacterial blooms.

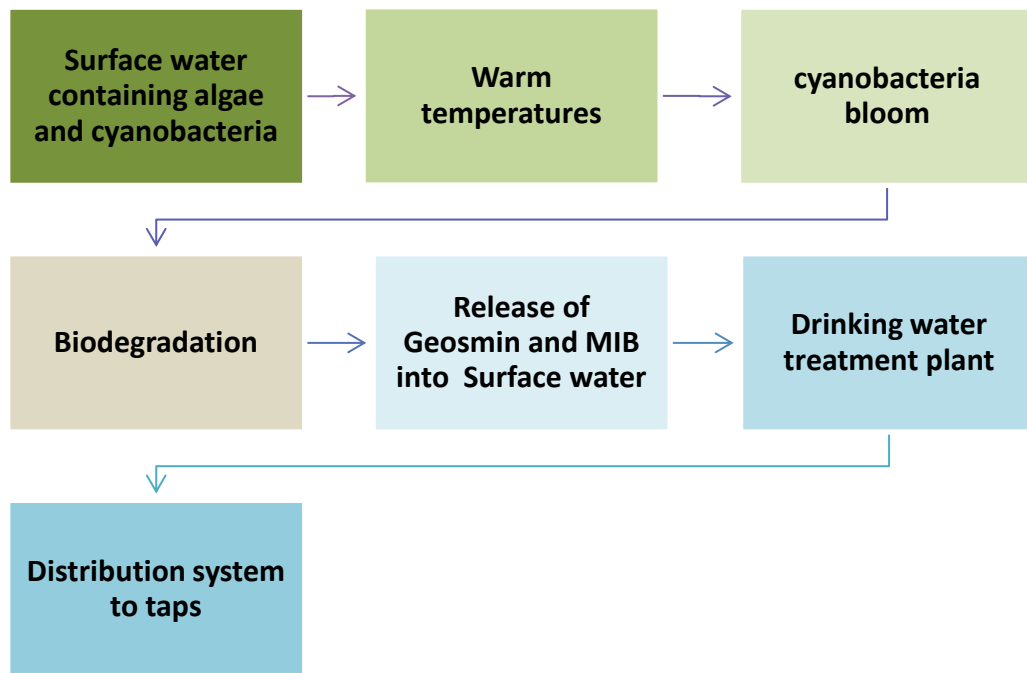


Figure 2: Simplified pathway from the source of geosmin and MIB to the consumer drinking water

Generally, there are few regulations for these two compounds; including in the US, the Environmental Protection Agency has not defined maximum permissible concentrations for geosmin and MIB in drinking water. Taste and odour standards are however, present in some countries, for example in the UK the threshold is described in the national assessment of drinking water report²². The maximum threshold concentration described in this report is 10ng/L for both MIB and geosmin²². While South Korea has a maximum allowed limit of 20 ng/L for both compounds²³, one of

the only countries to set a limit. The presence of these substances in drinking water may result in decreased consumer acceptability of the water and therefore, decreased water consumption and this could eventually cause the public to switch to alternate sources of drinking water such as bottled water and at-home treatment systems. The worldwide consumption of bottled water has experienced an annual increase of 5.5% since 2004²⁴. Different authors have speculated that this is due to beliefs of superior flavour of bottled water over drinking (tap) water²⁵. It is therefore suggested that T&O compounds in drinking (tap) water can contribute to a consumer perception that bottled water has a better taste. Owing to their chemical structures (cyclic tertiary alcohols) both geosmin and MIB are resistant to oxidation, a process commonly applied in water purification techniques. This, along with their low odour threshold, makes them nuisance substances to effectively remove from water. T&O compounds in drinking water are not restricted to certain geographies and are a problem faced by water treatment facilities around the world²⁶. A survey conducted with more than 800 utilities companies in the USA and Canada found that 16% of these companies experience T&O problems and an average of 4.5% of their budget is spent on trying to control their levels²⁷. From these companies 20% of them report annual outbreaks during the summer months²⁸ as a result of cyanobacteria bloom. Studies over the past few years have focused on developing tools that can predict bad T&O episodes, taking into account the trophic state of the water source^{29, 30}. Chlorophyll levels and the trophic state of the reservoir were found to be good indicators of T&O causing compounds, because cyanobacteria and MIB/geosmin concentrations are found to be

directly proportional to the chlorophyll concentrations in water²⁹. The publication frequency of geosmin and MIB is represented in Figure 3; there have been 568 papers published with the keywords ‘geosmin and MIB’ (web of knowledge 2016) and 347 of these papers have been published within the last 10 years. Most of these publications are published under ‘environmental sciences and ecology’ suggesting that they are focused on the environmental effects of geosmin and MIB with research into their formation and metabolic pathway (which is still relatively unknown). The relatively low, but increasing number of publications in this area emphasises the global need for research in order to enhance the development of analytical techniques and treatment methods for geosmin and MIB.

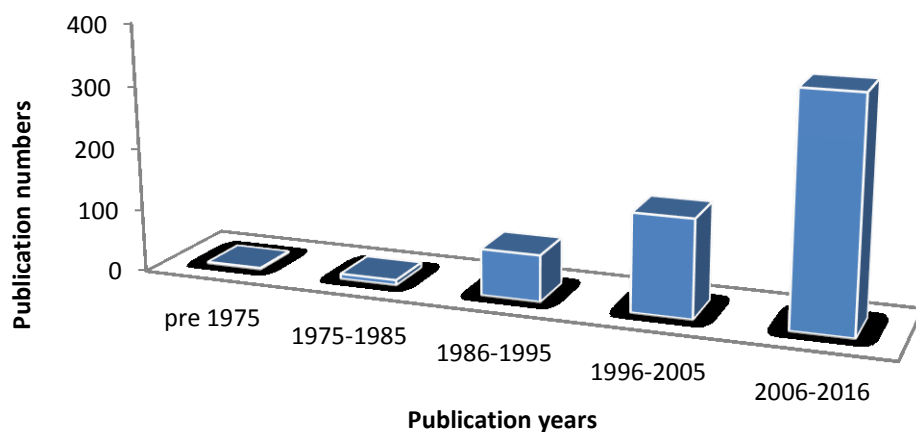


Figure 3: A timeline representing the number of geosmin and MIB related publications (Source: Web of Knowledge 2016)

This chapter provides an up-to-date overview of the analytical techniques reported for the identification and detection of geosmin and MIB with an emphasis on drinking water. Note that the last review paper of geosmin and MIB was published in 2011⁹. This chapter presents potential analytical techniques that could be implemented to identify and detect geosmin and MIB in drinking water. Furthermore, this chapter gives an oversight into treatment and potential future treatment technologies for these ubiquitous T&O compounds. A clearer understanding of the diagnosis and treatment of geosmin and MIB in drinking water will enable water treatment facilities to improve their treatment of T&O compounds.

2.3 ANALYTICAL DETECTION OF TASTE AND ODOUR COMPOUNDS

The analytical identification and quantification of important taste and odour compounds such as geosmin and MIB is required since they affect the organoleptic properties of drinking water and therefore the consumer perception and acceptability of drinking water. There is a range of analytical techniques that have been used for their identification and quantification.

2.3.1 SENSORY ANALYSIS

Human senses are the most sensitive tools for the detection of T&O compounds. However, sensory analysis is subjective, qualitative rather than quantitative, and extremely difficult to standardise. Sensory analysis has been used for many years in the assessment of the quality of drinking water, which was first applied to food and beverages flavour analysis and, in 1985, adapted for drinking water¹². This

approach is based on the rating of the odour intensity of a sample provided by trained panellists. This method has been reported to be precise, reproducible and accurate compared to untrained consumers, but is of course dependent upon panellist training. This technique of human sensory detection has been studied widely with a focus on human variability of the taste and odour compounds. Different studies have examined human detection of the taste and odour compounds at different temperatures and in different settings³¹.

2.3.2 INSTRUMENTAL ANALYSIS

Instrumental analysis of geosmin and MIB has been performed by conventional analytical techniques since the late 1980s and early 1990s. Gas chromatography and mass spectrometry were the first analytical techniques used, where geosmin was detected and identified by capillary gas chromatography - mass spectroscopy³². An interesting modification of gas chromatography was developed in 1988, which combined instrumental and sensory analysis, and was given the name “chromatographic sniffing”³³. In this approach the chromatographic step is for the separation of the compounds and the detection is done purely on sensory analysis, and so similar problems as described above arise.

Traditional analytical methods for monitoring MIB and geosmin concentrations include closed-loop stripping³⁴, liquid–liquid extraction³⁵, steam distillation³⁶ and purge and trap³⁷. These techniques were effective, but time consuming and labour intensive³⁸. In the 1990s an alternative technique was

introduced, known as solid phase extraction (SPE), and was able to measure very low concentrations of geosmin in fish tissue, using a solid phase absorbent. However, the apparatus setup involved a large number of components and was complex^{39, 40}. In 1996, solid phase micro-extraction (SPME) was used for the first time to measure organic micro pollutants in water. The focus of this research was volatile organic compounds (VOCs) such as benzene and toluene⁴¹. Since this pioneering report, research has been directed to optimize SPME for analysis of geosmin and MIB in water and now has become a standard analytical method³⁸. In a more recent study, a SPME-GC-MS based method demonstrated detection limits as low as 2 ng/L for both geosmin and MIB⁴². Further optimization of this method has resulted in detection limits being lowered to 0.9 ng/L and 0.6 ng/L for geosmin and MIB, respectively⁴².

Thermo Scientific developed a technique for the analysis of geosmin and MIB using SPME-PTV-GC/MS⁴³. The GC uses Programmed Temperature Vaporization (PTV), an instrument variation on the injector that improves desorption by extending the life of the fibre (which adsorbs the target compounds) within the GC. The injector (PTV) is heated to around 60°C for 30 minutes, (the temperature of extraction). When the fibre is transferred to the injector the temperature is raised to the desorption temperature of around 230°C. The fibre cools to room temperature and then is removed from the instrument, this process extends the life of the fibre. Excellent sensitivity and chromatographic performance was demonstrated with this instrument variation and detection limits of less than 0.4 ng/L were reported for both geosmin and MIB⁴³.

Analytical methods that can measure such low concentrations with high accuracy and precision are needed because the OTCs for these compounds are in the ng/L range. In addition to improving accuracy, these recent developments in analytical techniques have significantly improved the turnaround time for analysis, therefore allowing rapid analysis of a large number of samples. Agilent Technologies reported that the SPME method can detect geosmin and MIB at the ng/mL levels and that the method provides easy, accurate and sensitive odour compound analysis in drinking water⁴⁴. This technique was however, not applied to real samples and therefore the analysis was limited.

Hurlburt and co-workers presented an elegant study comparing the use of SPME with the membrane assisted solvent extraction (MASE) procedure¹⁴. The two analytical techniques were compared using four cyanobacteria samples known to produce off-flavours. The concentrations of the off flavours determined by MASE were lower than the values determined by SPME and, in general, precision increased with increased concentration¹⁴. The study also compares the use of SPME and methods such as liquid-liquid extraction for the analysis of the earthy tasting geosmin and MIB, and concluded that SPME is simpler, less expensive, and more sensitive than the liquid-liquid extraction techniques⁴⁵. Although methods such as liquid-liquid extraction can be effective, they are expensive and time consuming⁴⁵. The added cost and sample preparation for liquid-liquid extraction leads to the conclusion that SPME is the method of choice for the detection of compounds at low levels required here. For applications in which the concentrations are higher and accuracy is important,

liquid-liquid extraction becomes the method of choice. Xiaoyan and co-workers also came to the same conclusions when comparing SPME with liquid-liquid extraction⁴⁶. The SPME method has recently been accepted and published as Standard Method 6040 D, Analysis of Taste and Odour Compounds⁴⁷. This method uses an SPME fibre for adsorption of target compounds (geosmin and MIB)⁴⁷. Liquid Chromatography mass spectrometry (LC-MS) has been used to detect geosmin and MIB at levels as low as 1 ng/L. The method also demonstrated excellent precision and accuracy, even at trace levels of geosmin and MIB, however this technique has only been applied in model/buffer solutions and not to real water samples⁴⁸. This MS-MS method significantly eliminates matrix effects commonly observed in SPME extractions, providing lower detection levels and greater confidence for identifying these compounds at trace levels⁴⁸.

Agilent Technologies, reported that the use of ion trap MS allows ng/mL detection of geosmin and other odorants in drinking water⁴⁹. This method delivered a simple, yet sensitive and reliable detection of odorants. Such sensitivity is available from the instrument because the odorants are small, polar molecules and, therefore, produce extensive fragmentation during ionization, leading to ng/mL detection⁴⁹. Water samples from commercially available bottled water and tap water were analysed. The bottled water had a trace of MIB, whilst low ng/mL concentrations of geosmin and MIB were found in the various tap water supplies⁴⁹.

The key problem for water companies in the determination of geosmin and MIB concentrations is the lack of an onsite test to measure levels of geosmin and MIB

using water from a standard tap. A hollow fibre membrane-based (HFSA) sampler was applied to the sensing of geosmin and MIB in 2011, providing a novel approach to sample storage, as the water sample can be stored in the desorption device at room temperature for 3 days and at 4 °C for 2 weeks without loss of analytes⁵⁰. This method overcomes the drawbacks of the traditional method; *i.e.* storing large volume samples in a cooler packed with ice or a refrigerator at 4 °C to inhibit the production of MIB and geosmin by microorganisms during the shipping time⁵⁰. The HFSA was combined with SPME GC-MS so that analytes in the desorption solvent were determined. This procedure, combining GC-MS and SPME has a detection limit of 9 ng/L for geosmin and 4 ng/L for MIB⁵⁰. This sampling device was successfully applied to field sampling in Taihu Lake (China), with MIB and geosmin detected in the range of 0.11–0.61 µg/L during a medium out-break of cyanobacterial bloom. There is still a need for an onsite test at the tap device where, after a customer complaint, the water company can take a reading and assess the T&O problem. The development of the HFSA has however, provided a reliable sample storage solution⁵⁰.

All the above approaches are laboratory based analytical techniques and there is a clear need for a portable sensor for the on-site detection of geosmin and MIB; this can reduce transportation costs and sample storage issues and one can envisage that if a consumer has doubts on the quality of their drinking water, a rapid on-the-spot result could be obtained. To this end, an electronic tongue system, consisting of conducting polymer sensors that detect geosmin in distilled water, has been used in the USA⁵¹. The electrical response (capacitance) of the sensors was analyzed using principal

components analysis. The detection limit of this system was 25 ng/L and, although this is actually higher than the human threshold of detection, this technique could be used to provide the consumer or water company with confirmation that geosmin is present in a sample of water. The use of an electronic sensor device was also reported by a technology company who created a portable electronic nose that could quantify concentrations of MIB and geosmin by using gas chromatography ⁵². The nose was used on samples of geosmin and MIB made in the lab by a series of dilutions. These results were promising and showed that at room temperature geosmin and MIB were detected to a limit of 0.25mg/L and, after raising the temperature to 40°C, the limit of detection was 0.1mg/L. This method was also applied to pond water; however, no limit of detection was applied to real samples. The detection limits for this device are extremely high compared to the threshold odour concentrations and other techniques that enable detection limits in the ng/L range (see Table 2). Therefore, despite the potential of an electronic nose further development is clearly required to enable lower limits of detection. The range of analytical techniques reported for the detection of geosmin and MIB are summarised within Table 2.

Table 2: Overview of the reported analytical techniques used for the detection of geosmin and MIB.

No.	Technique	Limit of detection, Geosmin (ng/L)	Limit of detection, MIB (ng/L)	Comments	Ref.
1	GC-MS	1	0.5	First technique to be used in geosmin/MIB detection	34
2	SPME-GC-MS	0.9	0.6	Optimisation of SPME which has allowed improved LOD	44
3	SPME-PTV-GC-MS	0.4	0.4	Sensitive method	45
4	MASE-GC-MS	1	2.5	Compared to SPME, MASE is shown to be less sensitive but provides a greater level of precision, as well as the ability for multiple injections from the same sample; applied to cyanobacterial samples	11

5	Liquid-Liquid extraction and GC	0.8	0.8	Very precise but expensive and time consuming	47
6	SPME standard accepted method 6040 D	N/A	N/A	This method uses an SPME fibre for adsorption of target compounds and is the standard accepted method.	49
7	LC-MS	1	1	Excellent precision and accuracy but has not applied to real samples, this method can provide trace analysis with better LOD than SPME	50
8	Ion Trap MS	ND	0.4	Expensive and complicated method but produces sensitive detection and has been applied to commercially available bottle water and tap water	51
9	HFSA leading to SPME GC-MS	9	4	The HFSA device provides stable sample storage which then can be analysed by SPME-GCMS which is a very sensitive method	52

Key:GCMS: Gas chromatography mass spectroscopy; SPME: Solid phase microextraction; SPME-PTV-GCMS: Solid Phase microextraction -programme temperature vapourization- gas chromatography mass spectroscopy; MASE-GCMS: membrane assisted solvent extraction- gas chromatography mass

spectroscopy; LC-MS: liquid chromatography mass spectroscopy; HFSA: Hollow fibre membrane-based sampler

2.4 TREATMENT AND ELIMINATION OF GEOSMIN AND MIB

Stages of the drinking water treatment process are highlighted in a pathway in Figure 4. Despite using conventional treatment methods, such as coagulation, sedimentation, chlorination and filtration, elimination of geosmin and MIB is ineffective and alternative methods are being sought.

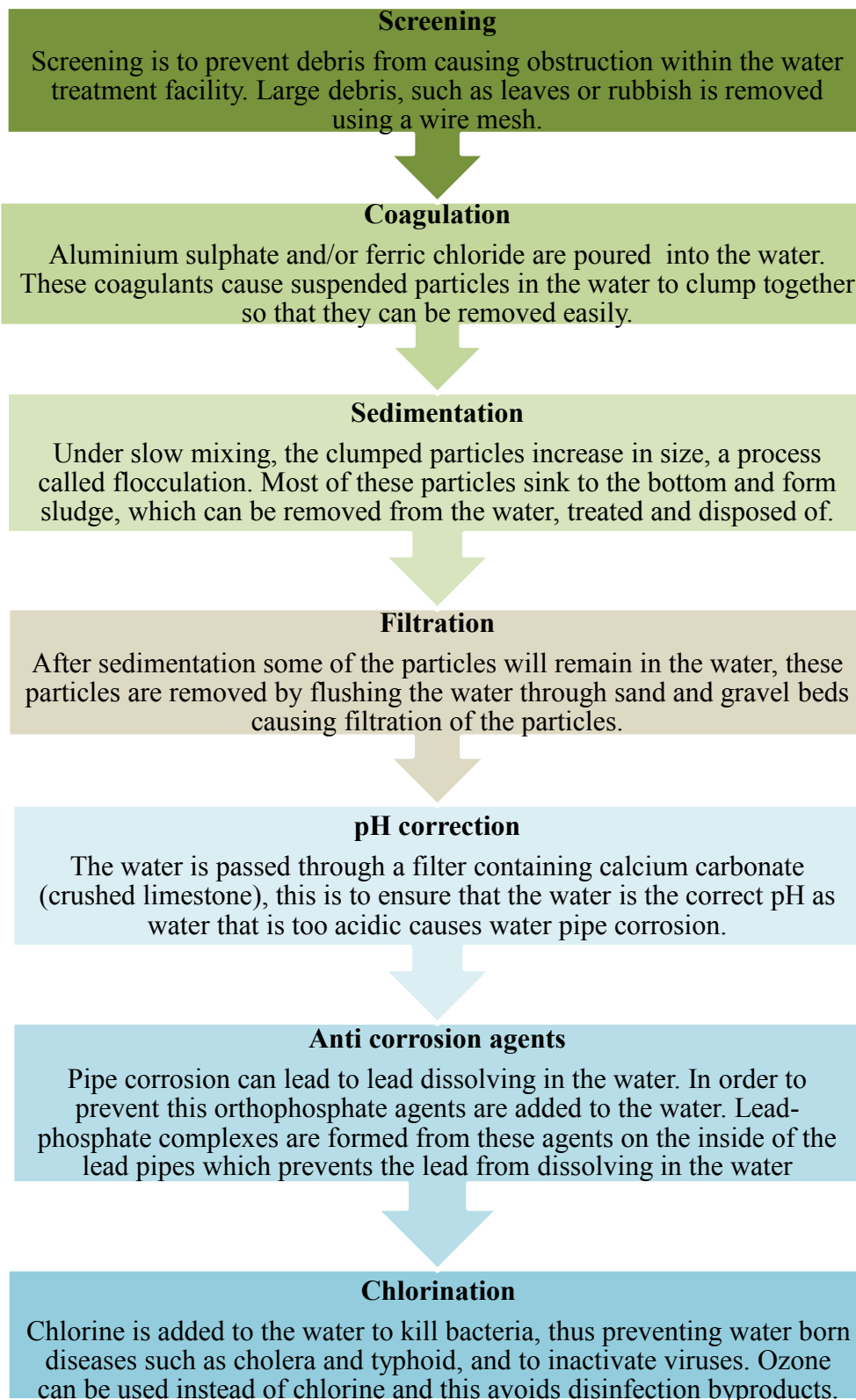


Figure 4: Stages of the drinking water treatment process

2.4.1 TREATMENT RESISTANCE AND CURRENT TECHNOLOGY

MIB and geosmin are extremely resistant to removal by conventional water treatment processes such as coagulation, sedimentation, chlorination and filtration¹⁸. For example, chlorination is one of the most important stages in conventional water purification, as it disinfects the finished water and destroys harmful substances by oxidation. Chlorination is also inexpensive and easy to apply, but unfortunately chlorination often leads to consumer complaints due to a ‘chlorine’ smell in the water. Geosmin and MIB are resistant to chlorine, even at a high dosage, so other methods for their removal need to be applied¹². The UK Water Framework Directive (2014) summarised the effectiveness of the conventional water treatment processes for geosmin and MIB; these findings are presented in Table 3.

Table 3: Removal of taste and odour compounds by conventional treatment (coagulation + filtration and chlorination) In the UK. Taken from reference [24].

Compound	Coagulation + filtration	Chlorination	Conventional treatment
Geosmin	0%	46%	46%
MIB	0%	46%	46%

It is clear that conventional treatments and chlorine treatment alone are not effective enough for the removal of geosmin and MIB¹². Water treatment plants operated by water utility companies must be used to reduce the concentration of

geosmin and MIB present in the finished water supply. The techniques of dealing with T&O compounds focus either on decomposition of the chemical structure or actual removal of the odorous compounds from the water. Methods of elimination include the use of activated carbon. Adsorption onto activated carbon is one effective way of reducing geosmin and MIB concentrations. This treatment method is also effective at causing a general reduction in total organic carbon. Activated carbon is currently used in water treatment facilities, however it was reported in the UK water framework directive that the drawbacks of this process are that it can lead to precipitation and other chemical reactions occurring at the carbon surface⁵³. Due to various water systems and the efficiencies of different styles of treatment efficiencies, parameters such as water quality and contact time are key factors in effectiveness of the removal of T&Os. Other treatment approaches include the use of sand filters. Removal of T&O compounds has been demonstrated with sand filters that contain biofilms. As with activated carbon treatment, sand filter efficiency also depends on contact time and varies with changing water qualities⁵⁴.

A treatment technology that is gaining in popularity is ozone⁵⁵. Ozonation and associated oxidation processes have been investigated for the removal of geosmin and MIB in nanopure water, lake water, river water and treated and untreated wastewater. Generally geosmin was found to be oxidised faster than MIB⁵⁵. Other approaches include ozone-enhanced biofiltration, which is effective for the removal of geosmin and MIB as well as trace organic removal. Whilst it is evident that climate change is predicted to increase the intensity of cyanobacterial blooms, through more droughts

and flooding, and, therefore, increase the production of geosmin and MIB, it is clear that climate change could also significantly influence the ozonation, which can break down geosmin and MIB⁵⁶. Prevention of geosmin and MIB outbreaks could be prevented at the source, by identifying the strains of bacteria that contribute to these compounds and eliminating them. A recent study by Suurnäkki and co-workers has used molecular detection methods, such as DNA sequencing to determine the producers of these compounds⁵⁷. After screening 100 strains of cyanobacteria and identifying 19 new off-flavour producers, which were isolated from aquatic and terrestrial environments; interestingly geosmin was found to be produced by all studied strains. The results also indicated that geosmin-producing cyanobacteria also produced other metabolites that are potential toxins, which may have implications for human health.

Geosmin and MIB outbreaks could be prevented at the source, by identifying the strains of bacteria that contribute to these compounds and eliminating them. Newer areas of treatment technology have emerged in the last four years; these are described in the next Chapter (sections 3.2 and 3.3). Many forms of treatments have been tried and tested over the years and there is still scope for improvement on current methods with greater T&O elimination rates. Table 4 gives a summary of all the current treatment options to eliminate geosmin and MIB. The effectiveness has been concluded in the Table, and has been deduced from the ability to eliminate geosmin and MIB.

Table 4: Summary of the treatment options to eliminate MIB and geosmin

No.	Treatment options	Effective/ ineffective	Comments	Ref
1	Activated Carbon	Effective	Effective but not efficient and other chemical reactions can take place on carbon surface	55
2	Chlorination	Ineffective	Cheap and easy treatment option to apply for pathogen control but ineffective at geosmin and MIB removal	9
3	Biological biofilms (growing on sand in sand filters)	Effective	Effective but similar problems to activated carbon arise	56
4	Biological processes eg. Bioreactors	Ineffective	Extremely low removal of geosmin, questionable if removed at all	59
5	Oxidation via ozone	Effective	Very expensive however very effective	56,57
6	Radiation via UV light	Somewhat effective	Expensive but effective in removing up to 50% of the compounds	63
7	UV light and hydrogen peroxide	Effective	This system is in use for taste and odour treatment in Ontario, Canada.	64

8	Radiation using UV light and TiO ₂	Effective	More effective than UV light in breaking down geosmin/MIB however questions raised on how suitable the methods are for large scale treatment	65-67
9	Ultrasonic degradation	Effective	Not suitable for large scale treatment and very expensive	72

2.4.2 BIOLOGICAL TREATMENT

In the late 1990s and early 2000s, there was wide use of biological treatments for the removal of contaminants in drinking water. Some of the first research carried out with biological removal of geosmin concentrated on using a lab scale bioreactor⁵⁸. The results demonstrated very low geosmin removal and concluded that biodegradation was not the most effective technology for removal of taste and odour compounds in drinking water. Although geosmin and MIB have been shown to be biodegradable, no definite pathway for either compound has been elucidated to date⁵⁹. In a study by Ho et al. MIB and geosmin were shown to be readily removed through bench-scale sand filters, with the removal being identified as a biodegradation process. Biodegradation of both MIB and geosmin was determined to be a pseudo-first-order reaction, with rates influenced by the initial concentration of the biofilm but not the initial concentration of the T&O compounds. Furthermore, biodegradation rates were increased when the biofilm had been pre-exposed to MIB and geosmin⁵⁴. The use of biological treatments, such as sand filters, depends on the contact time between the microbes and the T&O's and so it is not realistic to pre-expose the T&Os to the biofilm.

With this in mind, the use of biological treatment would require the identification of the bacteria strains that cause the degradation.

2.4.3 PHYSICAL TREATMENT AND CHEMICAL OXIDATION

Ultra-violet based technology is promising for the treatment of T&O compounds in water⁶⁰. A study by Rosenfeldt in 2005 examined the effectiveness of direct UV photolysis and the UV/hydrogen peroxide (H₂O₂) advanced oxidation process for removing MIB and geosmin from raw source water and treated water⁶¹. Direct UV photolysis removed 10% and 25–50% of the MIB and geosmin, respectively. The addition of H₂O₂ created advanced oxidation conditions and oxidized greater than 70% of these compounds, thus providing an effective approach⁶¹. A treatment technology used in Ontario is the addition of hydrogen peroxide to a UV disinfection system. This treatment technology, reported in 2015, is where hydrogen peroxide is added to water upstream of a UV system⁶². The combination of UV and hydrogen peroxide initiates a powerful oxidation reaction that destroys T&O causing chemicals without forming harmful by-products⁶³. The disadvantage of such a system is the high cost⁶². This system, to our knowledge, is the first of its kind. Although effective, there is still scope for a better method of removal that would avoid using large amounts of hydrogen peroxide and UV light; both relatively expensive⁶⁴ but the cost to purchase the former is likely to be less than that of the electricity required for the latter.

Physical treatments to remove geosmin and MIB have rapidly developed in the past few years. The current research focus on the physical treatment of T&O's such as geosmin and MIB is very much on using photocatalytic titanium dioxide (TiO₂) and demonstrating higher levels of removal than reported for other techniques⁶¹. Photocatalysis has been widely used in water treatment over the years, more commonly to remove organics⁶⁵. The removal of T&O compounds via photocatalysis has only recently been investigated. Recent lab based studies by Lawton and co-workers have looked into the destruction of geosmin and MIB using TiO₂ photocatalysis, whilst irradiating with a 280W UV-light (with a spectral output of 330-500 nm); the study was successful and was the first to demonstrate the removal of geosmin via TiO₂ photocatalysis⁶⁶. Bamuza-Pemu and Chirwa presented a study in 2012 where the photocatalytic degradation of geosmin was conducted in batch systems at a concentration of 10 ng/L with solutions prepared by spiking ultrapure water with geosmin standards, with a reaction pathway analysis conducted. Geosmin solutions were irradiated with a 400W UV-Vis lamp (with a spectral output of 300-600nm) in the absence and presence of TiO₂. Photocatalytic degradation of geosmin occurred rapidly, achieving over 99% degradation in 60 minutes, while UV photolysis alone achieved only 86% degradation in 60 min, therefore suggesting that TiO₂ photocatalysis is promising for the breakdown of geosmin,^{67, 68} though MIB was not explored. This area of research is growing with a few studies in the past few years into the effectiveness of using TiO₂ to degrade T&O's.

In 2015 more recent work demonstrated the preparation of stable TiO₂–USY (Ultrastable Y zeolite) zeolite composite coatings *via* the layer-by-layer dip-coating method for efficient adsorptive and photocatalytic removal of geosmin at ng/mL concentration levels⁶⁹. This promising technology gives rise to a high level of removal and, if the technology can be applied into the field, there could be a potential breakthrough in water treatment to remove these T&O compounds.

In a different approach, ultrasonic (640 kHz) degradation of geosmin (10 µg/L) and MIB (10 µg/L) was reported in 2007; the compounds were readily degraded within 10 minutes and less than 50 % of the starting material remained. After 40 minutes of ultrasonic treatment, over 90 % decomposition of both compounds was achieved. This therefore is an applicable method for the removal of MIB and geosmin from drinking water. However, since the general application of ultrasound for water treatment can potentially be costly, careful evaluation of the economic feasibility is required as this technique might not be suitable for large-scale treatment⁷⁰. A further disadvantage of these techniques is due to the fact that water samples need to be transported to the instrument, which could be time consuming. Further processing steps may be required, such as pre-concentration procedures. All of these factors are time consuming. This would be an issue if the sample was required urgently, possibly due to a developing environmental issue. The development of a future successful biological treatment would need to include prevention of geosmin and MIB outbreaks at the source, i.e. identifying the bacteria needed to break the T&O compounds down. Whereas the

development of a cost-effective physical treatment, would provide water treatment facilities with an alternative treatment method; which would save them money.

This chapter will give an overview of semi-conductor photocatalysis and the relevance of this within producing thin films and using them for the breakdown of taste and odour compounds in drinking water. This chapter does not give a comprehensive review of the photocatalysis phenomenon; it mainly focuses on the aspects of the photocatalytic process that are relevant to the current research project, e.g. the use of titanium dioxide. The chapter introduces the main advantages and drawbacks of using titanium dioxide as a photocatalyst and briefly reviews the methods of improving its efficiency that have been used in this work.

3.1 SEMICONDUCTORS

A semiconductor is a transitional stage material between an insulator and a conductive material⁷¹. The energy band gap and the electrical conductivity of semiconductors, compared to insulators and metals, is shown in Figure 5. In the case of an insulator, the band gap is so large that electrons cannot cross the distance between the valence band and the conduction band. For metals, there is no band gap and so electrons can move freely, giving rise to conductivity. For a semiconductor the electrons in the valence band can be excited by light energy greater, or equal to, its band gap, moving to the conduction band and creating electron-hole pairs. The flow of electrical current in a semiconductor depends on the electrons, which act as charge carriers. The electrons responsible for carrying the electrical current are called conduction electrons. In general, these cannot move freely, however some electrons

are loosely bound and are released to become a conduction electron, leaving positive charged ions behind. The valence electrons are responsible for moving the positive charges from one atom to the other, which creates a path whereby the electrical current can travel.

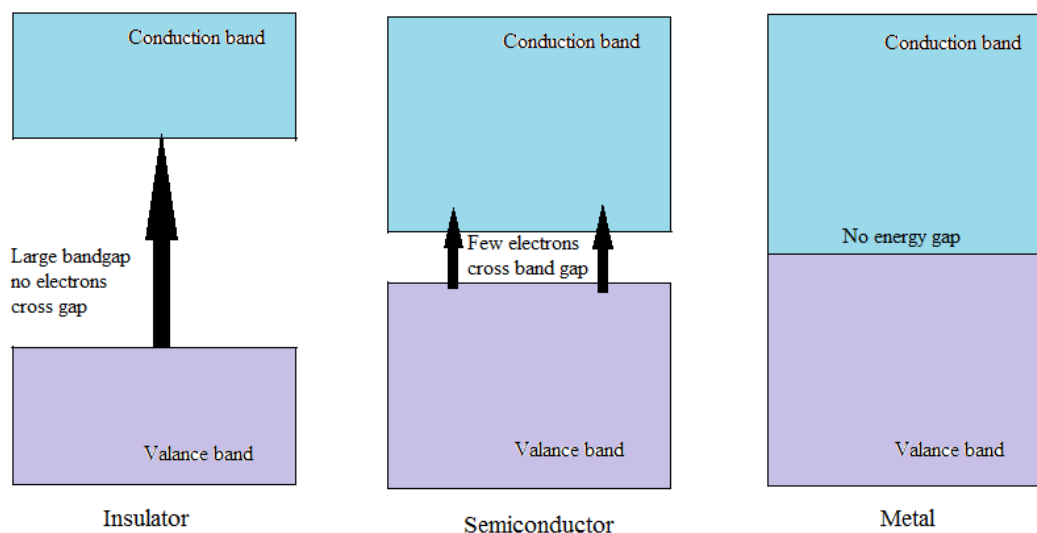


Figure 5: Energy bands in insulators, semiconductors and metals

Photocatalysis may be defined as the acceleration of a photoreaction by the presence of a catalyst⁷². A photocatalyst is a semiconductor material and with light irradiation the semiconductor is chemically activated. During the photoreaction process, the photocatalyst does not undergo any changes and it is not consumed as a reactant.

3.1. TITANIUM DIOXIDE CRYSTAL STRUCTURE

Titanium dioxide exists in three main forms, anatase, brookite and rutile. The two forms that are of interest in photocatalysis are anatase and rutile.

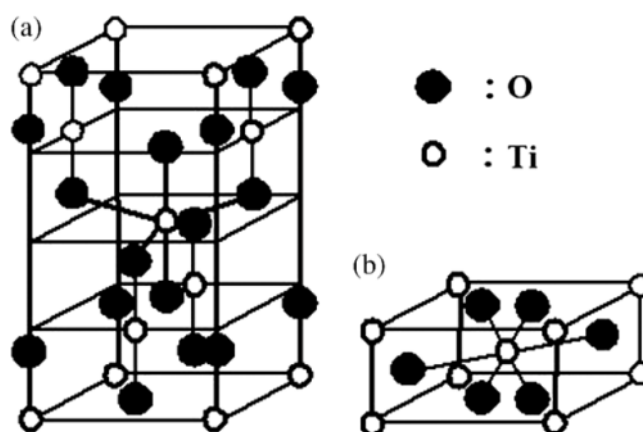


Figure 6: Crystal structure of a) anatase and b) rutile⁷³

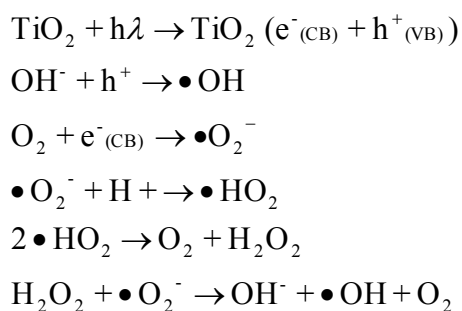
Both the rutile and anatase forms of TiO_2 have a tetragonal structure; they each contain 6 and 12 atoms per unit cell, respectively (Figure 6). In both crystal structures, each atom of titanium is coordinated with six oxygen atoms. Rutile has a lower band gap (3.0 eV) than anatase (3.2 eV), but, despite this, anatase exhibits better photocatalytic properties as a result of higher surface area and thus higher level of adsorbed radicals. Anatase has a larger band gap than rutile TiO_2 . While this reduces the light that can be absorbed, it may raise the valence band maximum to higher energy levels relative to redox potentials of adsorbed molecules. This increases the oxidation ‘power’ of electrons and facilitates electron transfer from the TiO_2 to adsorbed molecules⁷⁴. The rutile phase finds application as a white pigment in paints, cosmetics and the food industry due to its high refractive index.

3.2 TITANIUM DIOXIDE AS A PHOTOCATALYST

Titanium dioxide, in the anatase crystalline form (as opposed to the rutile or brookite forms) is the most widely used photocatalyst due to its relatively low cost,

low toxicity and high photostability^{75,76}. Photocatalytic titanium-based surfaces have many potential applications including water purification⁷⁷. Using titanium dioxide thin film coatings to breakdown T&Os is promising because it is relatively straightforward to demonstrate the effectiveness of the films in laboratory conditions. Titanium dioxide produced in nanoparticle form can arguably be more effective, due to the high surface area of active material. However, problems can arise in drinking water treatment systems due to downstream filtration of the particles.

The following equations describe the heterogeneous process that takes at the surface of the semiconductor when TiO₂ is used as a photocatalyst⁷⁸.



When TiO₂ is irradiated by photons of the correct wavelength, it initiates photocatalytic properties, which in turn produce hydroxyl radicals ($\bullet\text{OH}$); via the splitting of H₂O and superoxide (O⁻) via electron donation. Both radicals readily reduce and oxidize organic molecules causing them to fracture into non-harmful fragments or adducts.

3.3 METHODS OF IMPROVING PHOTOCATALYTIC ACTIVITY OF TITANIUM DIOXIDE

The photocatalytic properties of TiO_2 are derived from the formation of photogenerated charge carriers (holes and electrons), which happens when the sample is irradiated with ultra-band gap radiation, i.e. of energy that is greater than or equal to the band gap energy of the sample. For TiO_2 in the anatase crystalline phase, the band gap energy is 3.2 eV (3 eV for rutile), thus the sample must be irradiated with ultraviolet (UV) light (wavelength less than 385 nm) for the photocatalytic process to be initiated. The photogenerated holes created in the valence band diffuse to the TiO_2 surface and react with adsorbed water molecules, forming hydroxyl radicals. The hydroxyl radicals oxidize nearby organic molecules on the TiO_2 surface. Meanwhile, electrons promoted to the conduction band participate in reduction processes, which typically react with molecular oxygen in the air to produce superoxide radical anions⁷⁹ (Figure 7).

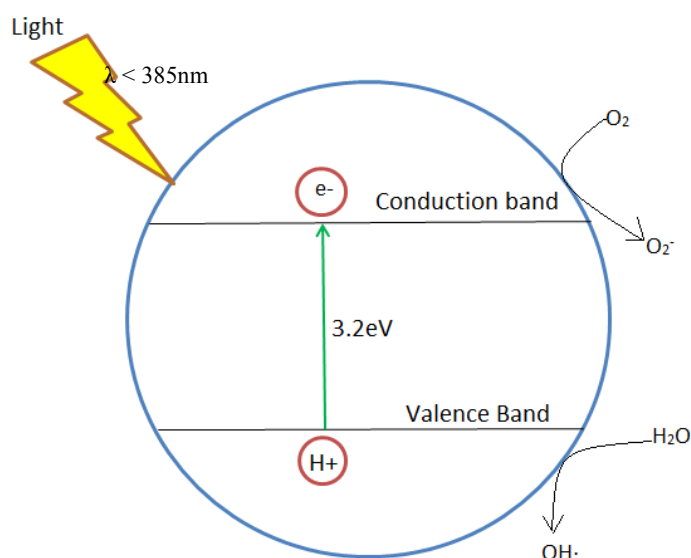


Figure 7: Titanium dioxide photocatalysis

The large band gap (3.2 eV) of anatase is, though, a major drawback, which means that illumination with wavelengths below 385 nm are necessary for excitation, thus limiting its sensitivity to the UV part of the solar spectrum⁸⁰. Sensitisation of TiO₂ to visible wavelengths can be achieved by the inclusion of impurities (dopants) e.g. molybdenum in the TiO₂ structure. The impurities create additional band gaps, allowing absorption to occur at higher wavelengths and enhances quantum efficiency *via* inhibiting the recombination of photo-generated holes and electrons, it has been shown that of the transition metals, molybdenum is very efficient for shifting activity to the visible range⁸¹. Several studies have focused on titanium dioxide coatings doped with silver, copper, iron, chromium and the lanthanides⁸².

Doping titanium dioxide with non-metals e.g. nitrogen, narrows the band gap due to a mixing of the dopant p-states with the p-states of oxygen forming the valence band of titanium dioxide⁸³. The narrowing of the band gap is caused by the replacement of 3 oxygen atoms by 2 nitrogen atoms, leading to an oxygen vacancy that shifts the band gap from 3.2 eV to 2.8 eV⁸⁴. Of the range of possible non-metal dopants nitrogen is the one most described in literature for improving the photocatalytic activity of titanium dioxide⁸⁵ and extending its activity into the visible range⁸⁶. Nitrogen-doped TiO₂ has received great interest in research as density of states calculations have indicated that doping with nitrogen would be effective in narrowing the bandgap of titania compared to other non-metal dopants^{87, 88}. In particular, doping with nitrogen has been shown to effectively improve the photocatalytic activity of titania under visible light, which is thought to be induced by the mixing of the N 2p

and O 2p states resulting in the band gap narrowing. Recently, Asahi *et al.* showed that TiO₂ films can be doped with (1-5%) nitrogen by sputtering methods, which allowed photoactivity for breakdown of 2-propanol in the visible spectral range⁸⁸. Other attempts to incorporate nitrogen within the TiO₂ structure include annealing TiO₂ at elevated temperature under the flow of ammonia for long time periods, which met with limited success⁶⁶. Whilst the decomposition of geosmin and MIB has been investigated using UV light there are limited studies showing titania doping resulting in visible light degradation⁸⁹. In this study, TiO₂ and N doped TiO₂ films were prepared by the magnetron sputtering technique and the photocatalytic activity was studied by monitoring the decomposition of geosmin and MIB under visible and UV light irradiation. Photo activity in the visible spectrum was made possible by the efficient incorporation of the N dopant. Furthermore, under UV illumination the presence of the N dopant had an enhancing effect, contrasting with a previous report that UV activity deteriorated with N-doped titanium dioxide⁹⁰.

There are different methods of testing the photocatalytic ability of TiO₂. Since photocatalysis is used to break down organic molecules methods can be used to detect particular molecules and analyse any change in concentration over time. This can be performed via methods such as gas chromatography and mass spectrometry. In order to gain insight into the rate of photocatalysis itself, observing the degradation of a coloured molecule such a methylene blue dye and measuring its change in absorbance over time can provide a fast and cost effective method of testing photocatalytic activity.

CHAPTER 4

THIN FILMS GROWN VIA MAGNETRON SPUTTERING

This chapter presents an overview of the thin film deposition process used in this work, specifically focussing on the physical sputtering technique commonly known as magnetron sputtering. Various coatings were produced to test their potential to break down the T&O's geosmin and MIB. The coatings produced were titanium dioxide, nitrogen doped titanium dioxide, molybdenum doped titanium dioxide and erbium doped titanium dioxide. This chapter introduces the theory of techniques and methodology behind producing these various coatings. The experimental details for their production can be found in Chapter 6.

4.1 PHYSICAL VAPOUR DEPOSITION

Physical vapour deposition (PVD) is a generic term for a group of atomistic deposition process, whereby a vapour is generated from a solid source and transported across a vacuum medium to condense on a surface as a thin film. The vapourised phase may consist of neutral atoms or ionised species. With the addition of a reactive gas, such as oxygen or nitrogen, a chemical reaction takes place and new compounds are formed, this is generally referred to as reactive deposition. The main processes of PVD are vacuum evaporation, ion plating and sputter deposition. This thesis focuses on a specific area of PVD commonly known as sputtering and specifically magnetron sputtering. Thin films were produced by the magnetron sputtering technique, which is

further described in section 4.2.1, but first it is important to understand the processes behind the technique.

4.2 PHYSICAL SPUTTERING

Sputter deposition is defined as ‘when a source material is vaporised via physical sputtering energetic particles generated by using a plasma’⁹¹. Plasma processing can perform 3 things, it can:

- Remove material from a surface, known as physical etching.
- Deposit a material onto a surface, known as sputter deposition.
- Modify the physical or chemical properties of a surface.

Etched or sputtered material can diffuse across a vacuum chamber to condense on a surface, forming a coating. Deposition of elements, compounds and alloys can occur and different sputter yields occur from different materials. This thesis specifically focuses on deposition via magnetron sputtering.

4.2.1 DC SPUTTERING

The direct current (DC) sputtering process is a very basic form of sputtering whereby an anode and cathode act as planar electrodes in a vacuum chamber. The target plate, from which the film is produced acts as the cathode in the system. The cathode is connected to a high voltage power supply. As argon is introduced into the chamber a glow discharge, or plasma is initiated between the electrodes. As the electrons accelerate away from the cathode, the argon gas is ionised leading to the

target being bombarded with positive argon ions, causing target atoms to be ejected away from the surface. The impact of argon ions at the target/cathode also results in the emission of secondary electrons, which cause additional ionisation of the argon gas atoms and make the discharge self-sustaining.

4.2.2 MAGNETRON SPUTTERING

As described above, in the basic sputtering process, a target (or cathode) plate is bombarded by energetic ions generated in a glow discharge plasma, situated in front of the target. The bombardment process causes the removal, i.e., ‘sputtering’, of target atoms, which may then condense on a substrate thin film⁸⁸. Momentum transfer causes atomic collisions to occur where the energy of the incident particles is transferred to the atoms of the target surface (Figure 8).

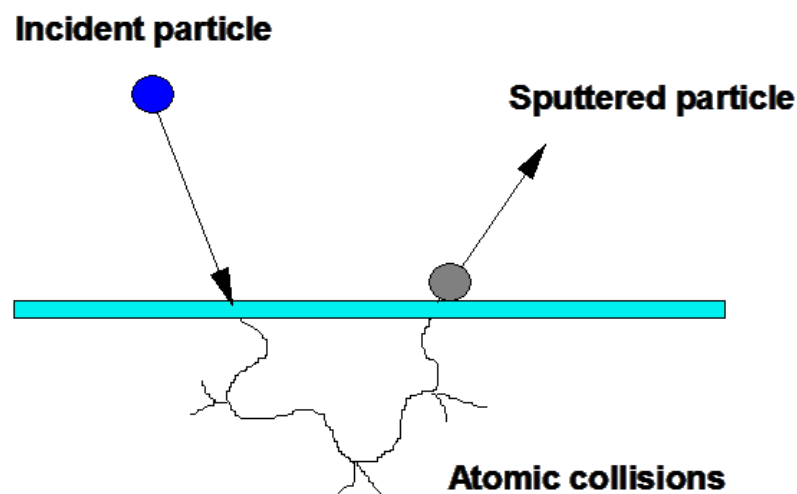


Figure 8: Atomic collision cascade diagram

The use of magnetron sputtering is the most widely used approach of the sputter deposition technique. ‘Magnetron sputtering has developed rapidly over the

last few decades to the point where it has become established as the process of choice for the deposition of a wide range of industrially important coatings. Eg. Hard wear-resistant coatings, low friction coatings, corrosion resistant coatings. In many cases, magnetron sputtered films now outperform films deposited by other physical vapour deposition processes and can offer the same functionality as much thicker films produced by other surface coating techniques.’⁸⁷.

4.2.3 MAGNETRON TARGET

The magnetrons make use of the fact that a magnetic field configured parallel to the target surface can constrain secondary electron motion to the vicinity of the target. The magnets are arranged in such a way that one pole is positioned at the central axis of the target and the second pole is formed by a ring of magnets around the outer edge of the target. Configuring the magnetic field in this way leads to the formation of a dense plasma in the target region, compared to a planar sputtering source. This, in turn, leads to increased ion bombardment of the target, giving higher sputtering rates and, therefore, higher deposition rates at the substrate.

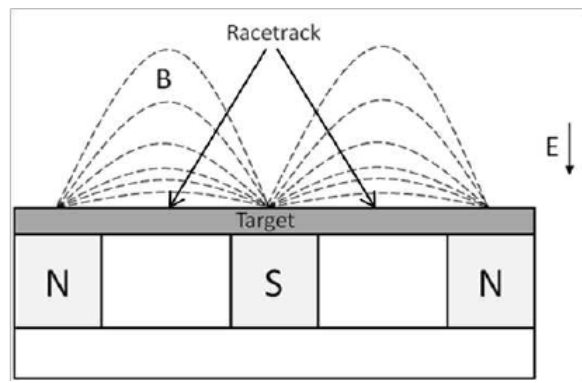


Figure 9: Schematic of magnetron showing 'racetrack' of each target⁹²

There are several types of magnetron available, this work uses planar magnetrons. Planar magnetrons have a high sputtering rate and are also convenient to use as there are no moving parts. Magnetic fields confine electrons near to the target surface. A higher degree of ionisation close to the targets leads to increased ion bombardment and hence a higher sputtering rate. In planar magnetrons, magnets are placed directly behind the target. For planar magnetrons the area between the magnets is the area where maximum ionisation occurs. This magnetic field shape caused by the magnetrons results in non-uniform sputtering of the target. The magnetic arrangement means that the sputtering of the target takes place predominantly between the inner and outer magnetic arrays where the field lines are approximately parallel to the target surface (Figure 9). The sputtering rate is highest in this region, resulting in a clearly visible erosion zone, which is referred to as the 'racetrack'.

A magnetron is considered to be balanced when the magnetic flux on the cathode surface is terminated to the magnetic core. Unbalanced magnetrons exist in two types, type I has a stronger central magnet and type II has stronger outer magnets.

Type II causes increased ionisation close to the substrate as the field lines are directed towards the substrate due to the outer magnets being stronger than the inner⁸⁷. The resulting plasma is highlighted in Figure 10. The importance of unbalancing the field is in the degree of ion bombardment of the growing films, the higher the ion current density the more bombardment, which can modify the growing film and give superior coating properties.

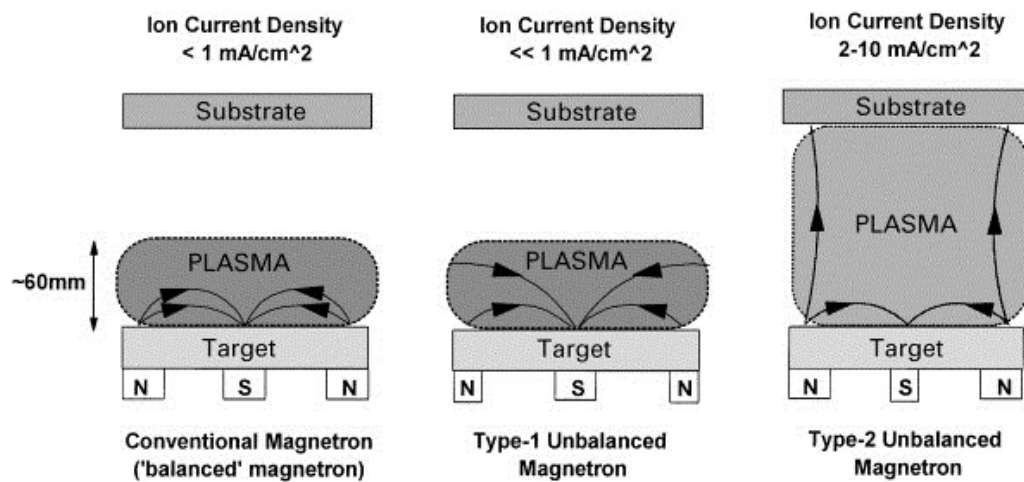


Figure 10: Unbalanced and balanced magnetrons⁶⁶

Substrate biasing is applying a negative bias to the substrate to provide increased acceleration of ions from the plasma and hence more energy to the growing film. Sufficient high voltage applied to the substrate can initiate a secondary discharge, generating ions close to the substrate and providing them with a large acceleration.

4.2.3 DEPOSITION

Reactive deposition is the introduction of reactive gases, such as nitrogen and oxygen, during the sputtering of metal targets, which leads to activation of the gas species and reaction at the substrate surface to form a variety of compounds. Precise control of the process is required to achieve the correct stoichiometry at acceptable deposition rates⁶⁶. For vapourised atoms to condense and solidify they require a solid surface to which they transfer energy. Particles tend to accumulate at ‘nucleation sites’ that are energetically favourable. Energetic adatoms may diffuse across a surface. The location of nucleation sites depends on the characteristics of the coating and substrate; examples may be at grain boundaries, surface imperfections or areas of chemical activity. The interface is the boundary between the coating and substrate. Interfaces may be abrupt, on an atomic scale, or may be graduated over a distance many atoms thick. A variety of interface types exist leading to different adhesion and growth mechanisms within a deposited film. Defects in coatings can be formed from substrate-surface defects, grain boundaries, micro-cracks and scratches.

4.3 THIN FILMS

The definition of a thin film describes a low-dimensional material created by condensing one-by-one atomic/molecular ionic species of matter on the surface of a substrate⁹³. The thickness is usually less than several microns thick. Basic properties of a thin film, such as film composition, film thickness, crystal phase and orientation are controlled by the deposition conditions. Film growth can be affected by substrate composition, morphology and any substrate surface contamination.

4.4 POWDER TARGETS

Powder form materials that can easily be mixed and spread across a recessed copper plate to make a sputter target. Using blended powder targets offers a relatively cheap means to sputter a material. Using solid targets only a small area of the target (25-30%) is utilised during sputtering, which is the race track area. Powder targets can be redistributed across the backing plate to ensure much better target usage. The powder is spread across a recessed plate and pressed or compacted to promote a better surface uniformity, and also to ensure the copper plate is not exposed below to ensure only the blended target is sputtered. An adequate weight (1kg steel rod) is used to tamp the blended target as light tamping can cause voids in the target and lead to target arcing⁷⁶. The advantages of a powder sputtering method is that the operation and usage of the method is very flexible; powder targets can be easily changed and as a method of producing thin films it is relatively cheap to source powder material. As a magnetron sputtering method, forming films from powder can be a very slow process and deposition time is often long. Controlling the sputtering rate of a powder target can be hard and repeatability of the composition of thin films produced from the powder target can prove difficult.

This chapter introduces the reasons for the use of nanoparticles in this work. Titanium dioxide and nitrogen doped titanium dioxide nanoparticles were produced for a direct comparison with titanium dioxide and nitrogen doped titanium dioxide thin films. The advantages and disadvantages of using nanoparticles to break down T&O's, such as geosmin and MIB, as an alternative method to using thin film coatings is also explored. Also discussed in this chapter is the idea behind the creation of core shell nanoparticles (gold and silver) by colloidal synthesis in an effort to develop a light emitting nanomaterial to initiate photocatalytic degradation of organic drinking water pollutants upon binding. The idea was that the gold and silver nanoparticles cause a chemiluminescent reaction, which would cause the photocatalytic materials to break down T&Os. This chapter introduces the theory of the techniques and methodology behind producing these nanoparticles, and the experimental details of such production

5.1 NANOPARTICLE USES AND OVERVIEW

Nanoparticles can be defined as a particle less than 100 nm in diameter or less than 100 nm in any one dimension. Particles that display unique properties that differ from the bulk equivalent are also referred to as nanoparticles. Unique optical properties, such as fluorescence and surface plasmon resonance, only occur at nanoscale. The materials produced to utilise these respective properties are citrate functionalised gold nanoparticles and silver nanoparticles. Titanium dioxide nanoparticles and nitrogen-doped titanium dioxide nanoparticles to investigate the

photocatalytic performance difference between thin films and nanoparticles. Modification of the band gap of semiconductor nanomaterials (TiO₂) through doping with nitrogen.

5.2 SURFACE PLASMON RESONANCE

Surface plasmon resonance (SPR) is a phenomenon that occurs on the molecular surface of precious metals such as gold and silver. Plasmon refers to the oscillation of electrons or “plasma” on the metal surface. The coupling of light with surface plasmon causes enhanced fluorescent effects of certain range of light depending on the metal used. The oscillating plasmon provide additional electrons for fluorescence to occur, boosting the effect of any fluorescent already occurring

5.3 CHEMILUMINESCENCE

Luminol is also widely used as a chemiluminescent reagent; the oxidation of luminol is carried out by reaction with hydrogen peroxide and horse radish peroxidase, the reaction scheme is outlined in Figure 11.

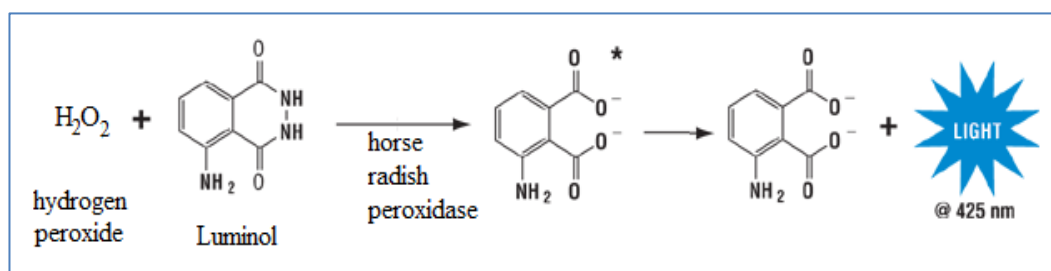


Figure 11: Reaction scheme showing oxidation of luminol.

It has been found that luminol can react with AgNO_3 in the presence of gold colloids to generate chemiluminescence at 425 nm^{94} , this is highlighted in Figure 12 which summarises the overall process.

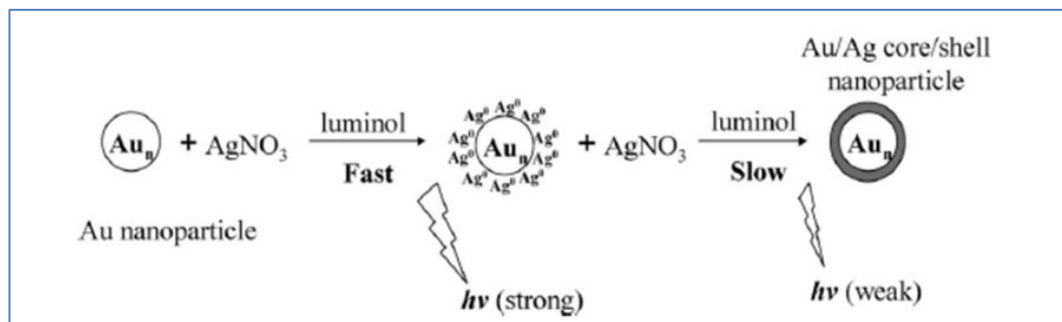


Figure 12: Catalysis model of Au nanoparticles in the CL reaction between luminol and AgNO_3^{94}

Silica nanoparticles are highly versatile materials that have been used in for a wide variety of applications. It has been shown that dyes can be incorporated within the silica nanoparticles and applications include SO_2 and O_2 gas sensors⁹⁵ and bioapplications for imaging⁹⁶. This section of the study focuses on the use of the chemiluminescence of luminol ($\lambda_{\text{em}} = 425 \text{ nm}$) to activate the photocatalysis of doped TiO_2 to break down T&O's. Luminol doped silica nanoparticles were produced with the idea revolving around activation of luminol (via gold or silver nanoparticles) releasing photons of light, which in turn will excite the fluorescent dye within the silica shell by Försters resonance energy transfer (FRET)⁹⁷. The gold core causes surface plasmon resonance enhancement as the dye's fluorescent emission, which then causes photons of higher visible wavelengths to irradiate the TiO_2 . Alternative methods are available for producing the plasmon boosting desired by the gold core. Other noble

metals such as silver have been shown to be more effective at some wavelengths⁹⁸, however, they can be more difficult to prepare. An alternative to using a gold core is to use gold nanoparticle seeds (1-3nm in diameter). This method relies on a different citrate reduction method in order to reduce the gold at a faster rate and form smaller particles⁹⁹. These smaller gold nanoparticle seeds can be attached to the outer surface of a fluorescent nanoparticle and exhibit their plasmon boosting properties from the surface rather than the core. Additionally gold nanoparticle seeds can be fused together via additional gold deposition to form a gold shell¹⁰⁰. There are several methods therefore, of causing the plasmon boosting using gold nanoparticles and they are explored in this thesis. The various citrate nanoparticles produced are presented in Figure 13.

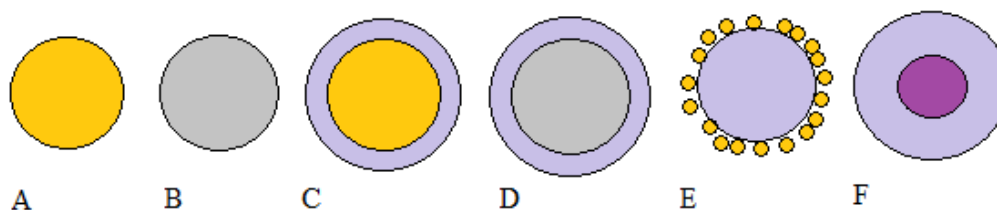


Figure 13: Various nanoparticles synthesised: A) Gold nanoparticle B) Silver nanoparticle C) Gold coated with silica nanoparticle D) Silver coated with silica nanoparticle E) Silica coated with gold nanoparticle seeds F) Luminol coated with silica nanoparticles

5.4 EXPERIMENTAL

5.4.1 PRODUCTION OF GOLD NANOPARTICLES

Gold nanoparticles were synthesised using a gold chloride reduction method following the standard Turkevich et al, Frens method¹⁰¹. The reaction involves reducing the gold in gold chloride and forming a gold precipitate¹⁰². 0.0128 g HAuCl₄.3H₂O, obtained from Sigma Aldrich (product code: 254169), was dissolved in 100 ml water in a 250 ml conical flask and brought to the boil. 1.008 g sodium citrate was dissolved in 100 ml water (approx. 1%) 3.5 ml of this solution was pipetted into the conical flask, the solution was kept on the boil for a further 15 min and then allowed to cool. The reaction equation is as follows:



5.4.2 COATING OF GOLD NANOPARTICLES

The coating of gold colloids with silica allows manipulation of the surface interaction potential, which makes it possible to disperse the colloids in a wide range of solvents¹⁰³. Gold nanoparticles previously prepared were then coated with silica using the following method. 0.256 g of Polyvinylpyrrolidone (PvP) was put into 10 ml water and ultrasonicated (model: 1510 Branson ultrasonicator) for 15 min. 3.45 ml of PvP solution prepared was added to 40 ml colloidal gold nanoparticle solution and stirred for 20 min. The PvP functionalised gold nanoparticle suspension was added to 80 ml ethanol then 4.2 ml of 29% ammonia in water was added and stirred for 15 min. 2 ml of Tetraethyl orthosilicate (TEOS) was added to the mixture, this causes the coating of the gold nanoparticles. After each hour 2 ml TEOS is added for 3 hours (6 ml TEOS added in total)

5.4.3 PRODUCTION OF SILVER NANOPARTICLES

Silver nanoparticles were synthesised using a reduction of citrate method¹⁰⁴. 0.011 g AgNO₃ was added to 50 ml water and was heated until boiling. 0.0587 g Sodium citrate was dissolved in 5 ml water and added drop-wise to the boiling solution. The nanoparticle suspension was then stirred vigorously and heated until the mixture turned yellow.

5.4.4 COATING OF SILVER NANOPARTICLES

Silver nanoparticles previously prepared were then coated using a modified Stöber method¹⁰⁵. 0.2598 g PVP was added to 10 ml water and ultrasonicated for 15 min. 3.45 ml of the PVP solution prepared was added to 35 ml colloidal solution and stirred for 20 min. 4.2 ml of 29% ammonia in water was then added to 100 ml ethanol, 6.57 ml of this solution was added to the PVP-colloid solution. 66.3 µl TEOS solution was precisely measured using a graduated pipette and added to the colloid solution then left to stir for 3hr.

5.4.5 PRODUCTION OF LUMINOL DOPED SILICA NANOPARTICLES

Luminol doped silica nanoparticle were produced by a modified Stöber method¹⁰⁶. 67 ml ethanol was added to 2.28 ml ammonium hydroxide and 1.68 ml H₂O then stirred in a conical flask. 0.28 ml tetraethylorthosilicate (TEOS) was added to the mixture. Then 0.0018 g luminol was added to 0.001 ml 3-aminopropyltrimethoxysilane (APS) of 1 µl APS in 0.5 ml ethanol and then added to

the TEOS mixture. This was stirred for 3 hrs, and then centrifuged. The mixture was redispersed in ethanol.

5.4.6 COATING OF SILICA WITH GOLD NANOPARTICLES

The surface of the luminol silica nanoparticles were functionalised with APS. Gold nanoparticles have an affinity for amines and the APS provides a surface coupling agent. 0.05 ml of APS was added to 50 ml of ethanol containing 0.01 g of the luminol doped silica nanoparticles. The solution was heated at 80°C for 1 hr so that the APS would react on the surface of the silica. The particles were centrifuged and re-dispersed in ethanol to remove excess APS. Gold colloid 5 ml (stock as prepared) was added to the surface functionalised luminol silica.

5.4.7 PRODUCTION OF TITANIUM DIOXIDE NANOPARTICLES

Titanium dioxide nanoparticles were synthesised by a sol gel method¹. 5.2 g of titanium isopropoxide was dissolved in 10 ml ethanol and then hydrolysed with 50 ml of distilled water. A white precipitate was produced instantly and stirred for 10 min. The precipitate was separated by decantation and washed with distilled water for complete removal of ethanol. To the precipitate, 10 ml peroxide was added slowly as this thickens with time into a gel. The gel was annealed at 300°C to give un-doped TiO₂ nanoparticles. The temperature was varied on different occasions of the

nanoparticle synthesis. However too high a temperature caused the gel to burn, so 300°C was found to be the best temperature to give TiO₂ un-doped nanoparticles.

5.4.8 PRODUCTION OF NITROGEN DOPED TITANIUM DIOXIDE NANOPARTICLES

Nitrogen doped titanium dioxide nanoparticles were produced from the same sol-gel method as the undoped titanium dioxide nanoparticles. However, for the N doping the gel mixture made for TiO₂ nanoparticle synthesis was split in half so approximately 2.5 ml of TiO₂ was doped with 0.125 ml (5% N-doped) of ethylmethanamine and then this was annealed at 200°C⁸⁹. Annealing nanoparticles at a higher temperature caused the nanoparticles to burn, leaving a residual organic. This is perhaps because the nanoparticles were dried in air and too much oxygen was present for the annealing stage.

PART II

EXPERIMENTAL AND ANALYTICAL TECHNIQUES

The aim of this Chapter is to explain the experimental procedure behind thin film production and provide the methodology used in order to produce the following coatings; titanium dioxide, nitrogen doped titanium dioxide, molybdenum doped titanium dioxide and erbium doped titanium dioxide.

6.1 TITANIUM DIOXIDE FILMS

The deposition of titania (TiO_2) and doped-titania coatings by magnetron sputtering was a major goal of the project. Two different rigs were used and the first one is shown in Figure 14. This rig was used for the deposition of TiO_2 , N- TiO_2 and Mo- TiO_2 thin films. The magnetron sputtering rig uses two magnetrons that were fitted with titanium targets (99.5% purity), powered by DC or pulsed DC power supplies. A third magnetron can be fitted with a dopant target (e.g. molybdenum); if a transition metal dopant is required. Alternatively, dopant gases (e.g. nitrogen) are introduced to the chamber during the deposition process. Substrate rotation during sputtering is very important as sputtering operates in a 'line of site' mechanism and therefore the constant rotation of the substrate allows uniform deposition of all the target materials across the substrate.

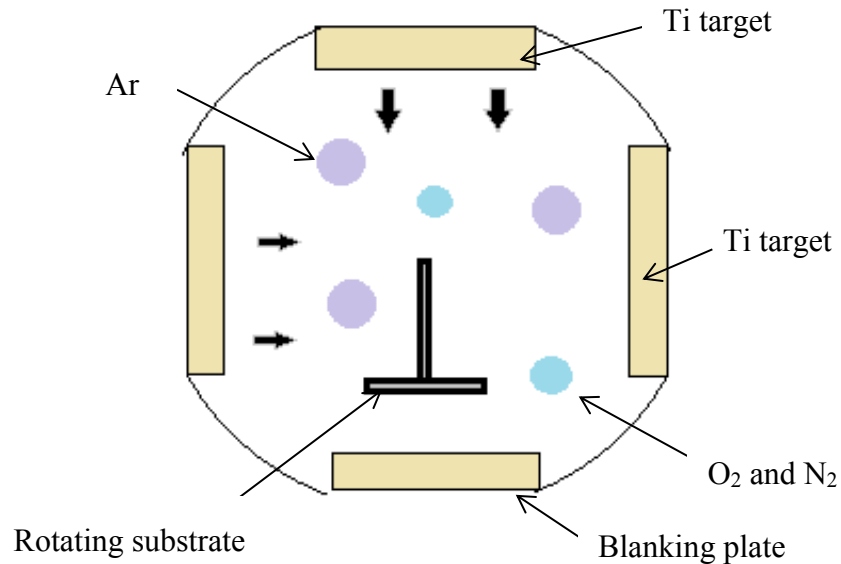


Figure 14: Magnetron sputtering chamber set up plan view, two titanium targets and a target for transition metal dopants, when required

6.1.2 TiO₂ COATINGS AND DOPED TiO₂ COATINGS

Thin films were deposited using reactive magnetron sputtering on a *Teer Coatings UDP 450 coating system* (Figure 15). Two titanium metal plate targets (99.5% purity) were used for the deposition of TiO₂. Argon (99.998% purity) as the working gas and oxygen (99.5% purity) as the reactive gas were added to the chamber. The working pressure was 0.1 Pa. Advanced Energy Pinnacle Plus pulsed DC power supplies were used to power the titanium magnetrons and an RF supply was used to bias the substrates.



Figure 15: Teer coatings Ltd. UDP450 magnetron sputtering rig

Glass microscope slide substrates (25mm x 50mm) were ultrasonically cleaned in acetone prior to loading into the chamber in order to remove surface contaminants. The substrates were aligned on a flat plate parallel to the surface of the metal targets at a distance of 150 mm from the target plane. A rotational speed of 10 rpm was applied to the substrates to ensure the substrate gets an even coverage, as magnetron sputtering builds up the coating over time. The chamber is evacuated using a rotary pump and an oil diffusion pump to a pressure less than 2×10^{-3} Pa. This level of vacuum was chosen to ensure that background levels of contamination (water vapour, oxygen, pump oils) was minimised in the deposited films. Once the chamber reached the desired pressure, water-cooling was introduced to the magnetrons to prevent the titanium targets from overheating. Argon gas was added to the chamber in order to raise the pressure to a working pressure of 0.13 Pa, which has previously been found to be suitable for the

deposition of titania coatings⁹². A standard set of operating conditions were used for the deposition of all the titania and doped titania coatings (unless otherwise indicated). The power supply for the Ti targets was set to 1000 W per target, pulse frequency of 100 kHz and a pulse off time of 4 μ s, giving a duty cycle when the magnetron operates of 60%. At this power, the average target voltage was approximately -300 V and the average current was approximately 3.3 A. The amount of oxygen was controlled using an optical emission monitor, using conditions known to produce stoichiometric TiO₂¹⁰⁷. As oxygen was added to the chamber, the glowing plasma changes colour from blue to pink, this can be observed in Figure 16. No additional heating was used during the coating process and the temperature did not exceed 200 °C during the process. The coating run time was 1.5 hours, after which the substrate was cooled down to room temperature and the chamber returned to atmospheric pressure. The sputtered films were post deposition annealed at 600 °C for 30 min in air.

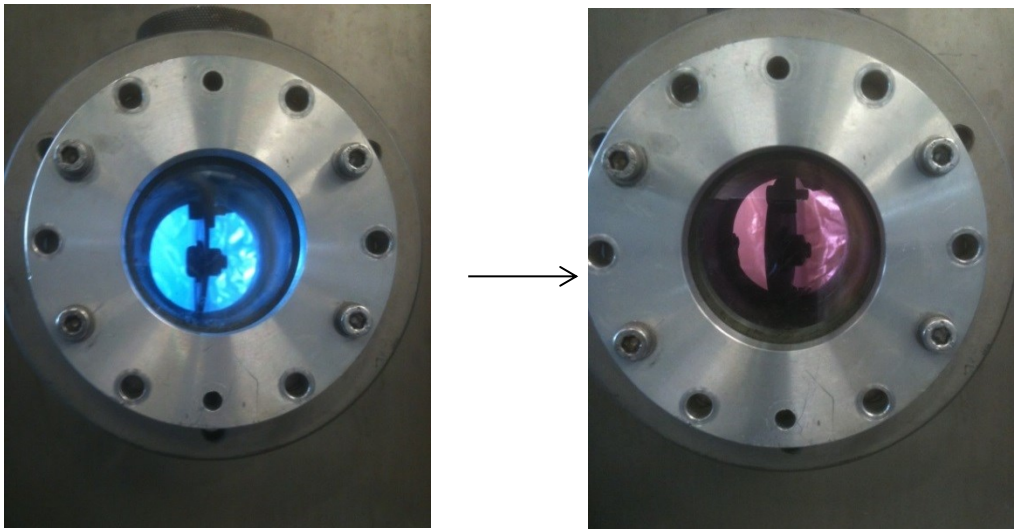


Figure 16: A) Inside the magnetron chamber argon gas only discharge with Ti target B) After the addition of oxygen to the argon gas magnetron chamber

The films produced *via* magnetron sputtering are listed in Table 5 with the experimental conditions and the abbreviated sample ID for each film used throughout this document. All titanium dioxide films were sputtered under the same conditions, which are described above, the only thing that varied from film to film was the deposition time and the annealing time in air in the oven.

Table 5: Titanium Dioxide thin film samples produced

Sample	Sample ID	Power (W)	Frequency (kHz)	Base chamber pressure (Pa)	Deposition time (min)	Time annealed in oven (min)
Titanium dioxide coating 1	C1	1000	100	1.2×10^{-3}	60	30
Titanium dioxide coating 2	C2	1000	100	1.1×10^{-3}	90	35
Titanium dioxide coating 3	C3	1000	100	1.1×10^{-3}	90	30
Titanium dioxide coating 4	C4	1000	100	1.3×10^{-3}	90	40

6.1.3 NITROGEN DOPED TITANIUM DIOXIDE FILMS

Doped thin films were produced by the same method above, with the exception that 7sccm of nitrogen gas was introduced to the chamber, in addition to the oxygen and argon, during the deposition process. The volume of nitrogen gas added was based on a previous study where 7sccm produced 1 at% nitrogen doped TiO₂ films¹⁰⁸. The deposition time for these films varied between 80 and 90 minutes, whereas the annealing time was fixed at 30 minutes, as shown in Table 6. The deposition time was varied to see the effect deposition time had on the thickness of the thin films produced

and the annealing time of 30 minutes was chosen based on the best post sputtered annealing times to produce anatase phase thin films in a previous study⁹⁰. All other deposition conditions were kept the same as the titanium coatings, as described above.

Table 6: N-Doped titanium dioxide coatings produced

Sample	Sample ID	Power (W)	Frequency (kHz)	Base chamber pressure (Pa)	Deposition time (min)	Time annealed in oven (min)
Nitrogen doped-Titanium dioxide coating 1	NC1	1000	100	1.3×10^{-3}	90	30
Nitrogen doped-Titanium dioxide coating 2	NC2	1000	100	1.4×10^{-3}	80	30
Nitrogen doped-Titanium dioxide coating 3	NC3	1000	100	1.2×10^{-3}	90	30
Nitrogen doped-Titanium dioxide coating 4	NC4	1000	100	1.3×10^{-3}	90	30

6.1.4 MOLYBDENUM DOPED TITANIUM DIOXIDE FILMS

In addition to the N-doped coatings, molybdenum doped coating were also investigated. This method is similar to the method used to produce pure titanium dioxide thin films except that a third target (Mo) is fitted into the chamber. To produce

a molybdenum-doped titanium dioxide thin film the Mo target is sputtered at a lower power than the Ti targets; typically 180W to give a dopant level of 6-7 at.%. The run time and annealing time of the films are given in Table 7 and all other conditions were kept the same.

Table 7: Molybdenum Doped titanium dioxide coatings produced

Sample	Sample ID	Power (W)	Frequency (kHz)	Base chamber pressure (Pa)	Deposition time (min)	Time annealed in oven (min)
Molybdenum doped- Titanium dioxide coating 1	MoC1	1000	100	1.2×10^{-3}	100	30
Molybdenum doped-Titanium dioxide coating 2	MoC2	1000	100	1.1×10^{-3}	90	35
Molybdenum doped-Titanium dioxide coating 3	MoC3	1000	100	1.3×10^{-3}	95	30
Molybdenum doped-Titanium dioxide coating 4	MoC4	1000	100	1.2×10^{-3}	90	40

6.1.5 SUBSTRATE PREPARATION

The thin films were deposited on standard microscopic glass slides. The glass substrates were cleaned very thoroughly to remove all traces of contamination such as finger prints, grease/oil, which can have negative effects on the thin film surfaces. The

substrates were cleaned with copious amounts of deionised water to help remove contaminants, acetone was also used in order to remove any organic components that could be present on the surface. The substrates prepared contained a piece of tape so that this would create a step in the coating (Figure 17) and after the deposition process it would be possible to calculate the coating thickness using a surface profilometer (further described in section 8.3).

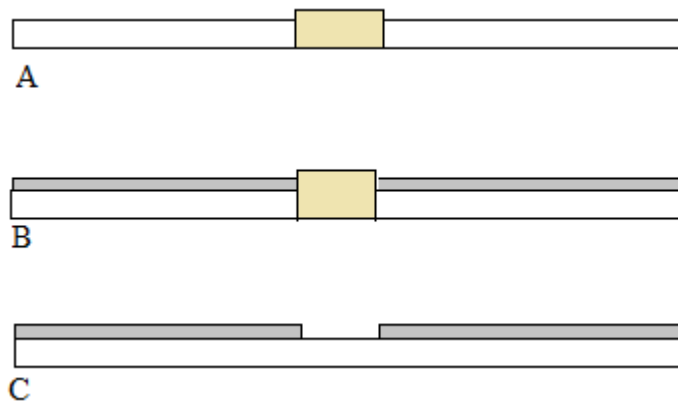


Figure 17: Schematic of substrate preparation to create a step. A) Tape covering part of the substrate B) Substrate after the deposition process C) Removal of the tape to creates a step between the substrate and thin film

6.2 POWDER COATING RIG

The rig used for the erbia doped titanium dioxide coatings differs from the Teer rig, in that the targets are formed from loosely packed powders¹⁰⁹. In this case titanium dioxide powder is sputtered to produce titanium dioxide coatings and titanium dioxide powder with erbium oxide powder is sputtered to produce erbium doped titanium dioxide coatings. The powder coating rig is pictured in Figure 21 where visible differences from Figure 18 can be observed.



Figure 18: Powder coating rig

The powder sputtered rig is similar to the Teer rig in terms of operation, however, the chamber set up differs. The substrate holder is fixed and sits above the target as can be observed in Figure 19, where a plan view of the rig can be seen. A glowing plasma inside the chamber can be observed in Figure 20.

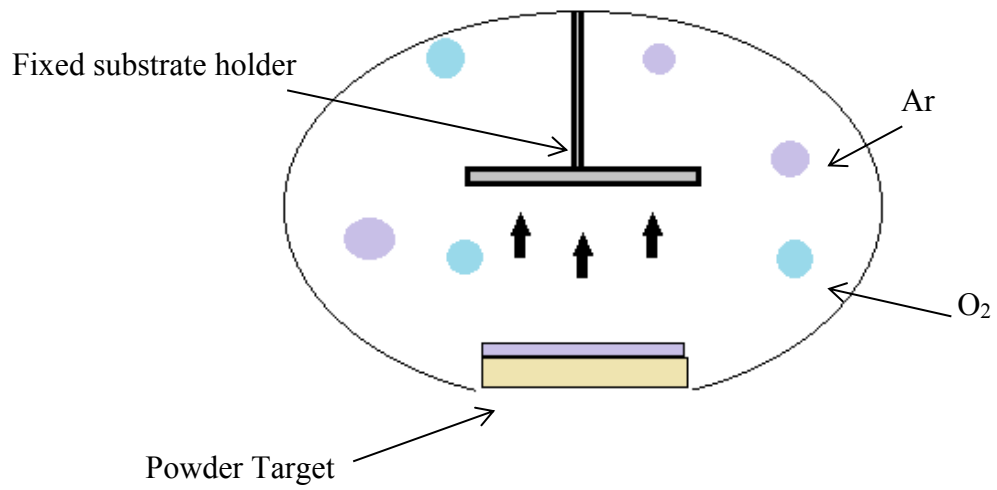


Figure 19: Powder target, magnetron sputtering chamber set up plan view



Figure 20: Glowing plasma inside the magnetron sputtering chamber during deposition

6.2.1 ERBIUM DOPED TITANIUM DIOXIDE THIN FILMS

Erbia doped titanium dioxide films were produced using powder from materials that can easily be mixed and spread across a recessed plate to make a sputter target. The materials used were titanium dioxide PC500 obtained from Crystal Global (CristalACTiVPC500); often used as a commercial standard for TiO₂ and erbium oxide powder obtained from Sigma-Aldrich (product code:289248). The powder is mixed together to produce a blended target. The amount of erbium oxide was controlled so that 5% at, 7.5%, 10%, 12.5% atomic weight of erbia was in the target composition. The blended powder targets all weighed a total of 15g.

6.2.2 PREPARATION OF POWDER TARGETS

Blended powder targets were prepared using TiO₂ PC500 powder and various amount of Er³⁺ powder. The total mass of the powder was 15g to cover entirely the copper backing plate. The powder blend was calculated based on the atomic percent concentration (at.%). Using this loosely packed blended powder targets allows for the ability to prepare targets of different compositional ratios. The composition of the powder targets were based on changing the at.% of the dopant. The at.% of the Erbium (Er) dopant of the various targets are listed in Table 8.

Table 8: Atomic percent ratio of the dopants for the TiO₂: Er powder targets

Target name	Atomic percentage of Er dopant at.%
TiO₂:Er 1	5
TiO₂:Er 2	7.5
TiO₂:Er 3	10
TiO₂:Er 4	12.5

The titanium dioxide powder used was industry standard PC500, with a molecular weight of 79.88 g mol⁻¹. The erbium oxide powder (Er³⁺) had a molecular weight of 382.52 g mol⁻¹. It is therefore possible to calculate the total mass of each compound needed in order to produce a target with the at.% listed in Table 8. These masses are listed in Table 9.

Table 9: The total mass of the blended powder targets

Target name	Compound powder target mass(g)	
	TiO ₂ PC500	Er ³⁺
TiO ₂	15	0
TiO ₂ : Er 1	11.98	3.02
TiO ₂ : Er 2	10.80	4.20
TiO ₂ : Er 3	9.79	5.21
TiO ₂ : Er 4	8.91	6.09

The preparation method was kept the same for each target. The mass of the powder was measured to 2 decimal places using a balance. The powder target material was then inserted into a glass bottle and left to mix on a rotator for half an hour to ensure that the target was completely blended. The blended powder target material was then distributed across a 2 mm deep circular copper backing plate on the magnetron plate and was tamped down using a 1 kg steel cylinder to ensure uniformity of the target surface.

6.2.3 OPERATING CONDITIONS

A standard set of operating conditions were used for the deposition of these titanium dioxide coatings and the erbium doped titanium dioxide coatings produced

from a powder (unless otherwise indicated). The power supply was initially set to 100 W, pulse frequency of 250 kHz and a pulse off time of 2 μ s, The power was increased by approximately 25 W per min until the power reached 250 W, this was to stop the target overheating. At this power, the target voltage was approximately -260 V and the current was approximately 0.9 A. The argon and oxygen flow rates were 15 sccm and 20 sccm respectively. The coating run time was 3 hours, after which the substrate was allowed to cool down and then the chamber returned to atmospheric pressure. The sputtered films were post deposition annealed at 600 °C for 30 min in air. The coating run times for these films were varied, along with the distance that the substrate sat from the target, this was to produce the best coatings possible. Deposition conditions were chosen to produce stable arc free conditions, and the deposition rates were calculated and the variation in deposition thickness was recorded. The optimum deposition rate of 1.58 nm·min⁻¹ was achieved in run 7 where the run time was 5 hours (Table 10).

6.2.4 DISTANCE BETWEEN SUBSTRATE AND TARGET

The distance between the substrate and the target is an important experimental variable. The distance is the pathway the sputtered atoms travel to get to and condense on the surface of the substrate from the target. Given this, it is assumed that a shorter pathway would lead to a thicker film, i.e. an increased deposition rate. However shorter pathways can lead to a localised adhesion failure of the coating and therefore causing the coating to delaminate from the substrate surface in stressed areas. The distances

tested in the experimental runs are described in Table 10. The substrate material was changed, both glass and silica were tested. It was concluded that glass was the preferred substrate, as problems arose with analytical characterisation due to the thickness of the films coated onto the silica substrate.

Table 10: Individual run conditions for erbia doped titanium dioxide films

Run	Target	Deposition Time (hrs)	Distance from the substrate (cm)	Substrate	Thickness (nm)	Deposition rate (nm·min⁻¹)
1	TiO ₂	3	7	Glass	100	0.55
2	TiO ₂	5	7	Glass	385	1.28
3	TiO ₂ 5% Er	3	7	Glass	168	0.93
4	TiO ₂ 5% Er	4	5	Glass	387	1.61
5	TiO ₂ 5% Er	4	5	Glass	341	1.42
6	TiO ₂ 10% Er	5	5	Glass	306	1.02
7	TiO ₂ 7.5% Er	4	5	Glass	278	1.58
8	TiO ₂ 7.5% Er	4	5	Silica	100	0.42

9	TiO ₂ 12.5% Er	4	5	Glass	270	1.13
10	TiO ₂ 12.5% Er	4	5	Silica	120	0.5
11	TiO ₂ 12.5% Er	5	5	Glass	302	1.01
12	TiO ₂ 12.5% Er	5	5	Silica	218	0.72

This chapter discusses the range of analytical techniques, which were utilised to fully characterise the thin films and nanoparticles produced. The surface morphology, film quality and film structure were obtained by imaging the samples by scanning electron microscopy (SEM) and transmission electron microscopy (TEM), images provided allowed the assessment of the sample quality. Surface topography was analysed by surface profilometry and white light surface profilometry and provided information about the surface roughness and thickness. X-ray diffraction (XRD) and Raman spectroscopy provided spectra allowing the crystallinity to be determined and the material to be identified. Energy dispersive X-ray spectroscopy (EDX), X-ray photoelectron spectroscopy (XPS) and inductively coupled plasma mass spectroscopy (ICP-MS) provide the elemental composition of the materials produced. Also in this chapter band gap calculations and photocatalytic tests are discussed along with the gas chromatography mass spectrometry (GC-MS) method used in order to detect the decomposition of taste and odour compounds broken down by the nanoparticles and thin films produced.

7.1 SEM

Scanning electron microscopy (SEM) was used to study the surface morphology of samples at high magnification. SEM analysis usually requires conductive samples that are stable under high vacuum conditions- thin films are therefore very suitable for SEM analysis. The resolution of the SEM can approach a

few nm and it can operate at magnifications that are easily adjusted from about 10X - 300,000X¹⁰⁰.

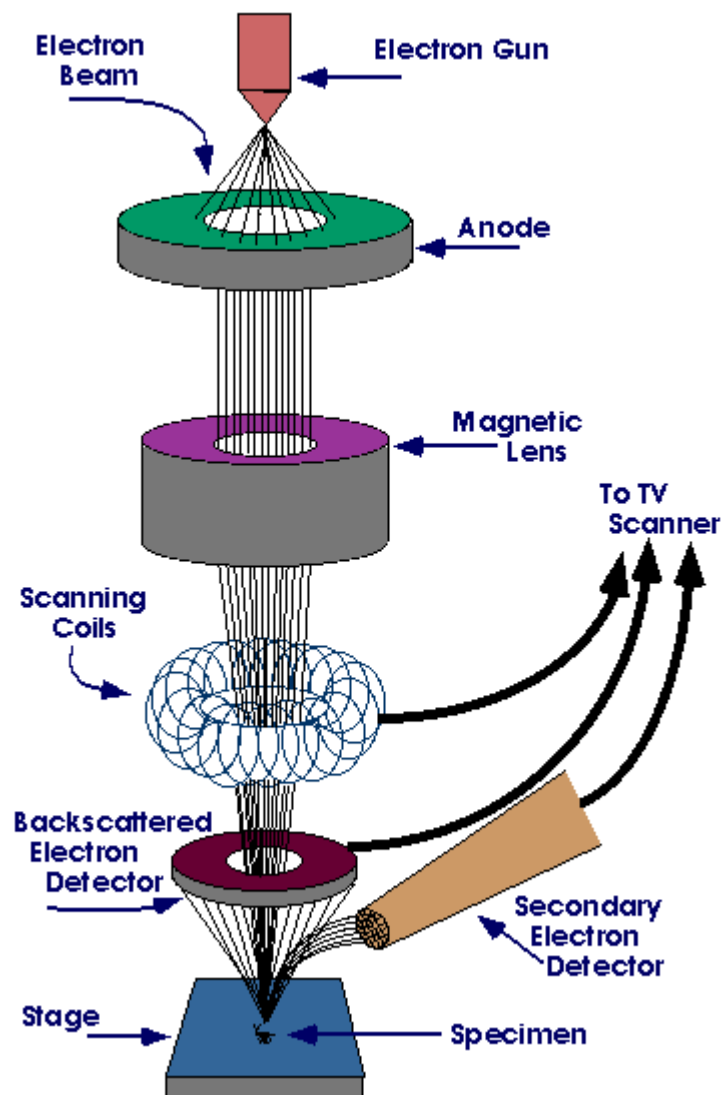


Figure 21: SEM schematic⁷⁵.

In the SEM (schematic shown in Figure 21) the source of electrons or gun emits electrons, which are accelerated to an energy between 1kV and 40kV¹¹⁰. The anode

plate forces the electrons into a stream (electron beam). The magnetic lens creates a magnetic force that directs the path of the electron beam. The fine beam of electrons is rastered across the specimen by the scan coils (rolls of wire that face each other to make a magnetic field that pushes the beam from side to side) and the number of secondary electrons produced from each point of the sample is counted by a detector. The computer measures the electrical current from the detector and turns it into an image on the screen. Depending on the height, and the shape, of the sample at each raster we get black, grey or white dots that create the image on the screen. The image is created in a grey scale that depends on the number of electrons detected. The SEM then provides a clear topographical image of a sample surface. The use of SEM requires little sample preparation, provided that the specimen is vacuum compatible. The sample normally needs to be conducting but if the sample is an insulator, it can be coated with a thin (approx. 10nm) conducting film of gold or carbon. In following this approach care must be taken to avoid producing a non-uniform coating, which might hide or distort surface features. SEM analysis of the films and nanoparticles were carried out using a *Carl Zeiss Ltd. Supra 40VP SmartSEM*.

7.2 TEM

In transmission electron microscopy, an electron beam is transmitted through a sample. The sample must, therefore, be very thin (~50nm) so that it is transparent to the electron beam. TEM detects the size, shape and spatial arrangement of particles within a sample at the atomic scale. The electron gun emits electrons which are

accelerated to an energy of 100-400keV. The illumination produced is concentrated on the specimen by a condenser lens. The illumination axis is aligned with the axes of the objective and projector lenses by the beam alignment stage. The beam passes through the specimen and the objective lens focuses the electrons into a magnified intermediate image. (This process is highlighted in Figure 22). The image is further magnified by a second projector lens and the final image is formed on a fluorescent screen. The screen is coated with phosphor, which fluoresces green under electron bombardment. The TEM room is darkened to allow observation of image details without distraction. Preparation of TEM samples is often the most difficult and time consuming part of the analytical process. TEM analysis of thin film samples were carried out using a *JEOL JEM-200*.

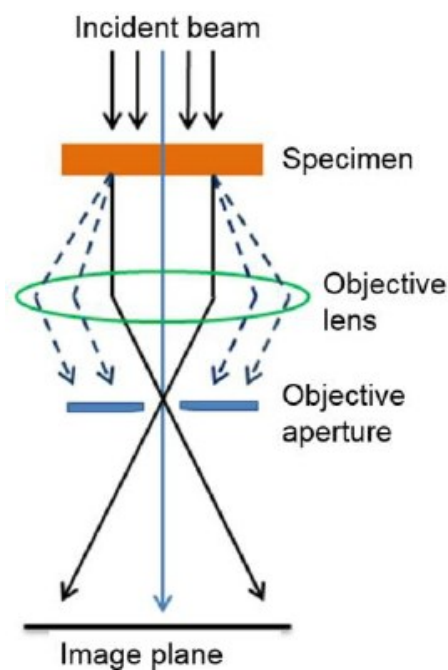


Figure 22: TEM schematic⁹⁰

7.3 SURFACE PROFILOMETRY

Surface profilometry measures step heights or trench depths on a surface by a mechanical profilometer. A step is formed in the coating by masking part of the substrate before thin film deposition, described in Figure 17. The thickness of the coating is measured by traversing the sample under a stationary diamond stylus, the trace of the stylus is recorded digitally thus determining the step height between the substrate and the coating. Almost any sample that will not be deformed by the stylus can be measured very rapidly. This technique enables analysis of the surface of the films by providing information of the coating thickness. This method of surface profilometry can be somewhat limited as the stylus moves across the surface, and if the surface is very rough the stylus can provide a false result or can be prevented from moving across the surface altogether.



Figure 23: Detak II instrument at MMU

Surface profilometry measurements of various thin film coatings were carried out using a *Detak II* instrument (Figure 23).

7.4 WHITE LIGHT SURFACE PROFILOMETRY

White light surface profilometry uses an optical profile method where a white light source shines onto a sample surface through a filtering optical component, and is used to calculate surface roughness of thin films. The light is separated through a dispersive lens into its component wavelengths, each of which corresponds to a different z-coordinate in the optical axis. The data provided by the measurement from the scanning probe gives a three-dimensional map of the surface with measured distance values in each direction (Figure 24). These data may be used to calculate the roughness of the surface. In general, optical profilers have the same advantages as mechanical profilers; there is no sample preparation and a short analysis time. Two surface roughness terms are commonly used: average roughness R_a and root-mean-square roughness R_{RMS} . The R_{RMS} is the standard deviation.

$$R_a = \frac{1}{N} \sum_{i=1}^N |z_i - \bar{z}| \quad \text{Eq. 1}$$

For N measurements of height z and average height \bar{z} , the average roughness is the mean deviation of the height measurements and the root-mean-square roughness is the standard deviation.

$$R_{\text{RMS}} = \left[\frac{1}{N} \sum_{i=1}^N (z_i - \bar{z})^2 \right]^{1/2} \quad \text{Eq.2}$$

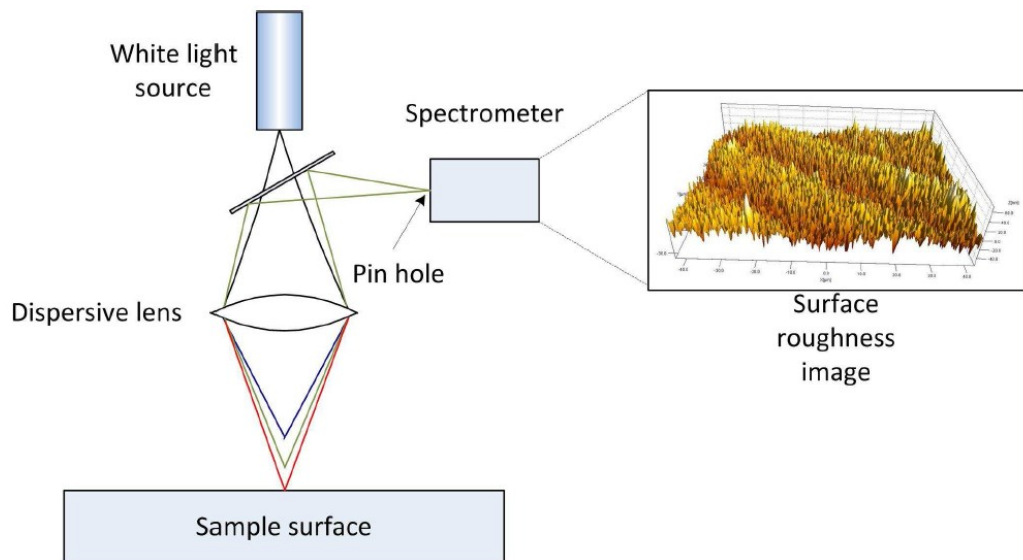


Figure 24: White light surface profilometry schematic¹¹¹

White light surface profilometry measurements of thin film coatings were carried out using an *Azygo, ZEmetrics ZEgage* instrument.

7.5 XRD

X-ray diffraction (XRD) is a powerful analytical technique for the identification of the crystal phases present in materials and works on materials in bulk or powder form. It also provides an opportunity to determine such structural properties of the material as grain size, preferred orientation and phase composition. The XRD technique is based on the scattered intensity of an X-ray beam hitting the sample as a function of incident and scattered angle, polarization and wavelength or energy. XRD measures the intensity of the diffracted beam as a function of angular position. The

wavelengths of the X-rays (0.154 nm for copper radiation) are similar to interatomic distances in solids and consequently, atoms can act as scattering centres. Diffraction occurs when the scattered X-rays are in-phase, which occurs at incident beam angles that are material specific. The nature of the diffraction can therefore reveal information about the structure and properties of the sample and be used to identify the phases present. The diffraction pattern produced includes the angle of diffraction, which is represented by Bragg's law¹¹²:

$$n\lambda = 2d \sin\theta \quad \text{Eq. 3}$$

Where d represents the spacing between planes of atoms in the material, n is an integer, λ is the wavelength of the incident x-rays and θ is the diffracting angle.

In the analysis of surface coatings XRD gives information on phases present, preferred orientation, crystalline size/strain and stress (intrinsic and extrinsic). All these properties listed can be varied with deposition conditions provided that the coatings are: of a suitable thickness, have crystalline phase present and are deposited on a suitable substrate. However, in this project the technique was only used to determine which phases were present.

7.6 RAMAN SPECTROSCOPY

Raman spectroscopy is a structural characterization technique. Lasers of 532 nm and 780 nm were used on a Thermo Scientific, DXR Raman Microscope model with OMNIC software. Raman spectroscopy was used to characterise the phase of titanium dioxide formed in the films and nanoparticles by comparing the Raman results

with standard samples and literature results previously reported¹¹³. Raman provides a unique chemical signature of a material. Raman can also highlight stress and geometric structural changes of a material as well as doping and chemical modification. Sample preparation is generally not required for Raman.

7.7 EDX

Energy dispersive X-ray spectroscopy (EDX) is a chemical microanalysis technique used in conjunction with scanning electron microscopy (SEM). EDX analyses X-ray emissions from the sample surface. Each element will emit X-rays with characteristic energies/wavelengths that can be identified and quantified. This method uses the X-ray spectrum of a solid sample bombarded by a focused beam of electrons. During an EDX analysis, the specimen is placed inside the scanning electron microscope and bombarded with an electron beam. The electron beam excites the atoms in the specimen causing them to eject electrons from their inner shells, a hole is thus created and filled by an electron from the outer high energy shell. The excess energy emitted as x-rays, are characteristic of the element and determination of their energy allows for identification of the elements in the specimen. This technique can therefore be used for obtaining elemental composition of the titanium dioxide and various metal dopants found in the thin films produced from magnetron sputtering. EDX analysis was carried out using *EDAX Inc. Apollo 40 SDD*.

X-ray photoelectron spectroscopy (XPS) employs a monochromatic X-ray source, which is focussed and directed toward the surface of a solid sample. X-rays penetrate the surface, interacting with and liberating electrons. Only electrons liberated near to the sample surface can escape to the surrounding vacuum (typically 10^{-6} Pa). The electrons are then detected and analysed (kinetic energy and number of electrons) by an electron spectrometer. XPS is based on the analysis of the kinetic energy of the photoelectrons emitted by the atoms when irradiated by a monochromatic X-ray beam. If the fixed energy of the incident beam is higher than the binding energy of the core electron of the atom, this electron can be removed. This photoelectron has a particular kinetic energy that is given by the Einstein relationship¹¹⁴:

$$E_k = h\nu - E_b - \Phi \quad \text{Eq. 4}$$

Where E_k is the kinetic energy (eV), E_b is the binding energy (eV), h is Planks constant, ν is the frequency of the incident X-rays (eV) and ϕ is the spectrometer work function (eV)

XPS is a non-destructive technique that is extremely surface sensitive and provides quantitative chemical analysis (At.%), typically accurate to 0.1 At.%. XPS is effective for detection of all elements except hydrogen and helium and can detect chemical states due to changes in the binding energy of electrons. X-ray photoelectron

spectroscopy (**XPS**) measurements were carried out using a *Thermo Scientific K-alpha spectrometer through EPSRC funded open access NEXIS programme*.

7.9 ICP-MS

Often properties of a material are effected by doping levels in the 10^{14} range, which means characterisation at the parts per billion (ppb) to sub-ppb levels. Inductively coupled plasma mass spectroscopy (ICP-MS) is capable of this degree of sensitivity. The information derived from ICP-MS is simply a mass spectrum of the sample. This includes a wealth of information. In one sampling, which can take less than one minute, information on almost all elements in the periodic table can be derived to at least low ppb levels. The mass spectrum contains not only elemental information but also isotopic information for each element. This can be useful to give a positive identification of elements.

Basic principles of the instrumentation:

1. An inductively coupled plasma for sample ionization
2. A mass spectrometer for detecting ions
3. A sample introduction system.

All of these components are critical for the high sensitivity found in ICP-MS.

ICP was used in this study to determine the amount of dopants in the thin films created when EDX was not successful in obtaining results, due to the detection limits of the instrument. This worked by completely dissolving the coatings from the glass and using the following method for ICP analysis of the samples. 4ml ultrapure water

added to 1 cm x 1 cm section from the thin film, added to 2 ml HNO₃ in a beaker placed on a hot plate at 80°C until the film had digested (approx. 1 hour). The solutions were diluted to 10 mL using deionized water (conductivity 18.2 mΩ) and analysed. A set of standards was used to create a calibration graph and allowed the quantification of the amount of erbium metal, molybdenum and titania in the various doped thin films

Inductively coupled plasma mass spectrometry (**ICP-MS**) measurements were carried out using a *Perkin Elmer spectrometer*.

7.10 PHOTOCORRELATION SPECTROSCOPY

Here, photon correlation spectroscopy (PCS) was used to estimate the size of the gold and silver nanoparticles. PCS uses dynamic light scattering (DLS) to infer particle size measurements. PCS works on the principle that the nanoparticles in a liquid move about randomly. This is known as *Brownian motion*. Brownian motion is defined as ‘*The random movement of particles in a liquid due to the bombardment by the molecules that surround them*’.⁷⁴ The speed of this random movement by the nanoparticle is related to its size: Small particles move quickly in a liquid and large particles move more slowly. Therefore, the size of the particles can be estimated by measuring this motion, and applying theoretical models. PCS was used to measure the size of the particles following nanoparticle synthesis, and measure the mean count rate (the mean number of particles) and attenuation (scattering intensity) of the particles. The particles were illuminated with laser light and the changes in intensity in the scattered light were recorded. This is known as dynamic light scattering (Figure 25).

The method provides an average particle size and particle size distribution. This procedure was carried out by adding the nanoparticles to a 1 x 1 x 5 cm plastic cuvette. The cuvette was then placed within a Zetasizer nano ZS which then estimated the particle diameter by dynamic light scattering¹¹⁵.

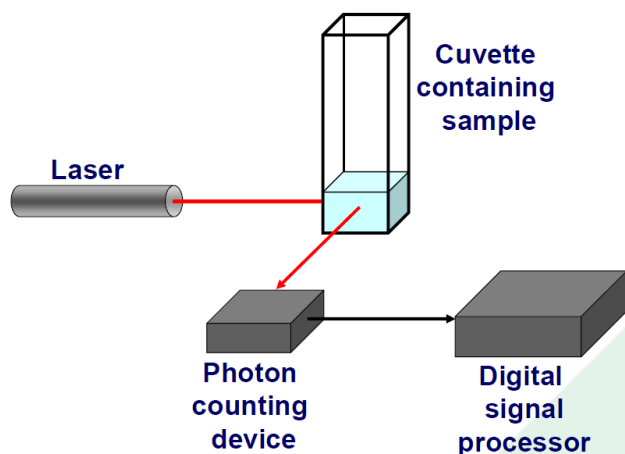


Figure 25: Photon correlation spectroscopy set up¹¹⁵

PCS measurements were obtained using a *Malvern Zetasizer nano ZS* (633 nm He-Ne laser, maximum power 5 mW), which estimates the particle diameters by *dynamic light scattering*.

7.11 FLUORESCENCE SPECTROSCOPY

Fluorescence spectroscopy analyzes the fluorescence from a sample. The excitation of fluorescent molecules leads to energy being lost as heat or emitted through fluorescence. The wavelength of the light (emission wavelength) is longer than the wavelength for the excited molecule, due to the loss of vibrational energy as heat. The light produces a high energy radiation, which passes through a

monochromator, at which the excitation wavelength of the beam may be selected, and it passes through the cuvette containing the sample. Upon excitation the fluorescence radiation of the sample occurs in all directions. The radiation passes through a second monochromator, which is held at right angles to the sample, which allows the emitted fluorescence light to enter the detector (Figure 26).

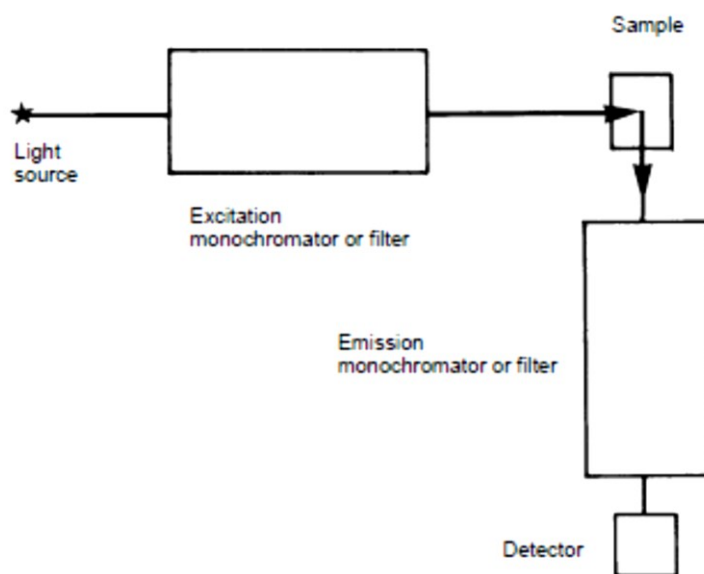


Figure 26: Schematic illustration of fluorescence spectrometer

7.12 BAND GAP CALCULATION

UV-Vis spectroscopy measures the optical properties (transmission and reflectance) of the thin film coatings, which are important in relation to photocatalytic activity. In this project the Tauc Plot method¹¹⁶ was used to determine the band gap of the thin films made.

$$\alpha h\nu = (h\nu - E_g)^{1/n} \quad \text{Eq.5}$$

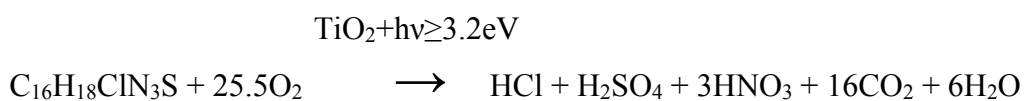
where α is the absorbance coefficient, h is the Plank constant, ν is the frequency of the light and n is exponent that denotes the nature of the sample transition. In the case of TiO_2 , indirect transition means that $n=2$. Therefore a plot of $(\alpha h\nu)^{0.5}$ versus $h\nu$ and extrapolating the linear region to the abscissa provides values for the band gap and band gap differences in a range of thin films. This method can be quite accurate, however, considering that the extrapolation relies on human estimation. The band gap value should be noted to be approximately ± 0.1 eV. UV-Vis absorption spectroscopy, for all of the studied nanomaterials and films, was carried out using a *Perkin Elmer Lambda 40 UV-Vis Spectrometer*.

For UV-Vis analysis of the gold and silver nanoparticles the solutions were placed in a 1 x 1 x 5 cm quartz cuvette. The entrance and exit slit widths were set as 2 nm each and the spectral region of 200 nm to 1100 nm was scanned for each sample. Deionised water was used as a blank sample for each measurement.

7.13 PHOTOCATALYTIC TESTING

Photocatalytic testing measures the activity of TiO_2 and its ability to break down, in this case, organic molecules. The photocatalytic activity can be determined by measuring the absorption over time of an organic dye solution, such as methylene blue. Methylene blue is a heterocyclic aromatic dye with a molecular formula of $\text{C}_{16}\text{H}_{18}\text{ClN}_3\text{S}$. When methylene blue contacts with the photocatalytic surface under

light irradiation the process called mineralisation takes place according to the following equation¹¹⁷ with easily measured colour change from blue to colourless:



A solution of methylene blue is produced and a piece of the coated substrate is cut to 2 cm² and placed in the methylene blue solution and left to soak in the dark for 30 min. The reason for soaking is so the initial absorbance readings are not affected by the absorbance of the dye onto the film. Then the beaker is placed under a UV lamp and the absorbance of the mixture at 664 nm is measured every second for 1 hour, in order to see the rate of dye degradation. The rate of degradation can be calculated by calculating the height of the absorbance peak compared to time, the gradient of this line gives the rate of degradation. The photocatalytic test equipment used is shown in Figure 27.

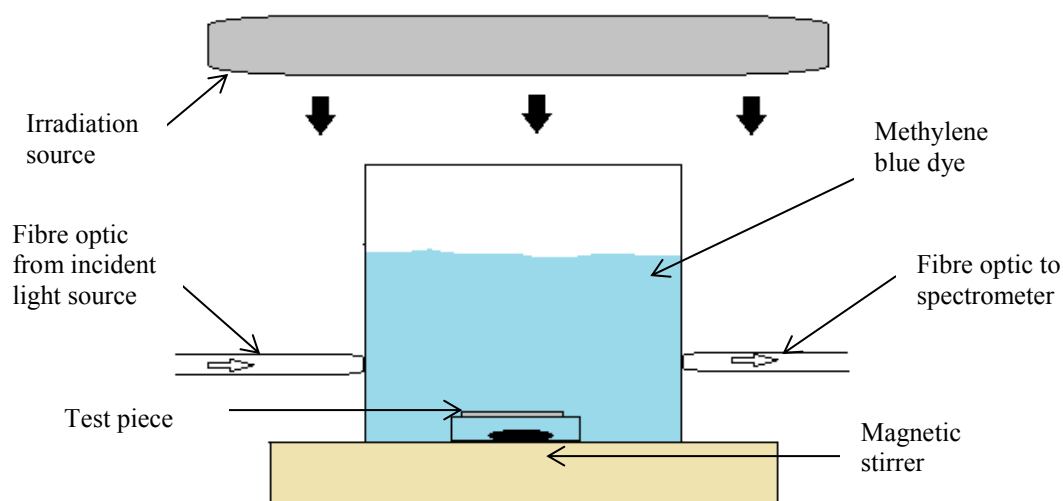
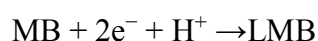


Figure 27: Schematic representation of methylene blue test

Degradation of dye under UV light irradiation in contact with a photocatalytic surface represents a relatively simple and convenient method for the assessment of photocatalytic activity. Since methylene blue dye has its own distinctive colour, the photocatalytic activity in this case is monitored by measuring the absorption of the dye solution over time. The absorption peak, at 664 nm, decreases over time in the presence of UV radiation and an active surface. The ability to break down methylene blue dye allows MB to act as a model organic pollutant to allow comparative tests of other pollutants to be performed. In addition, it is useful because of methylene blue's use commercially for dyeing and printing and so is in itself, a water pollutant. A stock solution of methylene blue was prepared (0.1M). The TiO₂ coated film on a glass slide was cut down to measure 2 cm² and placed in a 60ml glass cuvette. The methylene blue stock solution (60ml) was added to the cuvette and left to soak for 30 min. The

cuvette was placed under a UV lamp (Philips TL-D super 80 light source with power 15W) and the absorbance (664 nm) was recorded using a spectrometer every second for 1 hour.

Other features of methylene blue making it popular test method are low toxicity and high solubility in water. Thus, monitoring methylene blue aqueous solution absorption peak height at 664 nm, over a period of time, provides convenient and reliable method of assessing photocatalytic activity. Apart from that, it is reported that under certain conditions methylene blue may reduce through photosensitisation to the form of leuco-methylene blue (LMB), which is colourless and is an example of dye bleaching:



This reaction is likely to take place in acidic conditions so the pH control of the process is desirable in order to prove that the bleaching of MB is caused solely by photocatalytic process and not by LMB formation. (Monitoring the pH of the methylene blue solutions was achieved using a *Hanna Instruments pH 209* pH meter employing a standard pH electrode.)

The rate of degradation can be calculated by comparing the height of the absorption peak as a function of time. Degradation of dye under UV light irradiation in contact with a photocatalytic surface represents a relatively simple and convenient method for the assessment of photocatalytic activity. The film is pre-soaked for half an hour in MB. The reason for soaking is so the initial absorbance readings are not

affected by the absorbance of the dye onto the film. The first order rate constant, and therefore decomposition of MB can be calculated using the equation:

$$K_a = \ln(A_0 / A_t) \quad \text{Eq. 6}$$

Where A_0 – absorbance at time 0 and A_t – absorbance at the time of the experiment, a value for K_a was produced. The K_a value is rate constant for a chemical reaction known as dissociation in the context of reactions. The larger the K_a value, the more dissociation of the molecules in solution. Therefore, a higher K_a value shows high photocatalytic activity. Pilkington's (industrial company) Aktiv™ glass¹¹⁸ is used as a control in this experiment. Pilkington's Aktiv™ is a self-cleaning glass which breaks down organic dirt on the surface of the glass upon exposure to UV light.

7.14 GC-MS

Gas chromatography mass spectrometry (GC-MS) consists of a gas chromatograph (GC) coupled to a mass spectrometer (MS), by which mixtures of chemicals may be separated, identified and quantified. This makes GC-MS ideal for the analysis of the hundreds of relatively low molecular weight compounds found in environmental materials, and in this case, T&Os such as geosmin and MIB. In order for a compound to be analysed by GC/MS it must be sufficiently volatile and thermally stable. As mentioned in section 2.3.2 GC-MS has widely been used for the detection of geosmin and MIB. GC-MS analysis was performed on *Agilent technologies 7890BGC-MS (Figure 28)*.

Figure 28: Agilent technologies 7890B instrument

The equipment used for GC-MS generally consists of an injection point at one end of a chromatography column filled with substrate material and a detector at the other end (Figure 29). The sample is injected into the injection port with a needle and a syringe capable of delivering a known volume. The injection port contains a septum made from silicone to prevent the gases from escaping. The injection port is also maintained at a temperature at which the sample is vaporised immediately. The GC oven was programmed at a temperature gradient of $50^{\circ}\text{Cmin}^{-1}$, ramped at $10^{\circ}\text{C min}^{-1}$ to 200°C and at $20^{\circ}\text{C min}^{-1}$ to 220°C . A carrier gas such as hydrogen then drives the sample down the column at a constant flow rate. The column is a metal tube consisting of a polysiloxane coating. As the sample moves down the column the sample will interact with the surface of the column depending on the different molecular characteristics of the sample.

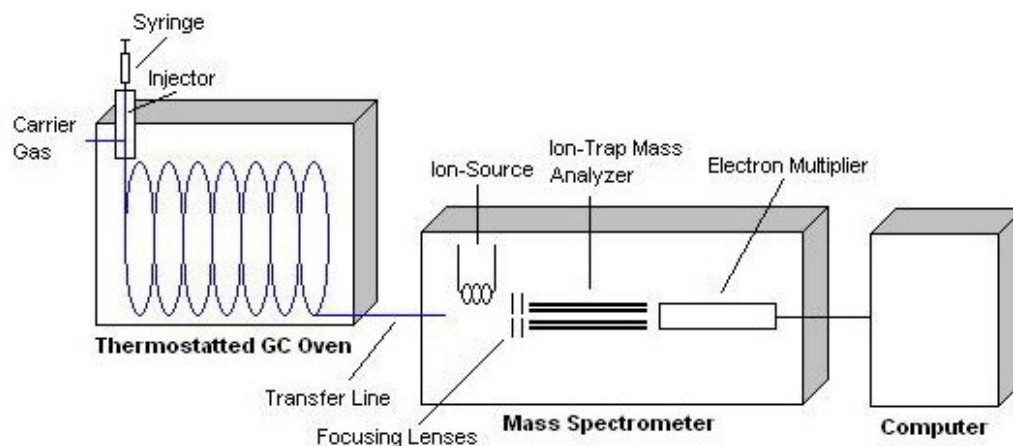


Figure 29: Gas-chromatography mass spectrometry structure¹¹⁹

The detector (mass spectrometer) measures the different compounds as they emerge from the column (compounds that don't adhere to the column will move through the column rapidly). The sample enters the ionisation chamber where an electron beam is accelerated by a high voltage. The molecules break into defined fragments on collision with electrons, each fragment is then accelerated along a curved path until they reach the detector. Charged particles then hit the detector forcing electrons to be accelerated away from the detector surface towards a second surface. This process generates more electrons bombarding the collector, this then results in a cascade of electrons reaching the collector and the instrument measures the load and records the mass that is proportional to the detector load. The MS instrument produces a spectral output as a series of peaks on a graph that is electronically stored and displayed on the computer monitor. Each peak represents a value for a mass of fragments. The peak height therefore, increases as the number of fragments detected with a single mass increases. The method condition parameters devised for detection

of geosmin and MIB is shown in Table 11. Method development of GC-MS analysis of the two taste and odour compounds was carried out and the best method condition parameters on the GC-MS available are shown in Table 11.

Table 11: GC-MS condition parameters

GC conditions		MS conditions	
Injection mode	Split mode, ratio 5:1	Scan Mode	m/z 40 to m/z 250
Inlet temperature	250°C	MS temperature	Source 230°C
Oven Temperature	50°C for 1 minute 10°C/min to 200°C, hold for 1 minute 20°C/min to 220°C, hold for 1 minute		

Preparation of geosmin and MIB samples were done by spiking known quantities of geosmin and MIB into aqua pure water, to make the correct concentration for the experiment. The solutions were stored in 20ml sample vials with rubber caps. For the geosmin and MIB standards the preparation method is as follows: 0.25ml geosmin in methanol (2mg/ml) diluted with ultrapure water in a 250ml grade A volumetric flask; 0.025ml 2-methylisoborneol in methanol (10mg/ml) diluted with ultrapure water in 250ml grade A volumetric flask.

The effect of geosmin and MIB concentration was tested; geosmin was diluted to 0.25, 0.5, 0.7, 1, 2, 4, 8, 50, 100, 1000, 2000ppm using an autopipete and MIB at the same concentrations. High concentrations were analysed using the GC-MS to determine the retention time of the compounds. A typical run time for a geosmin and MIB concentration was approximately 18minutes per analysis. The instrument had a cooling time to allow the injection port and oven to cool before the next sample was run, this was approximately 10 minutes as the GC-MS was ramped up to high temperatures (250°C) during the method. Two samples could be analysed in a hour allowing for approximately 12 samples a day. GC peaks were identified using the mass spec and the average peak height and peak area results were determined. Concentration of the geosmin and MIB peaks were determined by comparing the peak height data to that of the calibration curves. Occasionally it was important to ‘flush’ out the column with methanol as other students were sharing equipment and it was possible for contaminants to ‘stick’ on the inside of the column.

7.15 DEGRADATION OF TASTE AND ODOUR COMPOUNDS

Photocatalytic degradation of both geosmin and MIB was studied and conducted via a lab based test set up (Figure 30). The set up consisted of geosmin and MIB solutions prepared by spiking ultrapure water with the appropriate quantities of geosmin or MIB standards. The solutions were then irradiated with a 400W UV lamp in:

- a) The absence of TiO_2 (photolytic degradation)

- b) The presence of TiO₂ thin films produced via magnetron sputtering (photocatalytic degradation) (various forms of the doped TiO₂ thin films were also tested).

The solutions were tested in both light and dark conditions.

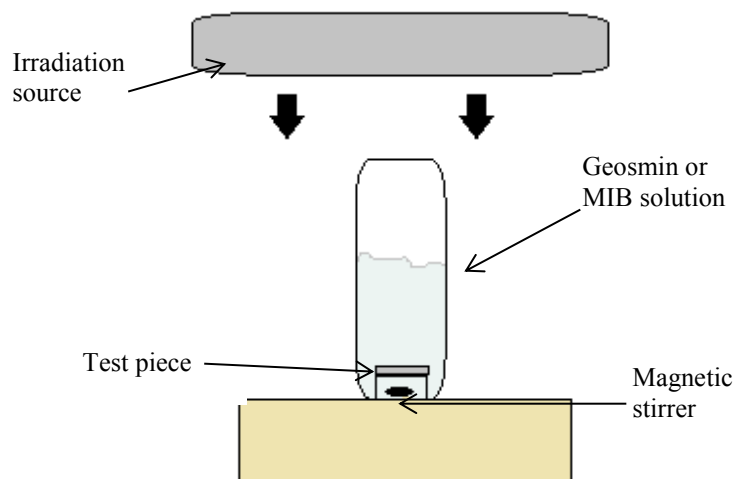


Figure 30: Set up of experiment to photocatalytically degrade T&O compounds

The setup of the experiment consisted of the geosmin or MIB solution stirred continuously under a UV lamp with sunlight being kept out (using a box to black out light). Aliquots of the solution were taken at 10min, 30min, 1hr, 1.5hr, 2hr, 2.5hr. These aliquots (1ml) was pipetted into 5ml sample vials (brown in colour to eliminate the effect of any light on the sample) and sealed with a cap. A polydimethylsiloxane fibre was injected to the headspace of the vial and injected into the manual injection port on the GC-MS. The geosmin or MIB peak is identified on the computer and the degradation of this peak height is recorded over time. The experiment was run for 2.5

hours. Allowing for cleaning of equipment and cooling of the GC oven, approximately two experiments could be run a day.



Figure 31: Test set up for degradation of taste and odour compounds

The films tested included TiO_2 , N-TiO_2 and Er-TiO_2 with the addition of other doped films, which included nitrogen and molybdenum. This test set up was repeated using a visible light source. Five replicates of each test was carried out to ensure that the degradation of geosmin and MIB for each set up was consistent and repeatable.

PART III

RESULTS AND DISCUSSION

This chapter presents the characterisation results for the following thin films; titanium dioxide, nitrogen doped titanium dioxide, molybdenum doped titanium dioxide and erbia doped titanium dioxide. The results and associated discussions are combined with the conclusions at the end of the chapter. The films all unique, possessed different surface morphology and composition and the significance of this is discussed in this chapter. An example of a typical titanium dioxide thin film produced from this study is pictured in Figure 32.

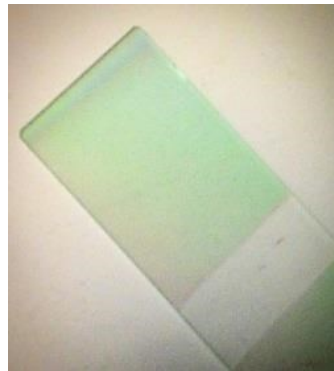
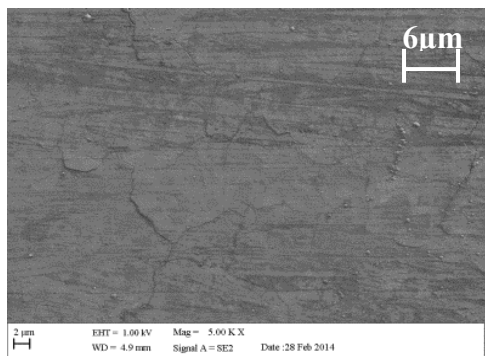


Figure 32: Image of TiO₂ thin film coating on glass substrate

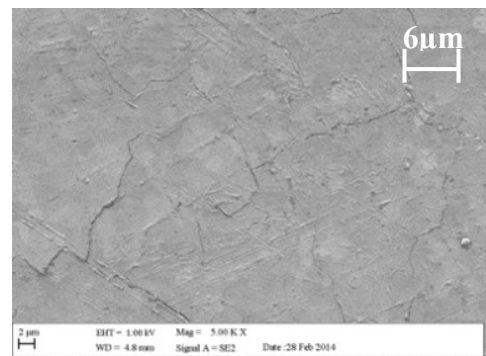
8.1 SEM RESULTS

SEM images reveal morphological properties of the thin films produced. Micrographs of the undoped titanium dioxide coatings and their surface topography's are shown in Figure 33. In the cases of C1 and C3, the SEM images show cracking in the film. The films were annealed at 600°C for a 35 minutes and 40 minutes

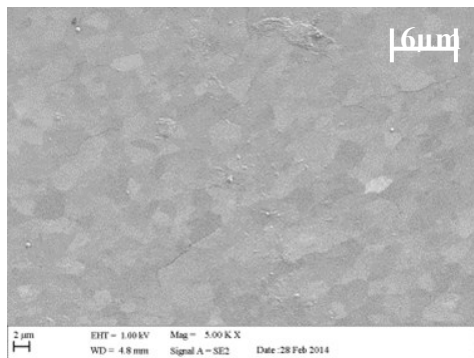
respectively, whereas the other films were annealed for 30 min. The longer annealing time can cause stress to the coating and the cracks to appear. In addition, it is also possible to see what appears to be a faceted surface. Images of the other coatings appear to be much rougher in appearance, with the presence of many small defects. It is presumed that this is due to scratches, contamination and debris present on the surface of the substrate prior to deposition, or possibly due to handling of the sample after coating.



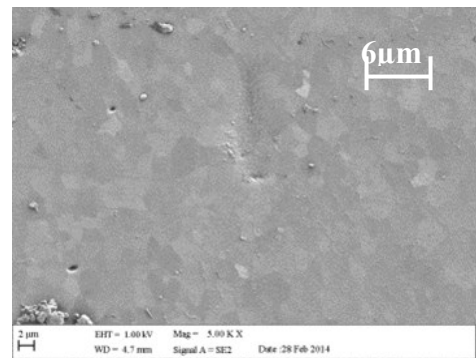
A



B



C



D

Figure 33: SEM images for A) C1 B) C2 C) C3 D) C4 undoped titanium dioxide thin films

The nitrogen doped titanium dioxide surface topography (Figure 34) was similar in appearance to that of the undoped titanium dioxide films. NC1 and NC2 show scratches and defects, whereas NC3 and NC4 have a faceted appearance. It is suggested in Raj et al¹²⁰ that the facets on the surface of the film are related to the formation of the anatase crystal phase, and the smoother the film the more likely it is to be rutile, as the crystallite formation on the surface of the film will be smooth for rutile and slightly 'rougher' on the anatase films.

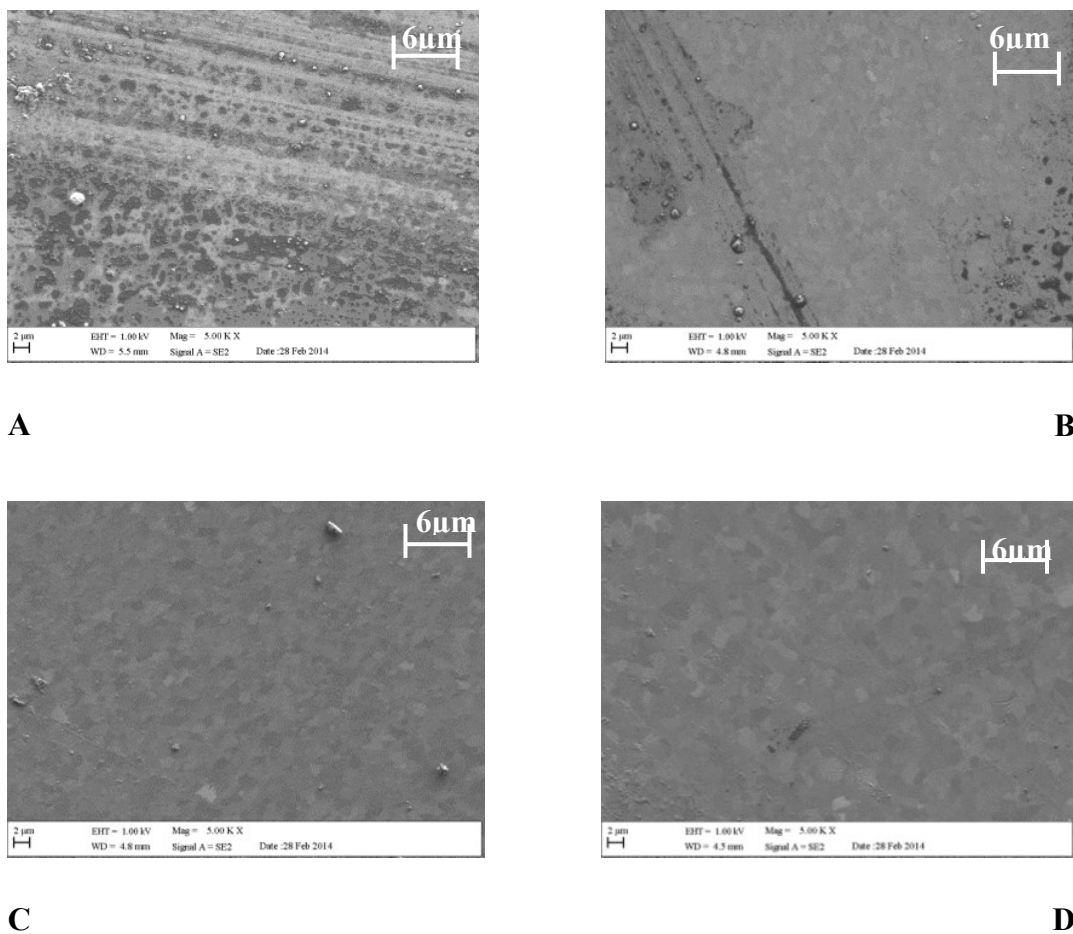


Figure 34: SEM images for A) NC1 B) NC2 C) NC3 D) NC4 nitrogen doped titanium dioxide thin films

Higher magnification SEM micrographs of the thin films revealed a regular nanostructured grainy surface morphology. A TiO₂ film (C1) is shown in (Fig. 35A), the incorporation of nitrogen appeared to result in a greater amount of surface spherical crystallites measuring ~100nm in size (Fig. 35B). The films are different to images shown in the literature of films grown by RF magnetron sputtering which have a more crystalline appearance¹²¹.

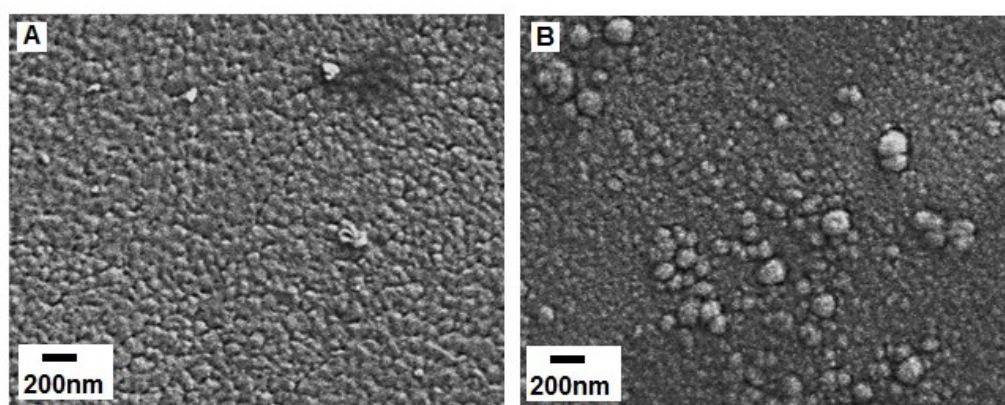
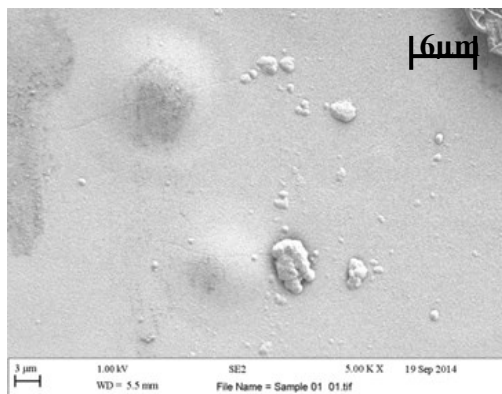


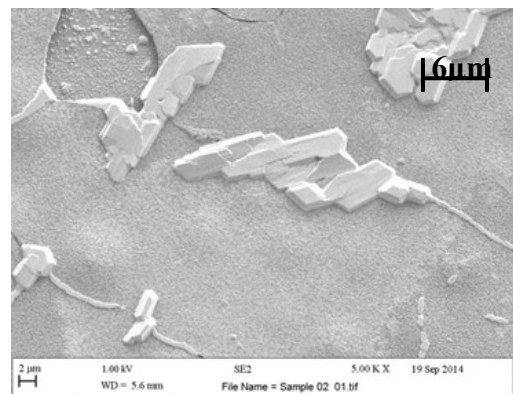
Figure 35: Scanning electron microscopy images of A) TiO₂ and B) N-TiO₂ thin films.

The surface morphology is known to be affected by sputtering gas composition. The grain size of the underlying N-TiO₂ thin film decreased, in comparison to the titania thin film with incorporation of nitrogen and increase of reactive gas within the sputtering gases as previously reported¹²². The film thickness was determined by white light profilometry. The TiO₂ film was 450nm ± 5nm whilst the N-TiO₂ film average thickness was 425nm ± 5nm. The surface roughness was 8nm for the TiO₂ whilst it was 15.9nm for the N-TiO₂, reaffirming the SEM observation.

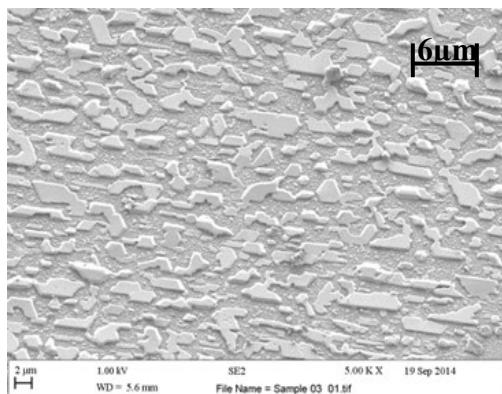
The molybdenum-doped films were less uniform than those produced via nitrogen doping and the undoped titanium dioxide films. All the surface topography images (Figure 36) show evidence of stress, which has caused delaminating and cracking, which is quite extreme in the case of molybdenum coating MoC3 (Figure 36C). However, away from the damaged areas, the coating looks very smooth, without the apparent facets seen on the undoped and nitrogen doped coatings.



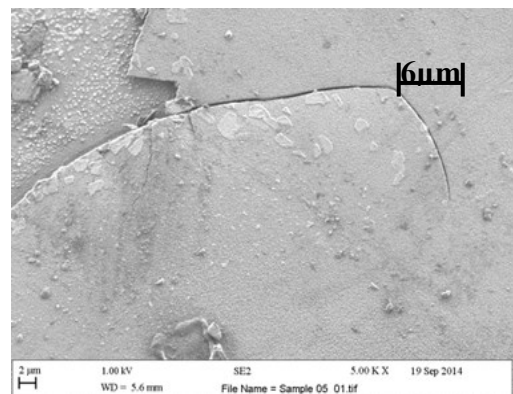
A



B



C



D

Figure 36: SEM images for A) MoC1 B) MoC2 C) MoC3 D) MoC4 molybdenum doped titanium dioxide thin films

Surface topography images of the various erbia doped thin films showed different films structures were produced when erbia was incorporated within the titania films. The undoped TiO₂ film had a smooth coating with irregular surface spherical nanoparticulates (average size of ~50 nm) (Fig. 37A). Interestingly the surface morphology of TiO₂ grown here via the powder sputter rig, presented by the SEM image, looks different to the TiO₂ grown via the Teer Coating rig. This is due to the formation of the thin films; the powder sputter rig provides a closer ion bombardment and therefore the thin films created tend to have areas of thicker film growth and therefore a more rough coverage overall. The film grown with 5% Er-TiO₂ (in the target) showed a grainy surface morphology with a regular even coverage of spherical crystallites (average size of ~50nm) (Fig. 37B).

The 7.5% Er-TiO₂ thin film sample had a rough bumpy surface morphology with a regular of aggregated close packed smooth crystallites (Fig. 37C). The film grown with 10% Er-TiO₂ showed a grainy surface morphology with a regular even coverage of spherical crystallites (average size of ~100nm) (Fig. 37D), however the 12.5% Er-TiO₂ film had a smooth coating with large 'nano-urchin' spherical deposits several microns in diameter.

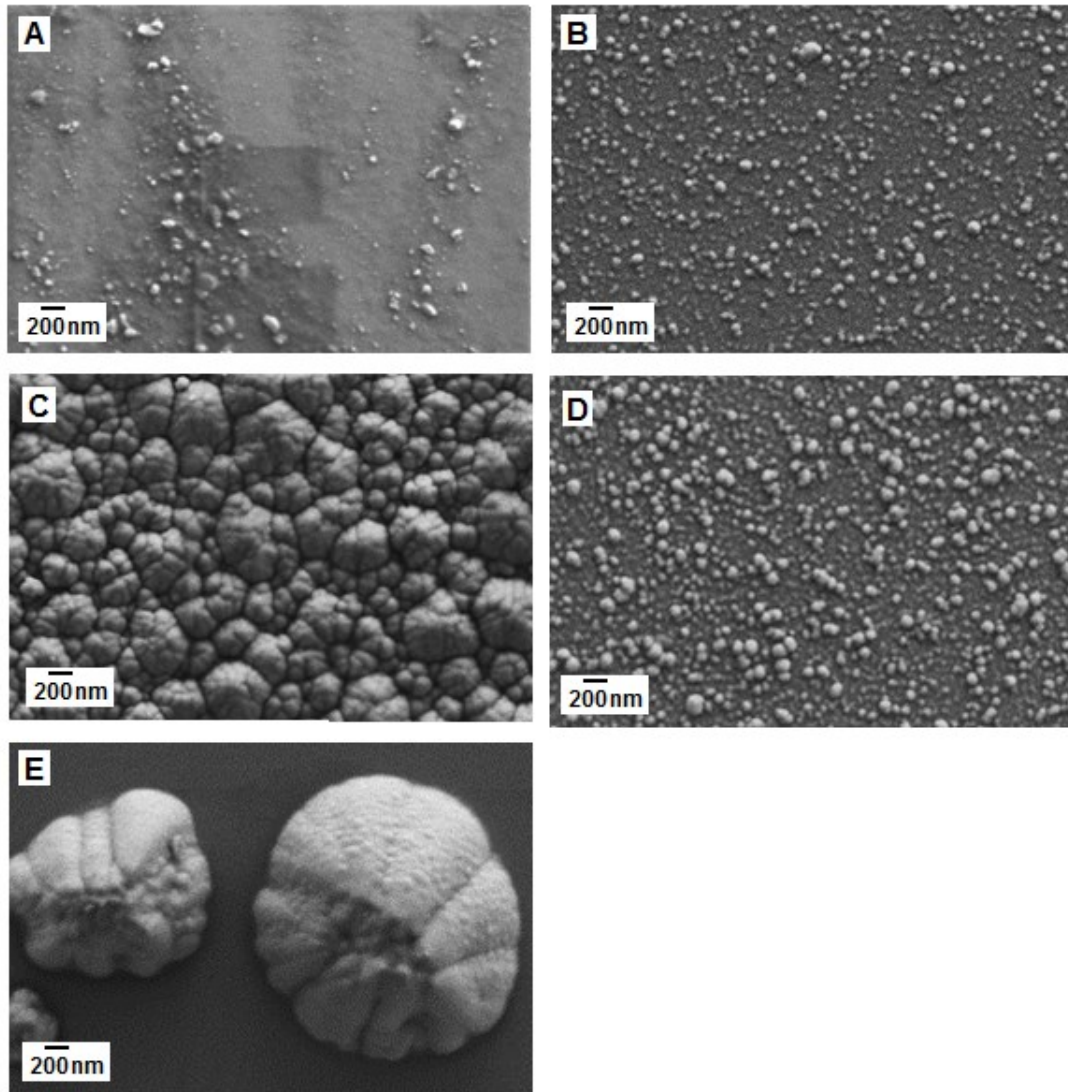


Figure 37: Scanning electron microscopy images of A) TiO_2 , B) 5% Er - TiO_2 thin, C) 7.5% Er- TiO_2 thin D) 10% Er - TiO_2 thin and E) 12.5% Er TiO_2 thin films.

Fig. 38A shows SEM images of the thin films produced on different substrates. A vast difference in film morphology is apparent when a silicon substrate is utilised instead of glass. Fig. 38A and 38C are films grown on glass whilst Fig. 38B and 38D are films grown on silicon. The films grown on silicon substrates have regular

spherical particles evenly covering the surface, whilst the films grown on glass at the same concentrations are much rougher and have an aggregated appearance.

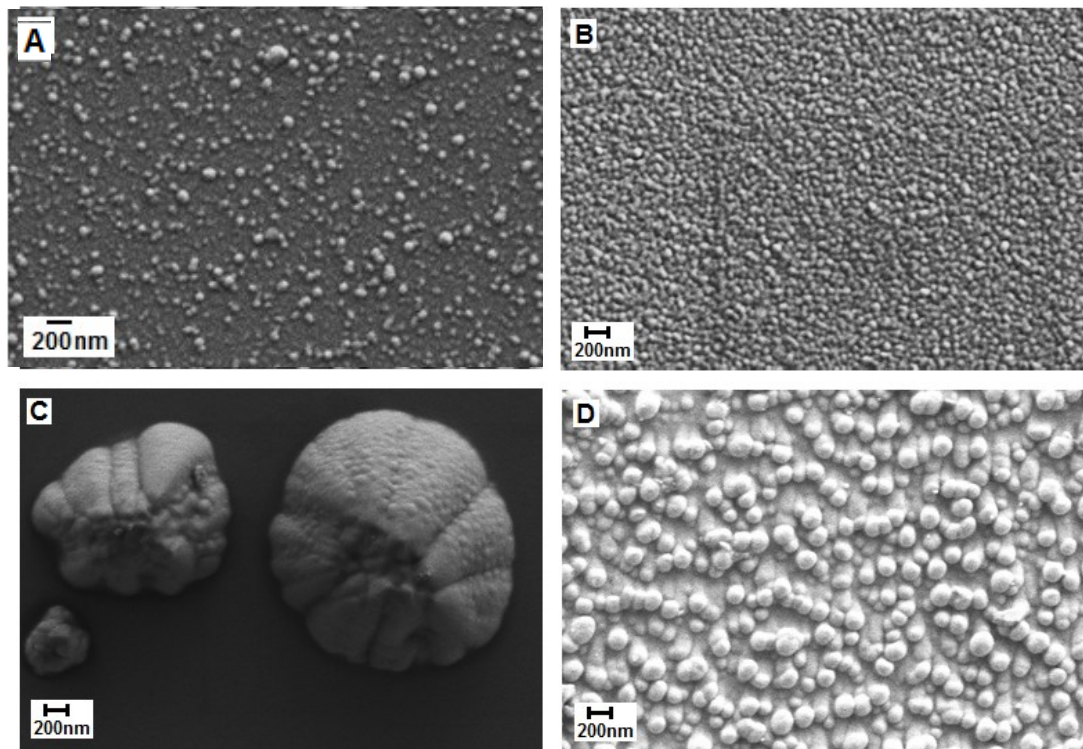
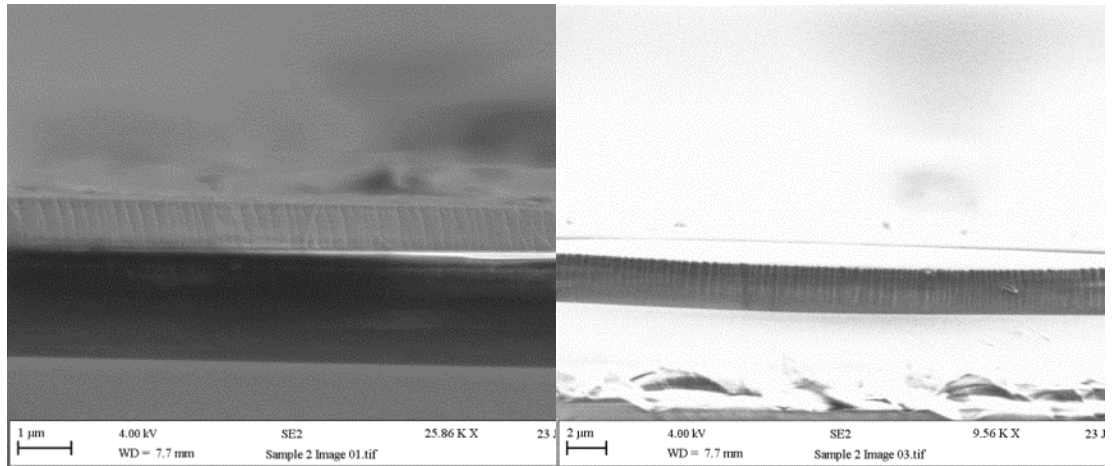


Figure 38: Scanning electron microscopy images of A) 5% Er-TiO₂ on glass, B) 5% Er - TiO₂ on silicon, C) 12.5% Er -TiO₂ on glass and D) 12.5% Er -TiO₂ on silicon.

Cross section images reveal the film thickness, which is in line with the surface profilometry results, showing both techniques adequate at revealing coating thickness results. The SEM section images also reveal that the thin film has a dense columnar grained structure clearly visible (Figure 39).



A

B

Figure 39: Cross section images of undoped TiO₂ (C1)

Fig. 40 shows cross sectional SEM images of the thin films produced on different substrates. The images show that the film thicknesses are around 100nm. Figure 40A and 40C are films grown on glass and confirm that films grown on glass are much rougher in appearance than the films grown on the silicon substrate (Fig. 40B and 40D). Particle size during magnetron sputtering grows over time at a rate that depends on the sputtering yield. Many materials tend to produce particles that are nearly spherical or compact aggregates. There may be nucleation centres occurring from impurities or surface defects within the glass, starting the surface deposition reactions. Whilst some particles may be confined in the plasma and fall onto the substrate when the discharge is extinguished. This seems to be the case for the 12.5% Er-doped thin film shown in Fig 40D, which has round particles that have smeared down the substrate.

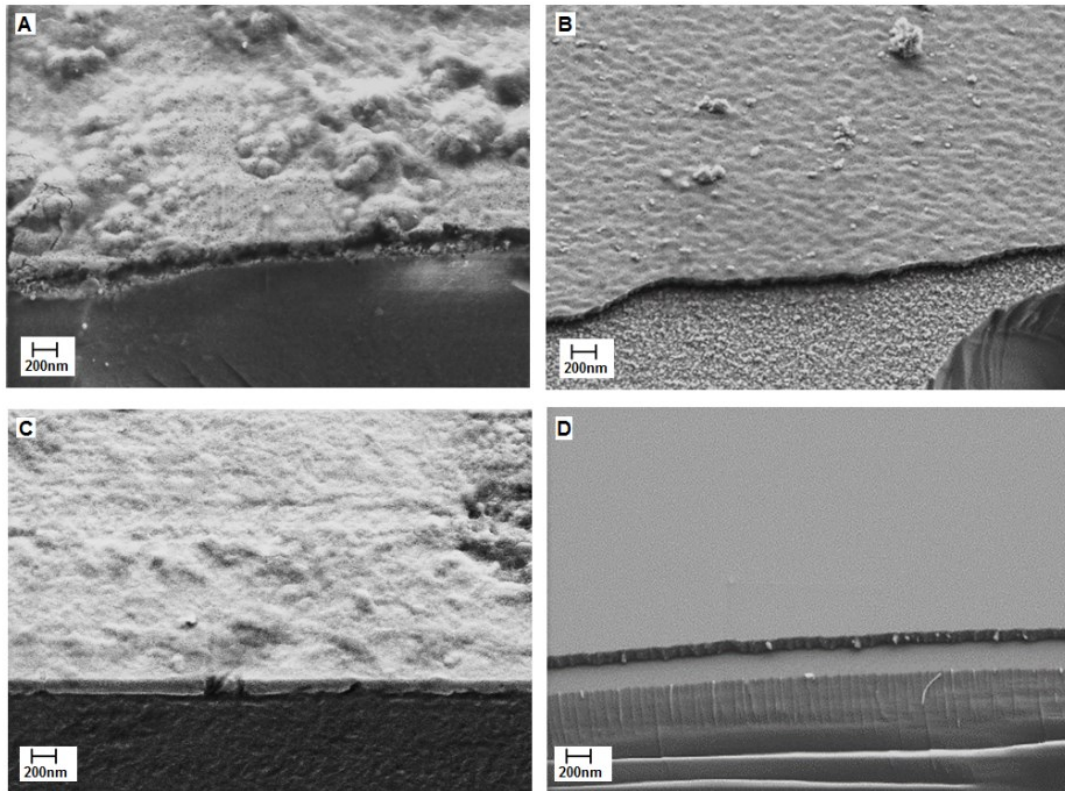


Figure 40: Cross sectional scanning electron microscopy images of A) 7.5% Er-TiO₂ on glass, B) 7.5% Er -TiO₂ on silicon, C) 12.5% Er -TiO₂ on glass and D) 12.5% Er -TiO₂ on silicon.

8.2 TEM RESULTS

TEM micrographs were obtained to provide a physical image of the thin films. The TEM micrographs acquired provided an estimation of the visual appearance of the atoms within the lattice of titanium dioxide. Only one sample was analysed by TEM; this was due to the opportunity arising at the very start of the project and the only films that were produced at this stage were undoped TiO₂.

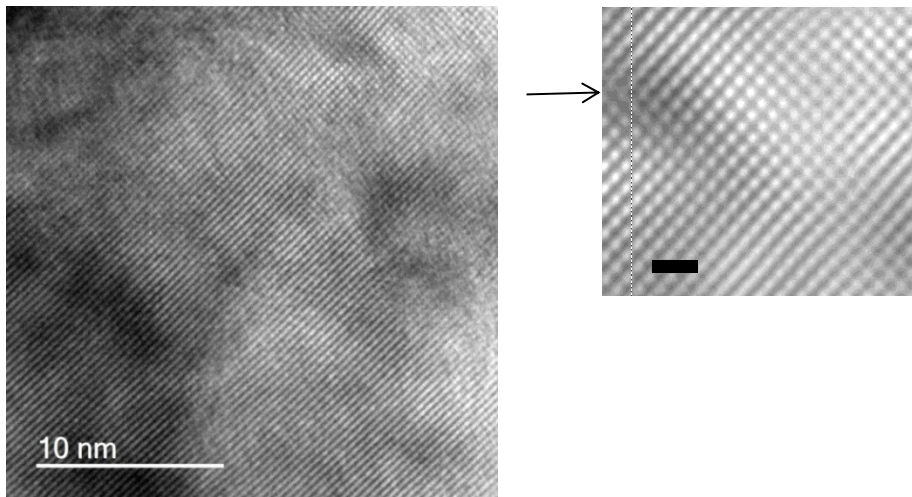


Figure 41: TEM image for TiO₂

Previous TEM phase analysis of TiO₂⁹⁰ highlights similar visual lattice planes. Computational software revealed the lattice planes (Figure 41) of thin film crystalline structure. The distance between each plane is 0.349 nm, which is a characteristic value for (101) this is also in line with literature, confirming that the coatings produced are titanium dioxide.

8.3 SURFACE PROFILOMETRY RESULTS

Surface profilometry results revealed the thin film thicknesses, which is presented in Table 12 and 13, along with the run times. It is important to note that the erbium-doped films were produced via the Powder rig whilst all other films produced via the *Teer* rig. Table 12 contains the results from the *Teer* rig (all substrates glass) and Table 13 contains the results from the Powder rig (substrates varied between glass and silica).

Table 12: Thin film thickness results

Sample ID	Run time (min)	Average Thickness of film produced (nm) taken from 3 readings ± 10nm
TiO₂ C1	60	582.4
C2	90	613.3
C3	90	400.1
C4	90	552.0
N-TiO₂ NC1	90	344.6
NC3	80	460.3
NC4	90	520.8
Mo-TiO₂ MoC1	100	703.4
MoC2	90	629.6
MoC3	95	697.6
MoC4	90	568.1

The thin films produced via the *Teer* rig ranged from 350-700 nm in thickness. The mean thickness for undoped TiO₂ films is 486 nm; the mean for nitrogen doped TiO₂ films: 404 nm; and the mean for molybdenum doped TiO₂ films: 649 nm. Molybdenum doped films were therefore the thickest and nitrogen doped films the thinnest. The greater thickness of the Mo-doped coatings arises because a molybdenum

target was sputtered during their formation, in addition to the two titanium targets. Thus, the amount of coating atoms arriving at the substrate during deposition was greater. The reason for the reduced thickness of the nitrogen coatings is not immediately clear, but may be related to the increased amount of reactive gas introduced during the deposition process, both nitrogen and oxygen being used for these coatings, which tend to form oxide and nitride compounds on the sputtering targets and reduce the amount of titanium being sputtered. In the case of the Powder rig, the distance from the substrate was changed and therefore this contributed to the change in thickness of the films as discussed in section 6.4.

The average thickness of the thin films produced from the powder sputter rig varied from 100-420nm. This shows the variation in the powder sputtering technique, thin films with the same deposition process tend to vary by no more than 100nm in thickness. The mean value was 281.3nm which is considerably smaller than the thickness of the thin films produced from the *Teer* rig.

Table 13: Erbium film run conditions

Powder run	Powder target	Deposition Time in chamber (hrs)	Distance from the substrate (cm)	Substrate	Average Thickness of film produced (nm) taken from 3 readings	
					±10	
1	TiO ₂		3	7	Glass	100
2	TiO ₂		5	7	Glass	385
3	TiO ₂ 5% Er		3	7	Glass	168
4	TiO ₂ 5% Er		4	5	Glass	387
5	TiO ₂ 10% Er		4	5	Glass	341
6	TiO ₂ 10% Er		5	5	Glass	306
7	TiO ₂ 7.5% Er		4	5	Glass	278
8	TiO ₂ 7.5% Er		4	5	Silica	300
9	TiO ₂ 12.5%Er		4	5	Glass	270
10	TiO ₂ 12.5%Er		4	5	Silica	120
11	TiO ₂ 12.5%Er		5	5	Glass	302

12	TiO ₂ 12.5%Er	5	5	Silica	418
----	-----------------------------	---	---	--------	-----

8.4 COMPARISON OF DEPOSITION RATES FOR THE TEER AND POWDER SPUTTERING RIGS

An interesting study into the deposition rates of the rigs will confirm which rig has a greater deposition rate per Kw of power used, and is therefore, more efficient. Firstly the deposition rate ($\text{nm} \cdot \text{min}^{-1}$) for each coating was calculated by dividing the coating thickness (nm) by the deposition time (min). The deposition rate value was then divided by the total target power (W) used in that coating run and a deposition rate per kW of power used was therefore calculated ($\text{nm} \cdot \text{kW}^{-1}$). The average for each different method was then taken and the findings are presented in Table 14. The findings conclude that the *powder sputter* rig is the least efficient at deposition per kW of energy used. The method that was most efficient was the TiO₂ *Teer* coating method, with the Er-TiO₂ method used on the *powder* rig the least efficient.

Table 14: Calculation of deposition rates per kW of power used

Sample ID	Deposition time	Average Thickness of film produced (nm) taken from 3 readings ± 10nm	Deposition rate ($\text{nm}\cdot\text{min}^{-1}$)	Deposition rate per kW ($\text{nm}\cdot\text{kW}^{-1}$)	Mean value
TiO₂ C1	60	582	9.706	9.7	6.77
C2	90	613	6.814	6.8	
C3	90	400	4.44	4.4	
C4	90	552	6.13	6.1	
N-TiO₂ NC1	90	345	3.82	3.8	5.12
Nc2	80		5.75	5.8	
NC3	80	460	5.78	5.8	
NC4	90	521	7.81	7.8	
Mo-TiO₂ MoC1	100	703	7.03	7.0	6.9
MoC2	90	630	6.99	7.0	
MoC3	95	698	7.34	7.3	
MoC4	90	568	6.31	6.3	
Powder Runs TiO₂	180	100	0.55	2.2	4.1

TiO ₂	300	385	1.28	5.1	
Run3	180	168	0.93	3.7	3.6
Run4	240	387	1.61	6.4	
Run5	240	341	1.42	5.7	
Run6	300	306	1.02	4.1	
Run7	240	278	1.58	6.3	
Run8	240	300	0.42	1.7	
Run9	240	270	1.13	4.5	
Run10	240	120	0.5	2.0	
Run11	300	303	1.01	4.0	
Run12	300	418	0.72	2.8	

8.5 WHITE LIGHT SURFACE PROFILOMETRY RESULTS

Figures 42 and 43 show images produced from white light profilometry, which highlight the surface roughness and surface area of the films; results are summarised in Table 15. Highlighted on these images on the left side is the instruments measurements; ‘Sa’ refers to surface area and ‘Sq’ means root mean square roughness. Sa and Sq represent an overall measure of the texture comprising the surface. Sa is used for machined surfaces and Sq used to specify optical surfaces. Therefore the Sq

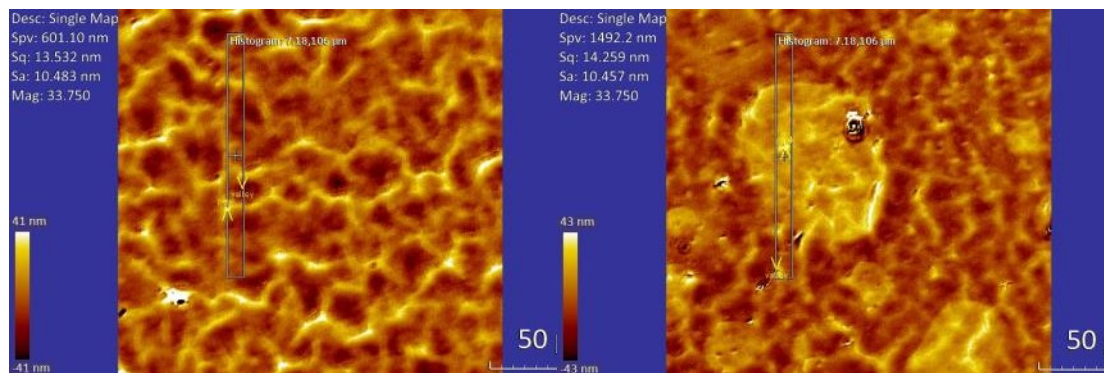
value is of interest in this study. These values can indicate significant deviations in the surface characteristics. 'Sp' refers to the maximum peak height; the height of the highest point. 'Sv' refers to the maximum valley depth; the depth of the lowest point. Spv refers to the maximum height of the surface, these values are evaluated from the absolute highest and lowest points found on the surface; the difference between Sp and Sv.

Results showed that there is a wide variation from sample to sample of the surface roughness of the films, but the deviation from the average of the surface roughness of each individual sample is low (based on 5 scans per sample) showing that the films were uniform across their surfaces.

Table 15: Thin film surface roughness and surface area results

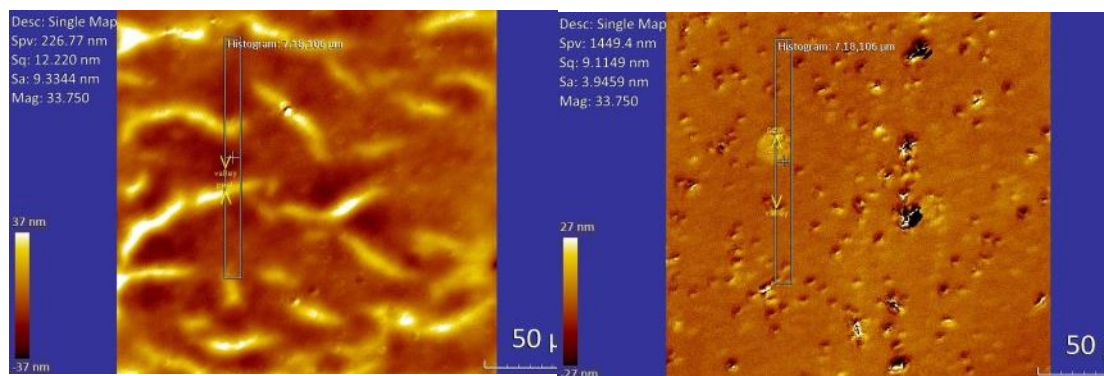
Sample ID	Surface roughness (nm) (Sq value)	Deviation from average (nm)
TiO₂ C1	13.5	5.4
C2	14.2	4.2
C3	12.2	2.1
C4	9.1	1.8
N-TiO₂ NC1	170.7	0.6
NC2	6.4	0.8
NC3	5.3	0.1
NC4	3.6	1.1
Mo-TiO₂ MoC1	161.7	12.6
MoC2	363.3	20.5
MoC3	466.9	40.6
MoC4	435.1	22.1
Er-TiO₂ 5%	9.1	4.6
7.5%	9.5	0.8

10%	7.7	2.4
12.5%	12.0	0.4



A

B



C

D

Figure 42: Surface images for A) C1 B) C2 C) C3 D) C4 undoped titanium dioxide thin films

The white light surface profilometry results for TiO₂ undoped thin films (Figure 42) and the N-TiO₂ thin films (Figure 43) show that similar films, with similar visual appearance, have similar roughness values. With the undoped roughness values

ranging from 9-14nm and the N-doped roughness values ranging from 3-6nm. Figure 43A is clearly an outlier. The explanation for this is that the wrong side of the film was tested and so is down to human error.

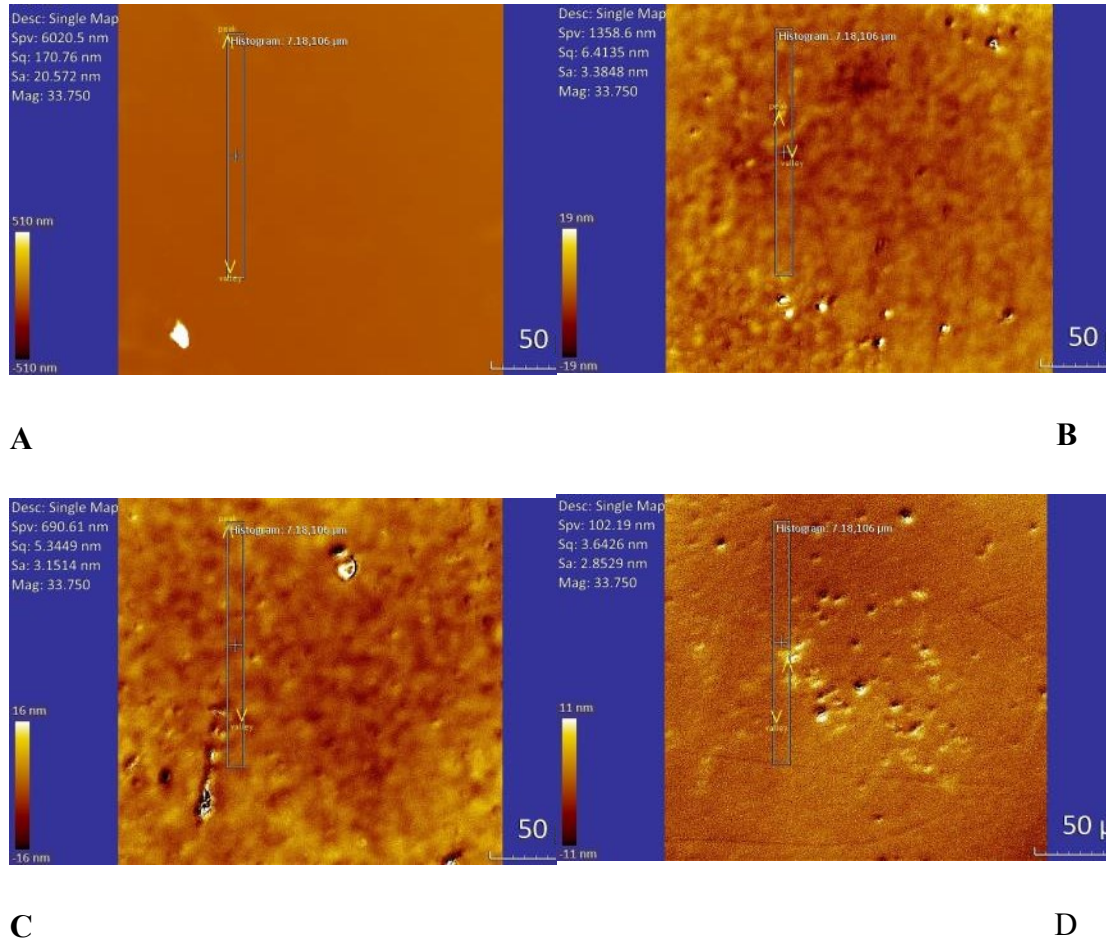
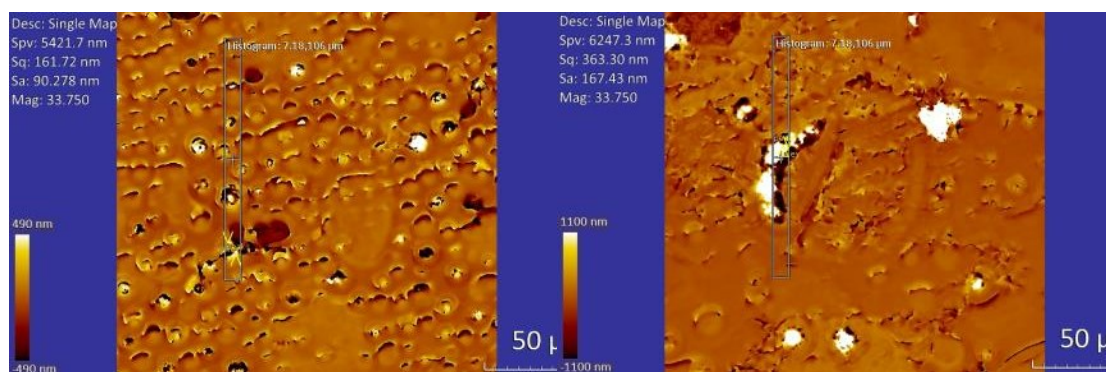


Figure 43: Surface images for A) NC1 B) NC2 C) NC3 D) NC4 nitrogen doped titanium dioxide thin films

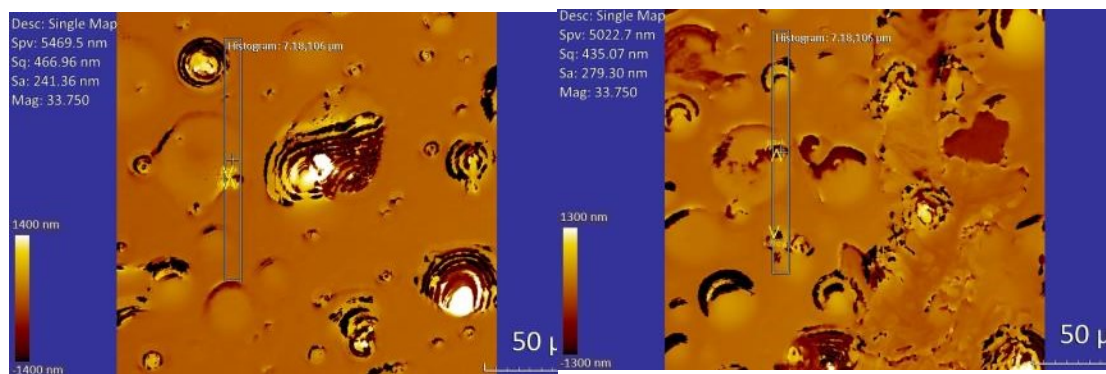
The molybdenum doped titanium dioxide coatings (Figure 44) have Sq values of 161nm, 363nm, 467nm and 435nm. The different sputtering conditions lead to these values. These were by far the greatest Sq values of all the films produced, this can also

be seen in the SEM images along with the images produced from the white light surface profilometer whereby the films are very rough. This information, along with the surface profilometer results is useful as not only were the molybdenum results the thickest films, they also had the greatest surface roughness. The molybdenum films appear to present more defects (grains and holes) on the sample surface than TiO₂ and N-TiO₂ thin films. This caused several problems in the further characterisation of these films, as there appeared to be visible holes in the coatings and the coating had not fully adhered to the substrate. This is further discussed within the characterisation sections.



A

B

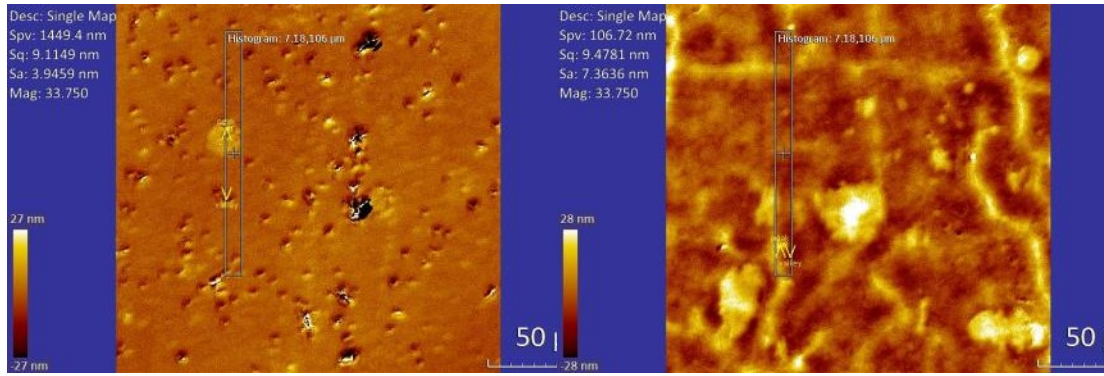


C

D

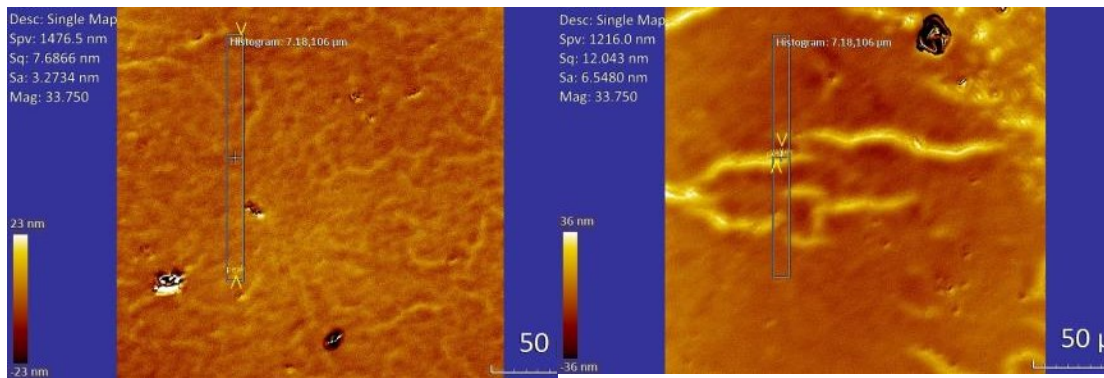
Figure 44: Surface images for A) MoC1 B) MoC2 C) MoC3 D) MoC4 molybdenum doped titanium dioxide thin films

Results from the Erbium-doped thin films show that the surface roughness ranged from 9-12nm and the addition of erbium oxide powder to the target did not have a large effect on the variation in surface roughness. The SEM results show an uneven surface as can also be observed here (Figure 45) where there are clear signs of defects on the surface of the coatings confirming that these particular thin films are not smooth surfaces.



A

B



C

D

Figure 45: Surface images for A) 7.5% Er-TiO₂, B) 5% Er -TiO₂, C) 12.5% Er -TiO₂ and D) 12.5% Er -TiO₂

8.6 XRD RESULTS

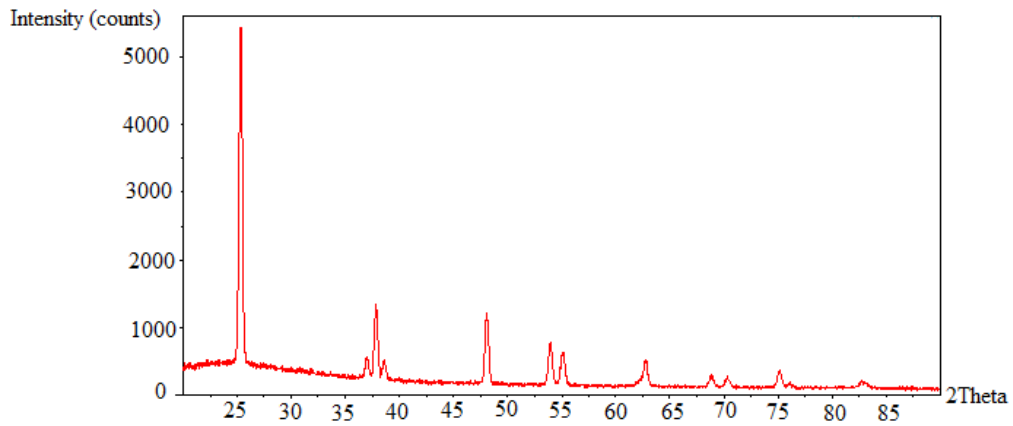


Figure 46: XRD pattern for C1 TiO₂ thin film

Figure 46 presents the XRD trace for coating C1. The observed peaks match those for the standard anatase pattern, with no peaks matching the rutile pattern, confirming that the film produced is that of anatase. The major anatase peaks were found at 25.3°, 37.8°, 48.0°, 55.0° and 62.6°. The XRD results therefore confirm that the post deposition annealed TiO₂ thin film was anatase. Anatase is the phase most desirable for producing the photocatalytic effects of the thin films. XRD revealed that the N-TiO₂ thin films were also anatase in phase, however the peak intensity decreased, suggesting a weaker crystal structure (Figure 47).

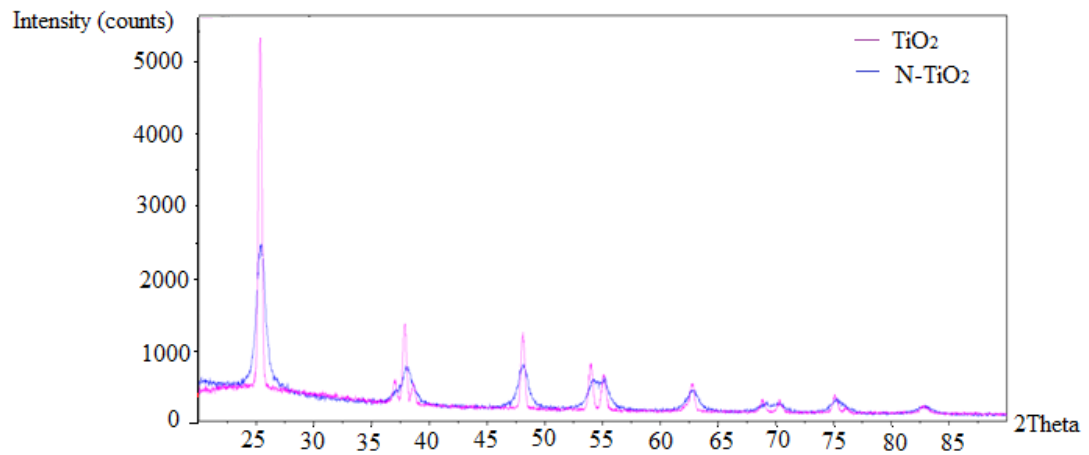


Figure 47: Observed XRD patterns for TiO₂ and N-TiO₂

XRD patterns for the Er-TiO₂ thin films suggest that a mixture of anatase and rutile crystalline phase are present (Figure 48). However the fact that no XRD spectra could be obtained for 3 of these films suggest small amounts of amorphous TiO₂ is also present. Difficulty in obtaining XRD spectra for some thin film samples is suggested to be due to the thickness of the coatings. Raman analysis was also carried out in order

to help confirm the crystalline phases of the thin film.

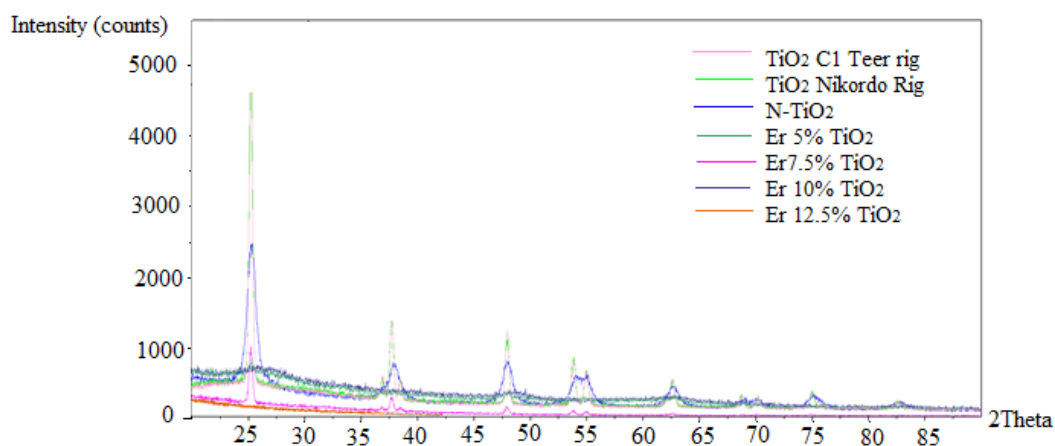


Figure 48: Observed XRD patterns for various thin films

8.7 RAMAN RESULTS

Raman spectra were obtained for titanium dioxide, nitrogen doped titanium dioxide and the various erbia doped titanium dioxide thin films. Raman spectra obtained for molybdenum thin films were not consistent. In some cases the films were shown to be amorphous and others no data was obtained, this was assumed to be due to the difficulty of growing the thin films during the deposition process, as most of the molybdenum thin films were not very well adhered to the substrate. Raman spectroscopy (Figure 49) confirmed that titania and nitrogen doped titania thin films contained standard features of the anatase titania crystal phase in line with literature values¹¹³.

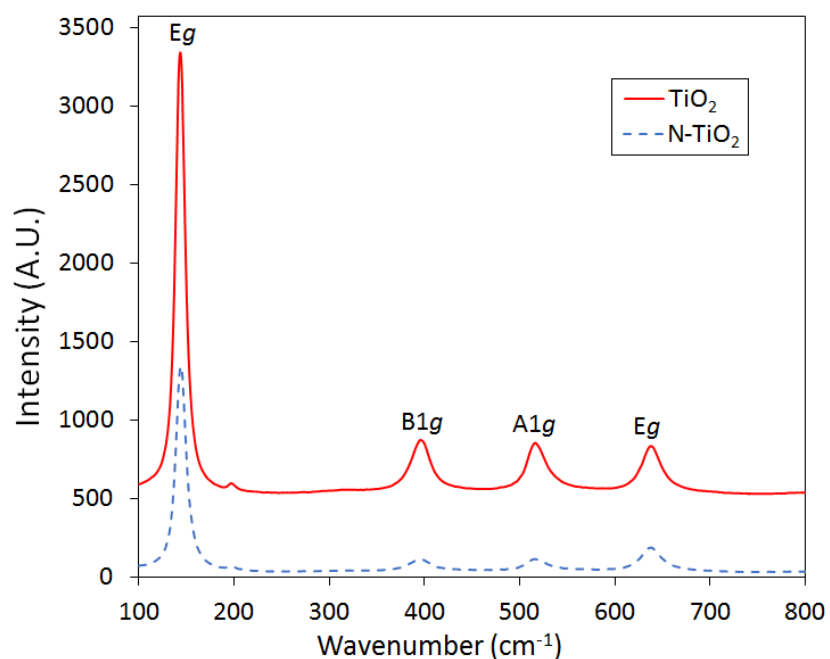


Figure 49: Raman spectra of A) TiO₂ and B) N-TiO₂ thin films.

Peaks at 402 cm⁻¹ related to the O–Ti–O bending vibrations, whilst the Ti–O stretching type vibrations were positioned at 522 and 644 cm⁻¹ ¹²³. No peak position shifts were observed with the incorporation of nitrogen. However, the intensities in the peak positions of the N-TiO₂ were not as sharp, suggesting that the doped film was less crystalline. Raman spectra taken from a previous study ¹¹² shows the positions of titania crystal phases (Figure 50).

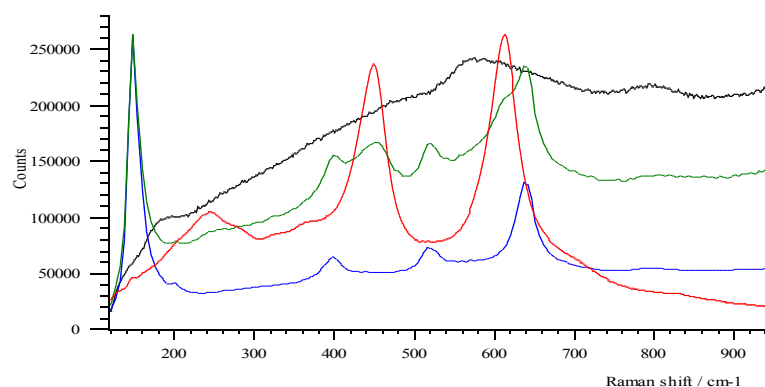


Figure 50: Raman spectra taken from reference ¹¹² to show positions of titania crystal phases , black: Amorphous TiO₂, blue: Anatase TiO₂, green: AN/RU TiO₂ and red: Rutile TiO₂

Raman spectra were obtained for TiO₂ and erbia doped TiO₂ with Er - 5 at %, Er - 7.5 at %, Er - 10 at % and Er - 12.5 at %, as shown in Fig. 51, several overlapping bands appeared around 100 cm⁻¹, ~400 cm⁻¹, ~500 cm⁻¹, ~750 cm⁻¹ and 1100 cm⁻¹. The undoped titania film showed weak broad peaks centered at 435 cm⁻¹, 578 cm⁻¹ and 1096 cm⁻¹. The closest crystalline phase correspond to rutile titania which has characteristic peaks at 450 cm⁻¹ and 615 cm⁻¹ ¹¹². The Er doped TiO₂ had similar peak shapes with varying intensity, several broad bands appeared. A shoulder band at 100 cm⁻¹. A band with medium intensity at ~435 cm⁻¹, a stronger peak at ~475 cm⁻¹ and weaker broad band at ~750 cm⁻¹ were ascribed to a mixture of both anatase crystalline phase, (characteristic peak positions 397 cm⁻¹, 520 cm⁻¹ and 640 cm⁻¹) and rutile crystalline phase, (characteristic peak positions 450 cm⁻¹ and 615 cm⁻¹).

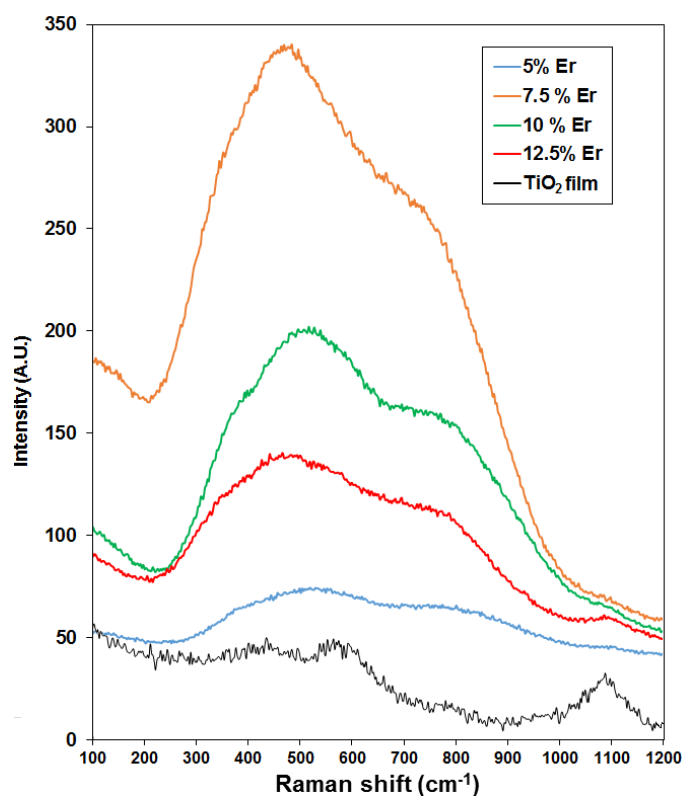


Figure 51: Raman spectra of TiO₂ and Er-TiO₂ thin films on glass substrates.

Figure 52A shows the Raman spectra of erbia doped TiO₂ thin films on different substrates (glass or silica). Sharp high intensity peaks at 304 cm⁻¹, 528 cm⁻¹ and 966 cm⁻¹ are the peaks arising from the silicon crystal substrate. The spectra of the Er-TiO₂ on silicon (Fig. 52B) reaffirm that a mixture of anatase and rutile crystalline phase are present, with peaks centred at 142 cm⁻¹, 398 cm⁻¹, 449 cm⁻¹, 642 cm⁻¹ and 672 cm⁻¹. However, weak peaks around 800 cm⁻¹ suggest small amounts of amorphous TiO₂ is also present.

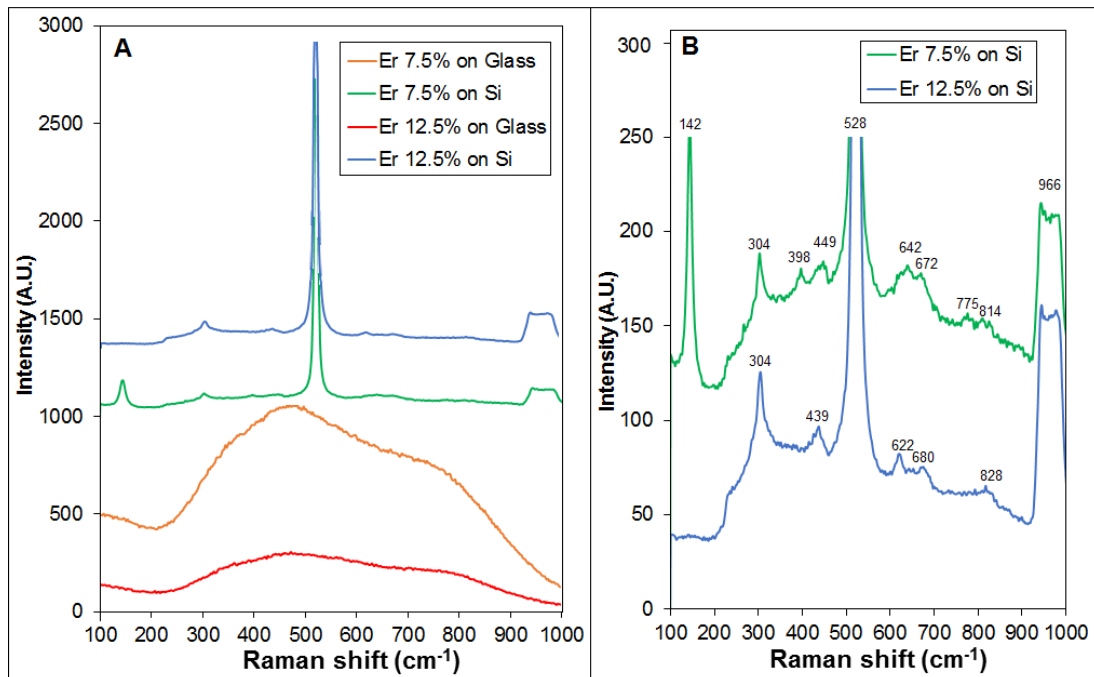


Figure 52: Raman spectra of of A) Er-TiO₂ on different substrates and B) Er -TiO₂ thin films on silicon.

8.8 EDX RESULTS

Unfortunately due to the detection limits of the EDX instrument, other methods of quantifying the elements in the thin films had to be sought. ICP was used in a method where the film was dissolved and the amount of dopant was quantified and therefore chemical composition of the thin films could be understood.

8.9 ICP RESULTS

ICP determined the chemical composition of the coatings using a method not commonly used for identifying the chemical composition of magnetron sputtered thin films. (The chemical composition would usually be determined via EDX; however, in

this case the coatings were too thin for EDX analysis) The calibration plots reveal excellent linearity for titanium, molybdenum and erbium.

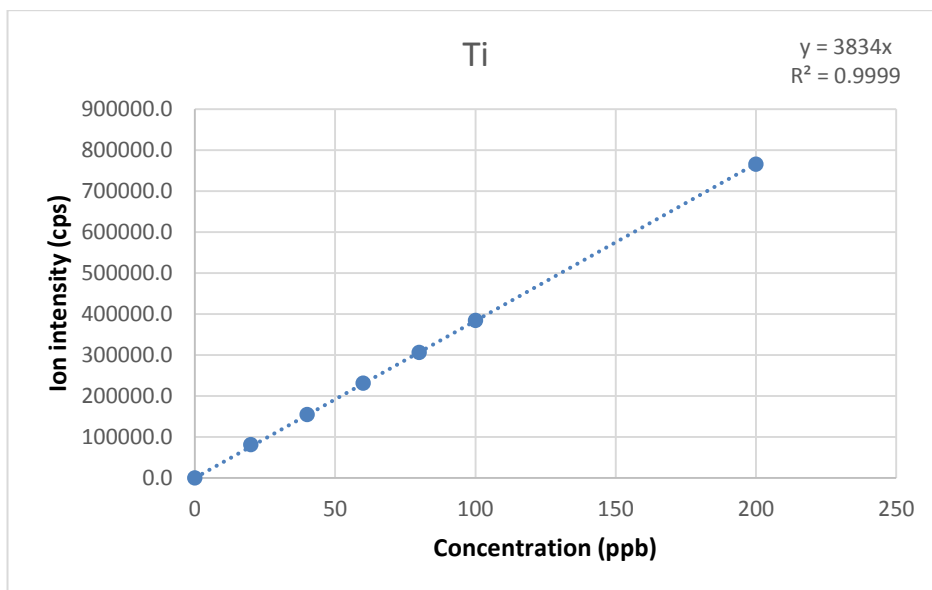


Figure 53: Titanium ICP calibration plot

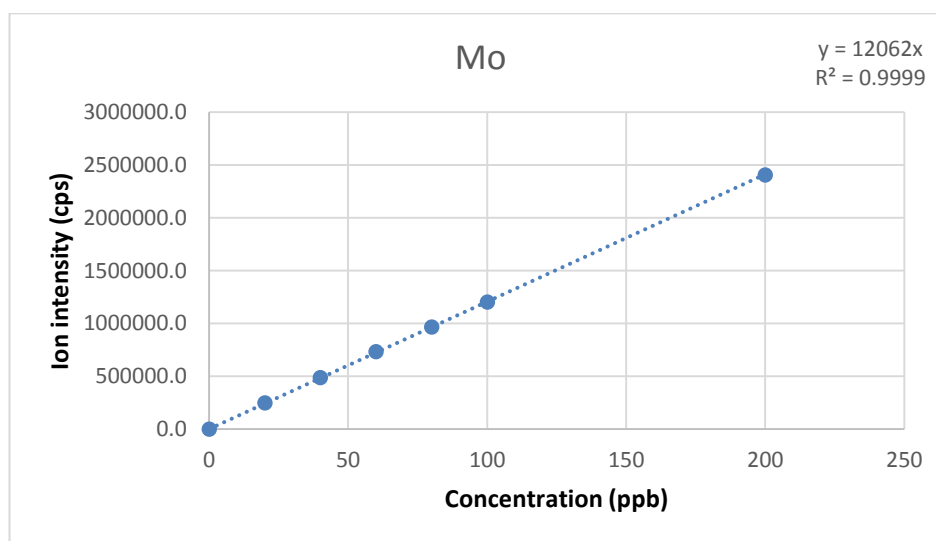


Figure 54: Molybdenum ICP calibration plot

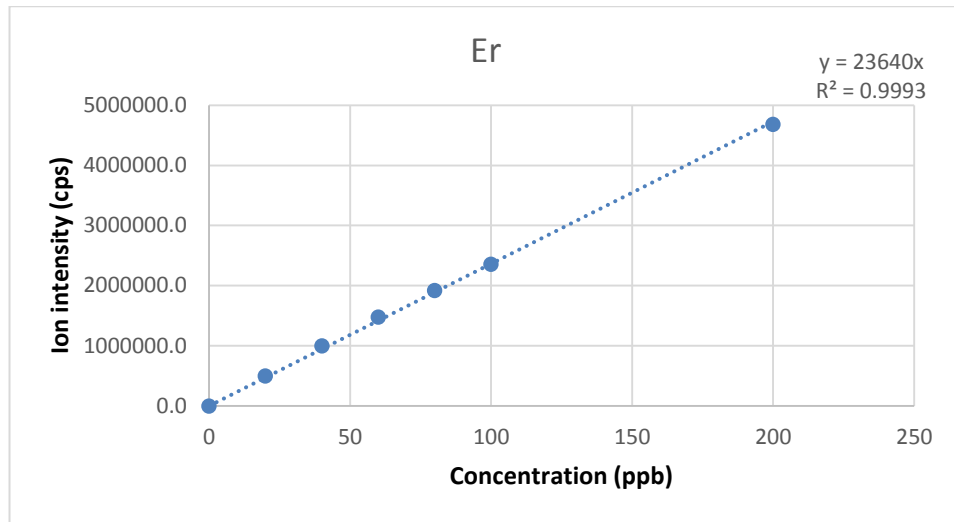


Figure 55: Erbium ICP Calibration plot

From the molybdenum deposition conditions the films were expected to be 10% Mo. From the dissolved coatings the results indicated that Mo1 has a very high molybdenum content at 14.27 and the lowest molybdenum content of Mo2 being 7.83% (Table 16). The same deposition conditions were applied when producing these films and so the conclusion to be drawn here is that the technique offers variation in the composition of the film.

Table 16: ICP results for amount of Mo in final film

Sample ID	Mo Film Composition from ICP
Mo1	14.27%
Mo2	7.83%
Mo3	10.55%
Mo4	11.08%

Table 17 summarises the amount of erbia doping in the digested thin films after ICP-MS analysis. It can be seen that the incorporation of dopant within the films is much lower than the amount prepared in the sputtering target.

Table 17: ICP results for amount of Er in final film compared to starting target

Er at% Target Composition	Er Film Composition from ICP
5%	2.79%
7.5%	3.21%
10%	7.18%
12.5%	7.45%

XPS analysis was conducted and results were obtained for TiO₂, N-TiO₂ and Er-TiO₂ thin films. Direct comparison between TiO₂ and N-TiO₂ results reveal typical Ti 2p_{3/2} and Ti 2p_{1/2} sub peaks due to the spin orbital coupling effect for TiO₂ and N-doped TiO₂ thin films (Fig. 56A).

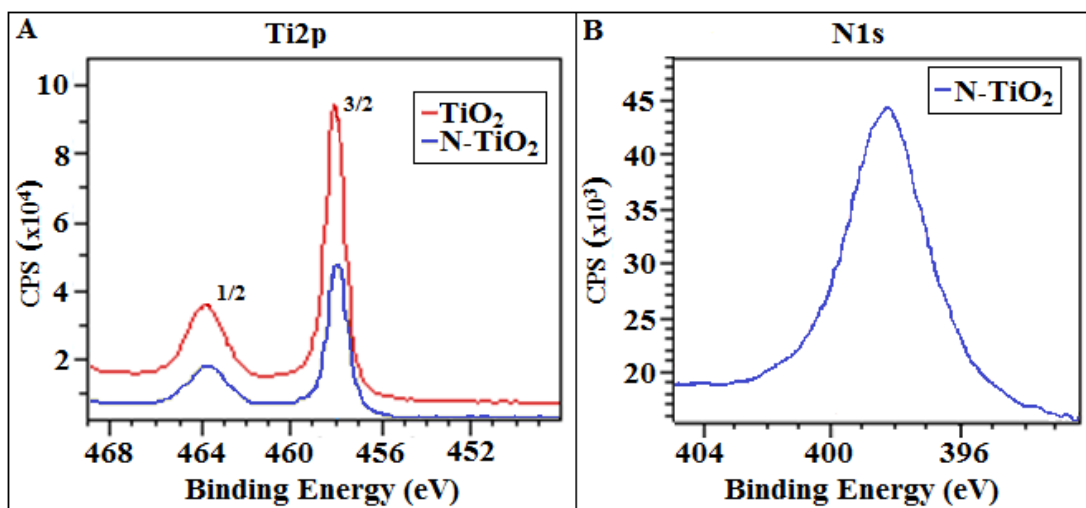


Figure 56: XPS spectra of (A) Ti2p peaks and (B) N1s of TiO₂ and N-TiO₂ thin films.

The TiO₂ peaks were positioned at 458.1 and 464.1 eV. There was a small shift (0.25eV) to lower binding energy ascribed to the incorporation of nitrogen atoms into the titania lattice, which is in agreement with previous observations of nitrogen doped titania¹²⁴. A lowering of the binding energy is resultant of the nitrogen replacing oxygen ions in the TiO₂ matrix. The minimal shift indicates that the nitrogen incorporation does not change the coordination and chemical state of Ti⁴⁺ ions. The N 1s XPS analysis revealed a peak centred at 398 eV and confirmed definitively that

nitrogen was substituted within the TiO₂ structure (Fig. 56B)¹²⁵. The N/Ti atomic ratios were estimated from the relative sensitivity factor and the peak areas of the Ti 2p (455-468 eV) and N 1s (395-400 eV) orbitals in the XPS spectra for the N-TiO₂ thin film and was determined to be 0.040 which equated to be a 1.0%, nitrogen substitution into the TiO₂ lattice.

In addition to XPS in order to determine the nitrogen content of the thin films, they were analysed using an automated combustion method (Leco CHN-600 Elemental Analyser). Thin films were ground to a fine powder using a ball mill. Powdered samples (0.5g) were combusted by heating it to a high temperature by a resistance furnace in a stream of purified oxygen. The N₂ produced by combustion is measured by a thermal conductivity cell. From this method the percentage of nitrogen was determined as 0.9 % ± 0.05.

The results from XPS analysis show a N content slightly higher than the result from the automated combustion method, XPS is a very reliable technique and the reason for the lower value of N from the carbon analyser is suspected to be due to the concentration being lower than the detection limit of the carbon analyser instrument.

Direct comparison of TiO₂ films and Er-TiO₂ films through XPS reveal that the Ti 2p XPS spectrum can be resolved into two components at binding energies of 464.0 eV and 458.4 eV, which can be assigned to Ti⁴⁺ and Ti³⁺, respectively. The Er4d XPS peak position located at BE of 168.7–169.2 eV indicate that Er states are to be

attributed to Er_2O_3 . The XPS measurement of binding state of Ti and Er in Er-doped TiO_2 films is shown in Figure 57.

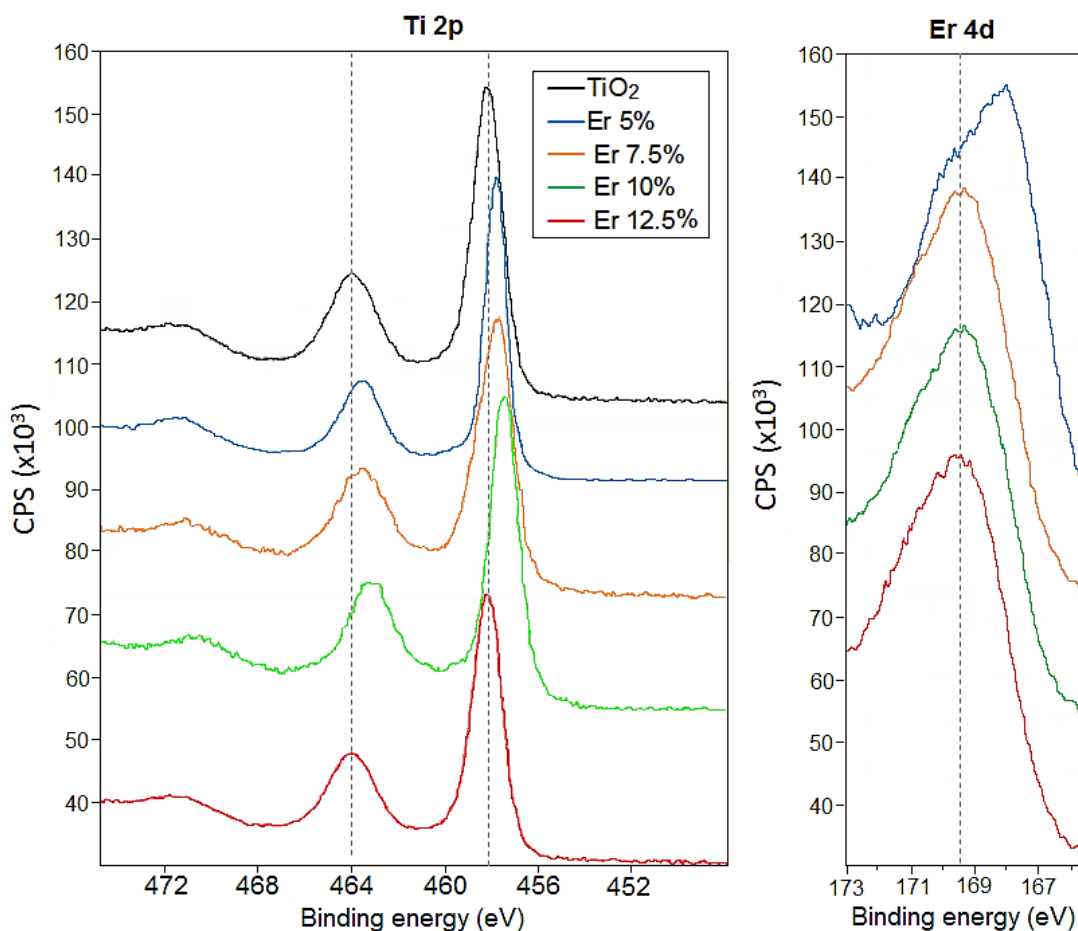


Figure 57: XPS spectra of (A) Ti2p peaks and (B) Er 4d peaks of TiO_2 and Er- TiO_2 thin films.

8.11 BAND GAP CALCULATION

The Tauc plot method determines the band gap from the UV-vis absorption spectra. An example of spectra obtained is seen in Figure 58. From the band gap

calculation it is important to see if the dopants cause a shift to the visible range (red shift) or a shift towards the UV range (blue shift).

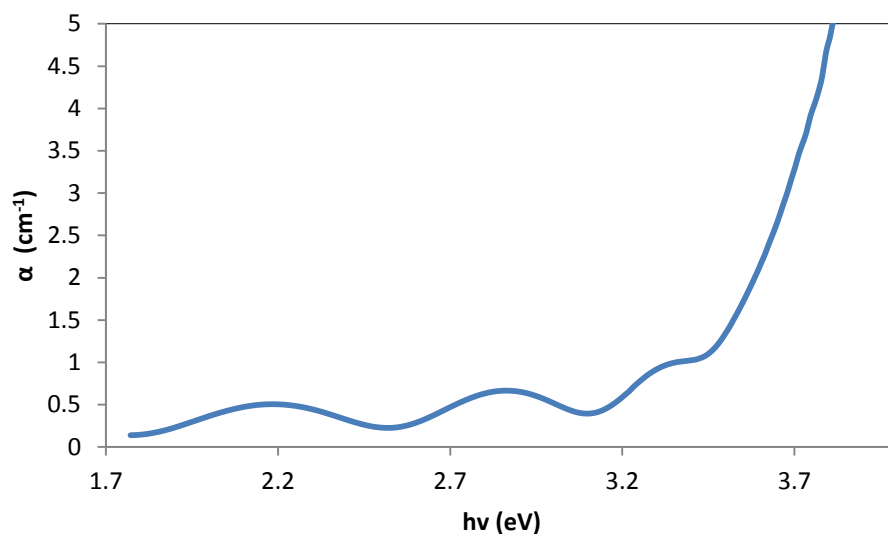


Figure 58: UV-Vis absorption spectra for TiO₂ C1

To investigate the band gap alteration of TiO₂ thin films and the effect with nitrogen incorporation, UV–visible absorption spectra were measured (Fig 59A). The absorption spectrum shows that there is a strong absorption peak centred at 330nm as expected for TiO₂.

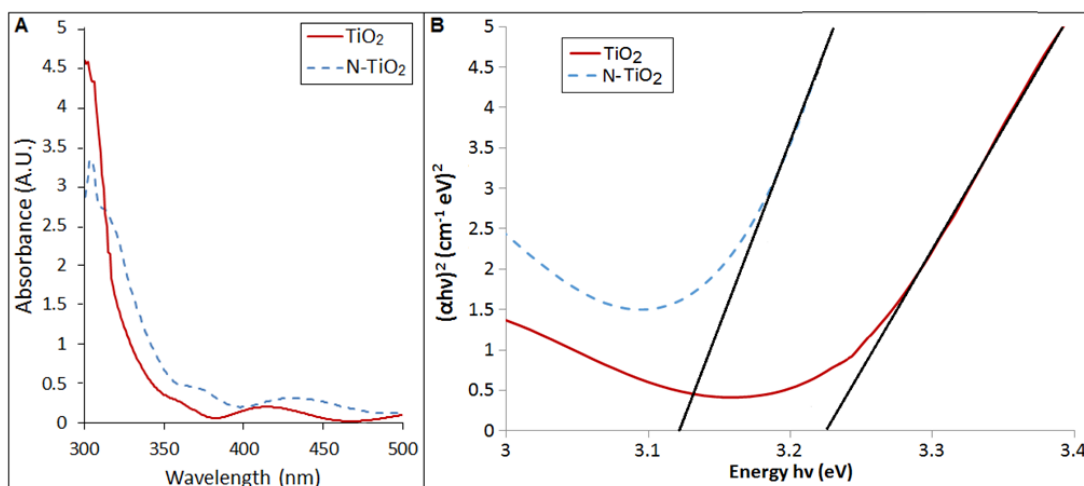


Figure 59: A) UV-visible absorption spectra and B) Tauc plot of TiO₂ and N-TiO₂ thin films.

There is a shift of the absorption peak toward the visible for the N-doped TiO₂ film. Additional peaks were also observed relating to Fabry-Perot interference arising from refractive index contrast between the substrate and film¹²⁶. The optical band gaps of TiO₂ and N-TiO₂ were determined using a Tauc plot of the modified Kubelka-Munk (KM) function with a linear extrapolation (Fig 59B)¹²⁷. The band gaps of TiO₂ and N-TiO₂ were calculated to be 3.20 and 3.14 eV, respectively. The N-atoms can occupy both interstitial or substitutional positions in the lattice structure. Substitution N-doped anatase has been shown to have a band gap of 3.06 eV, whilst interstitial N-doped anatase band gap is reduced 2.46 eV, therefore the N-TiO₂ is most likely to be substitutional.

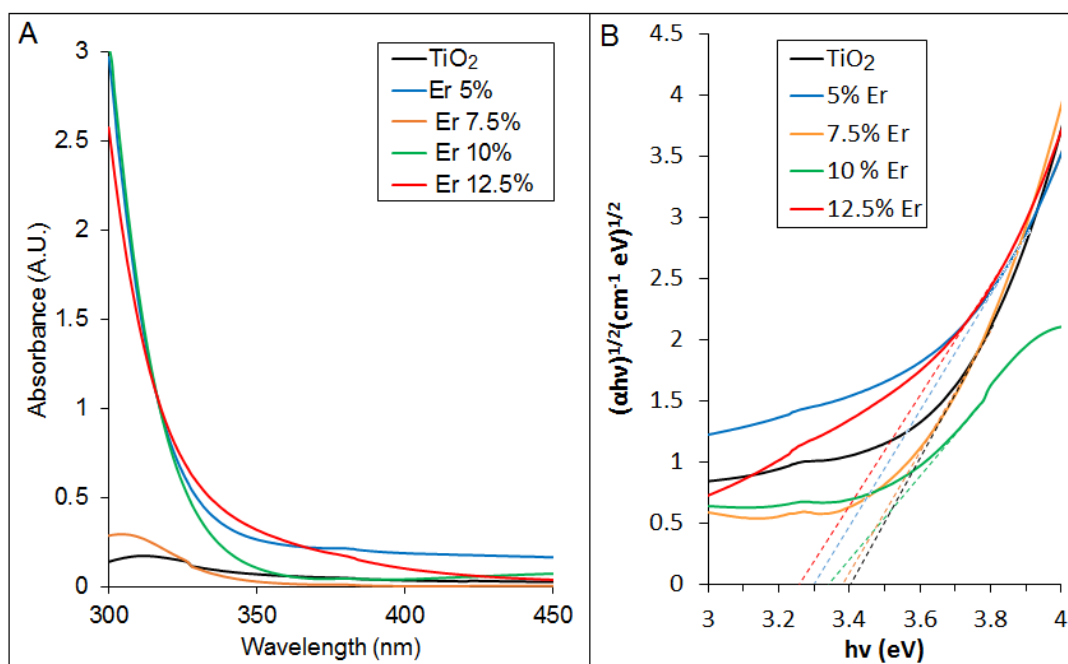


Figure 60: A) UV-visible absorption spectra and B) Tauc plot of TiO₂ and Er-TiO₂ thin films.

To study the optical absorption properties of Er doped TiO₂ UV-visible absorption spectra were recorded (Fig 60A). All films had a broad intense absorption around 300 nm, which is the characteristic absorption corresponding to the excitation of electrons from the valence band to the conduction band in TiO₂. All Er -doped films showed a slight shift of their absorption edge into the visible light compared to undoped TiO₂. The red shift in the band gap transition, existed due to the charge transfer transition between TiO₂ and Er³⁺ intra-4f electrons. However, no further absorption peaks can be observed as shown in the literature¹⁴. It has been shown that Er doping results in absorption peaks located at 451, 475, 524 and 655 nm, which can be attributed to the transition from the 4I_{15/2} ground state to the excited states of the

erbium ions $4F_{3/2,5/2}$, $4F_{7/2}$, $2H_{1/2}$ and $4F_{9/2}$. The transitions of 4f electrons of Er^{3+} favour the separation of photogenerated electron–hole pairs. That is helpful for the improvement of photocatalytic activity under visible light. To investigate the band gap alteration of erbia doping, of the optical band gaps were determined using a Tauc plot of the modified Kubelka–Munk (KM) function with a linear extrapolation¹²⁷ (Fig 60B). The band gap varied between 3.4eV and 3.28eV. Band gaps for all films are presented in Table 18.

Table 18: Band gap values

Sample ID	Band gap value eV	Shift in band gap
TiO₂	3.2	0
N-TiO₂	3.14	0.06
Er-TiO₂ 5%	3.30	0.10
Er-TiO₂ 7.5%	3.38	0.18
Er-TiO₂ 10%	3.35	0.15
Er-TiO₂ 12.5%	3.28	0.08

8.12 CONCLUSION

Titanium dioxide thin films were successfully deposited on glass substrates using a planar magnetron sputtering method. Nitrogen doping was achieved by the introduction of nitrogen gas as an additional reactive gas during sputtering. Molybdenum doped thin films were also produced from a similar method however characterisation of these films proved difficult and further modification of the method

is needed in order for these thin films to be used in this type of study. The range of analytical results provided in this chapter show that TiO_2 , N-TiO_2 and Er-TiO_2 thin films were successfully produced and characterised. The variation in the techniques to produce the different films has led to variation in the results such as different surface topographical features showed in the SEM results. The successful characterisation of these films leads to the conclusion that anatase form titanium dioxide has been produced. The presence of the anatase phase was confirmed by XRD for all annealed TiO_2 and N-TiO_2 thin films. There was a distinctive shift of the absorption band in the N-TiO_2 to longer visible regions of the electromagnetic spectrum. In the case of the powder target sputtered thin films, erbium doped titanium dioxide was successfully produced in different quantities. The characterisation of the different amount of dopant within the film was very important to the study. The amount of erbium couldn't be quantified using the EDX standard method for thin films. The amount of erbium present in the TiO_2 thin film was determined using ICP-MS. From the ICP results we can conclude that the amount of dopant in the powder, does not equate to the amount of dopant in the sputtered thin film. XPS analysis revealed that erbium was present in the form of an oxide. These Er-TiO_2 thin films were characterised to be a mixture of anatase and rutile. From the XRD and Raman spectroscopy results it can be concluded that, increasing the amount of lanthanide dopant in the thin film significantly promotes the formation of rutile phase, rather than anatase phase. Raman spectroscopy also revealed that the some films were not crystalline and the broad peak positions obtained corresponded to a mixture of anatase and brookite crystalline forms. The measuring of

the band gap of the materials allows for further study into the photocatalytic properties of the thin films produced. Such work is detailed in Chapter 10.

The main aim of the nanoparticle work was to develop a light emitting nanomaterial to act as the light energy in the degradation of T&O's in drinking water.

Strategies include:

1. Growth of core shell nanoparticles by colloidal synthesis.
2. Testing of luminol as an alternative to electrical light
3. Creation of TiO₂ nanoparticles

9.1 UV-VIS RESULTS

The gold nanoparticle solution produced via the citrate reduction method was characteristically red and the silver nanoparticle solution was characteristically yellow (Figure 61).



Figure 61: Gold and silver nanoparticle solutions produced

The UV-Vis absorption spectra for the gold nanoparticles showed a distinctive plasmon band absorbance measurement at 520nm (Figure 62).

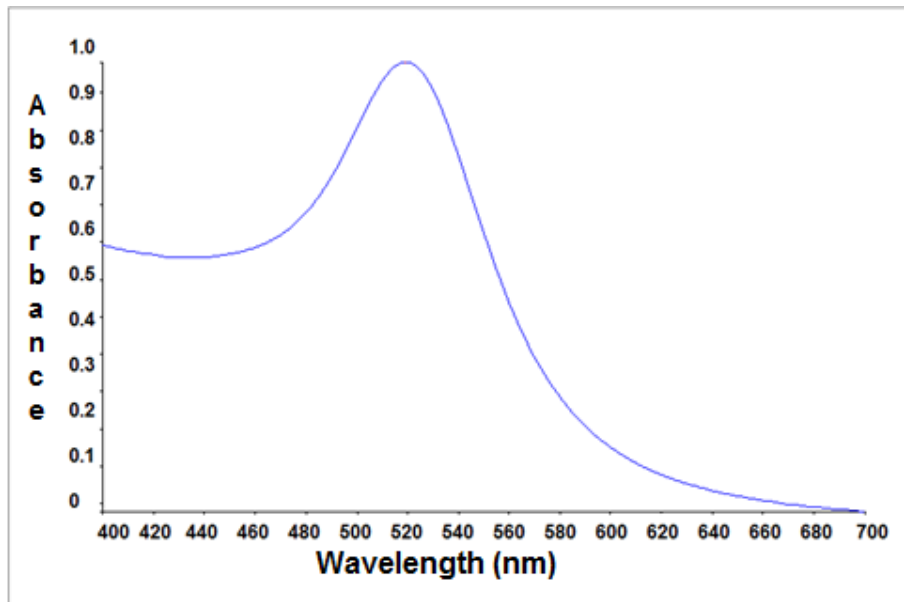


Figure 62: UV-VIS absorption peak for gold nanoparticles

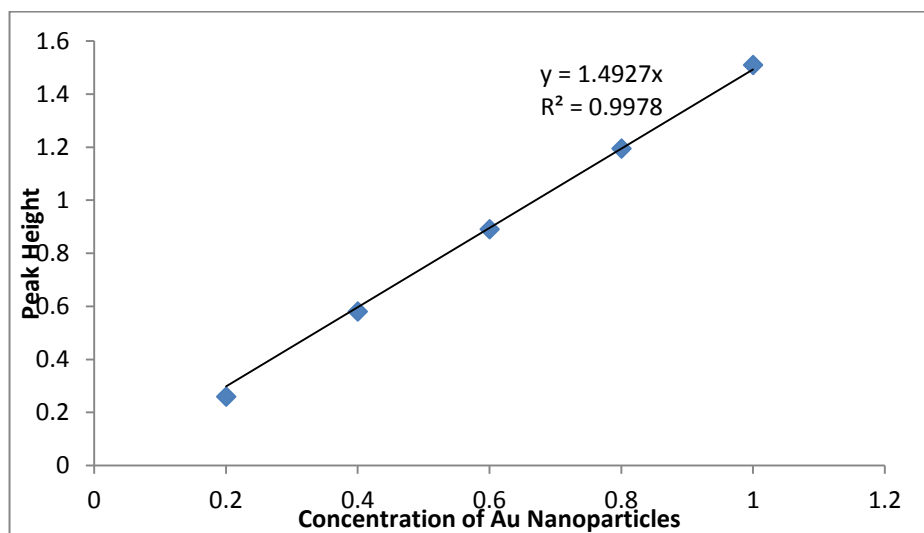


Figure 63: UV-Vis calibration plot for Au

The UV-vis absorption spectra for silver nanoparticles showed a distinctive plasmon absorbance measurement at 430nm (Figure 64).

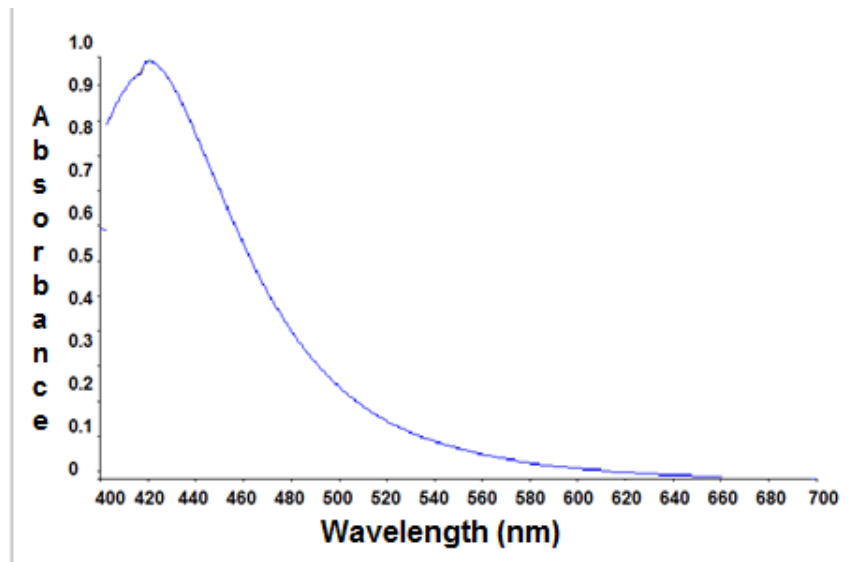


Figure 64: UV-VIS absorption peak for silver nanoparticles

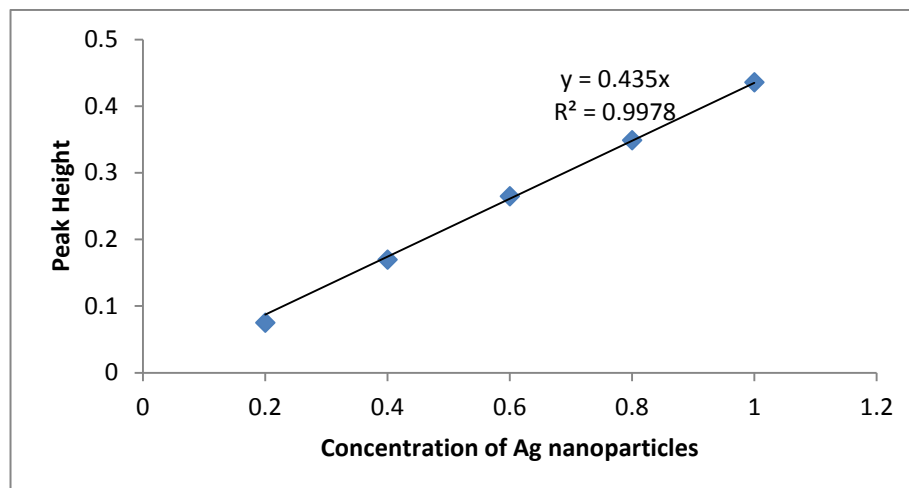


Figure 65: UV-Vis calibration plot for Ag

9.2 PHOTON CORRELATION SPECTROSCOPY RESULTS

The initial nanoparticles produced included gold nanoparticles, gold core nanoparticles coated in silica, silver nanoparticles and silver core nanoparticles coated

in silica. The results in Table 19 show the size of the particles in suspension in nanometres (nm) and the thickness of the silica coatings. An example of the spectra produced from the photon correlation spectrometer is displayed in Figure 66.

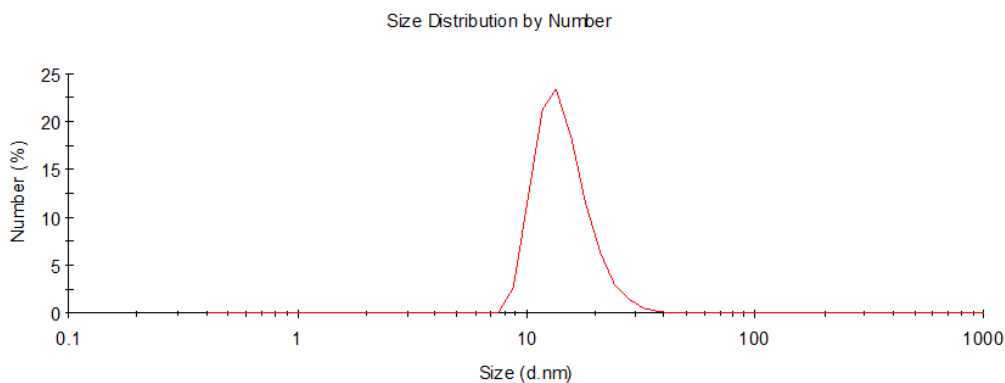


Figure 66: Example spectra of gold nanoparticle particle size

The instrument also provides an additional value called the poly dispersity index (PDI), this is a measurement of how polydisperse the sample is with a value of 1 having an indistinguishable size, which indicates that the sample has a very broad size distribution and may contain large particles. A sample with PDI of 0.07 or below is considered monodisperse. A sample with a PDI higher than 0.7 indicates a very broad distribution of particle sizes. A sample that has a PDI of 0.08 to 0.7 is considered the mid-range of PDI and the range in which the distribution of particles are the best¹¹⁵. The results in Table 19 indicates the PDI values for the nanoparticles synthesised, it can therefore be concluded that they all fall into the range where the distribution of particles is even.

Table 19: Photon correlation spectroscopy results of nanoparticles produced, gold and gold coated in silica and silver and silver coated in silica

Sample name	Average particle size diameter (nm)	Polydispersity index (PDI)
Gold nanoparticles	15.8	0.1
Gold nanoparticles coated with silica	33.2	0.2
Silver nanoparticles	4.6	0.5
Silver nanoparticles coated with silica	6.8	0.5

9.2 CONCENTRATION OF NANOPARTICLES

Concentration of gold nanoparticles were calculated. In a study by R.Johnston¹²⁸ it is assumed for ‘spherical’ metal clusters such as gold nanoparticles that:

$$V_{\text{cluster}} = NV_{\text{atom}} \quad \text{Eq. 7}$$

$$\frac{4}{3}\pi (R_{\text{cluster}})^3 = N\frac{4}{3}\pi (R_{\text{atom}})^3 \quad \text{Eq. 8}$$

Where V is the cluster or atom volume, R is the cluster or atomic radius and N is total number of atoms within the cluster. Re-arranging this gives us:

$$R_{\text{cluster}} = N^{1/3} R_{\text{atom}} \quad \text{Eq. 9}$$

Knowing this cluster radius we can also calculate the surface area (S) of the nanoparticles:

$$S_{cluster} = 4\pi (R_{cluster})^2 \quad \text{Eq. 10}$$

We may also calculate the number of surface atoms, N_s by dividing the surface area of the cluster by the cross section of an individual cluster atom:

$$N_s = (4\pi (R_{cluster})^2 / \pi(R_{atom})^2) = 4N^{2/3} \quad \text{Eq. 11}$$

Nanoparticles found with a radius of 7nm from the photon correlation spectroscopy results and R_{atom} of approx. 0.137nm would therefore lead to the number of gold atoms per nanoparticle to be estimated using:

$$N = (R_{cluster}/R_{atom})^3 \quad \text{Eq. 12}$$

$$= (7 \times 10^{-9} / 0.137 \times 10^{-9})^3$$

$$= \underline{133392} \text{ gold atoms per nanoparticle}$$

Therefore The number of surface atoms N_s , on a single gold nanoparticle can be estimated to be:

$$N_s = 4N^{2/3} \quad \text{Eq.13}$$

$$= 4 \times (133392)^{2/3}$$

$$= \underline{10442} \text{ gold surface atoms per nanoparticle}$$

From the calculation of N the molecular weight (Mw) of a single nanoparticle was calculated using the relative molecular mass of a single gold atom (Mgold)

$$Mw = M_{\text{gold}} \times N \quad \text{Eq. 14}$$

$$= 196.97 \times 133392$$

$$= \underline{26274} \text{ kDA mol}^{-1}$$

Calculation of the amount of nanoparticles formed (Nnp) when 1 dm³ of 1mM HAuCl₄ is reduced by citrate was calculated:

$$\text{Moles of HAuCl}_4 = 1 \times 10^{-3}$$

$$\text{No of gold atoms} = 1 \times 10^{-3} \times N_A$$

$$= 6.022 \times 10^{20}$$

$$N_{\text{np}} = N_{\text{atom}} / N \quad \text{Eq. 15}$$

$$N_{\text{np}} = 6.022 \times 10^{20} / 133392$$

$$= \underline{4.5145 \times 10^{15}} \text{ nanoparticles formed per } 1 \times 10^{-3} \text{ mol HAuCl}_4$$

Hence final concentration of gold colloid Cnp was estimate by dividing Nnp by Avogadro's number, Na

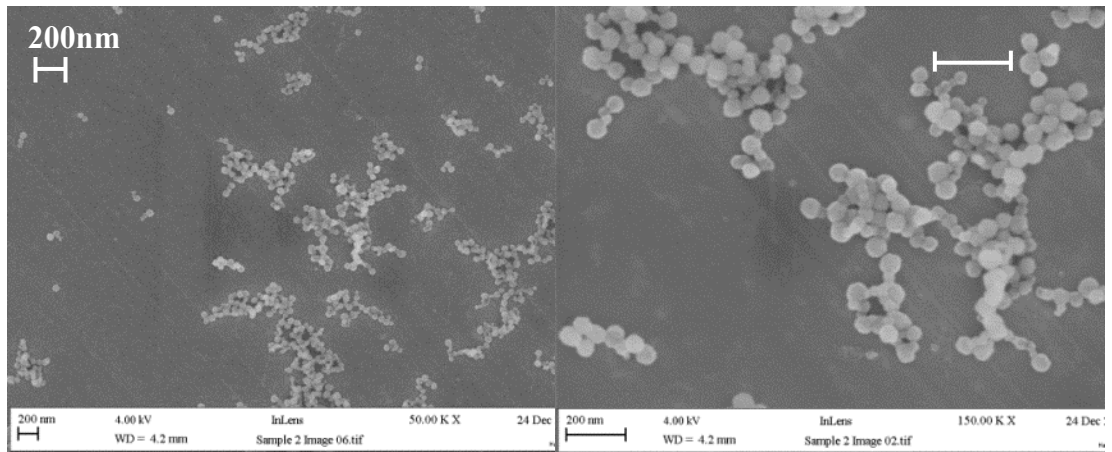
$$C_{np} = N_{np}/N_a \quad \text{Eq. 16}$$

$$= 4.5145 \times 10^{15} / 6.022 \times 10^{23}$$

$$= \underline{7.496 \times 10^{-9} \text{ mol dm}^{-3}}$$

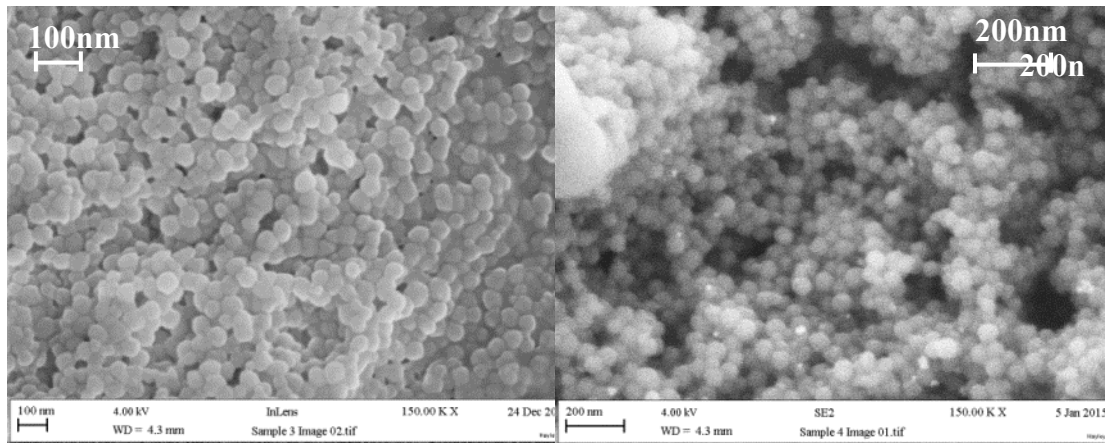
9.3 LUMINOL DOPED SILICA NANOPARTICLES AND COATING OF LUMINOL DOPED SILICA WITH GOLD NANOPARTICLES

The SEM results shown in Figure 67A represent luminol doped silica. These are magnified further in Figure 67B and it is clear that a cluster of nanoparticles has been produced with a diameter of 50 nm. The image of the nanoparticles observed in Figure 67C was taken after the luminol silica nanoparticles were functionalised with APS. APS provides a surface coupling agent as the gold nanoparticles have an affinity for amines. The APS added has caused the nanoparticles to cluster together, the diameter remains the same at 50 nm. Figure 67D shows the addition of gold nanoparticles, these can be observed as the bright white dots tethered to the surface of the luminol doped silica.



A

B



C

D

Figure 67: SEM results for a), b) luminol doped silica c) luminol doped silica with APS and d) luminol doped silica with gold nanoparticles

9.4 FLUORESCENT SPECTROSCOPY RESULTS FOR LUMINOL DOPED SILICA NANOPARTICLES

Fluorescent spectroscopy results confirm that silica has successfully been doped with luminol as a fluorescent signal corresponds to the peak height. The peak height and therefore the fluorescence decreases when gold nanoparticles are added to

the solution. The fluorescence results in Table 20 show that with the addition of gold colloids the wavelength of the suspension is 427.5 nm. Previous studies have shown this to be approx. 425 nm⁹⁴.

Table 20: Fluorescence spectroscopy results for luminol doped silica

Sample	Wavelength peak (nm)	Peak height	Peak area
Luminol doped silica	416	216.5	15487.175
Luminol doped silica with the addition of gold nanoparticles	427.5	140.7	9121.514

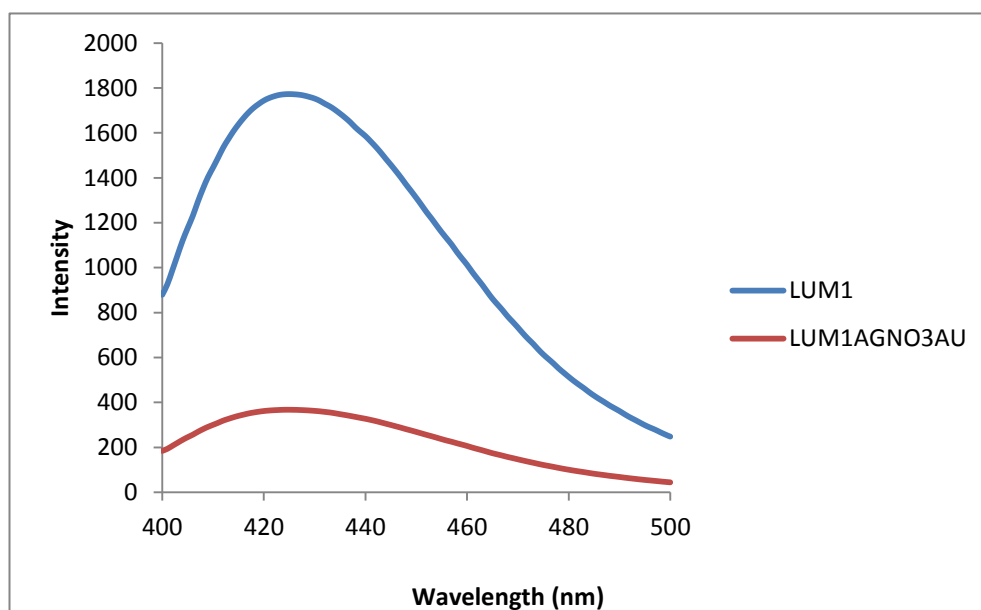


Figure 68: Fluorescence results for luminol and luminol doped with silica and gold nanoparticles

The investigation into gold and silver nanoparticle plasmon boosting proved unsuccessful, it was hoped that the luminescent peak (featured in Figure 68) would be boosted by the addition of gold nanoparticles and that the luminol could form the light source for the decomposition of taste and odour compounds, this part of the study was taken no further.

9.5 TITANIUM DIOXIDE NANOPARTICLES AND N-DOPED NANOPARTICLES

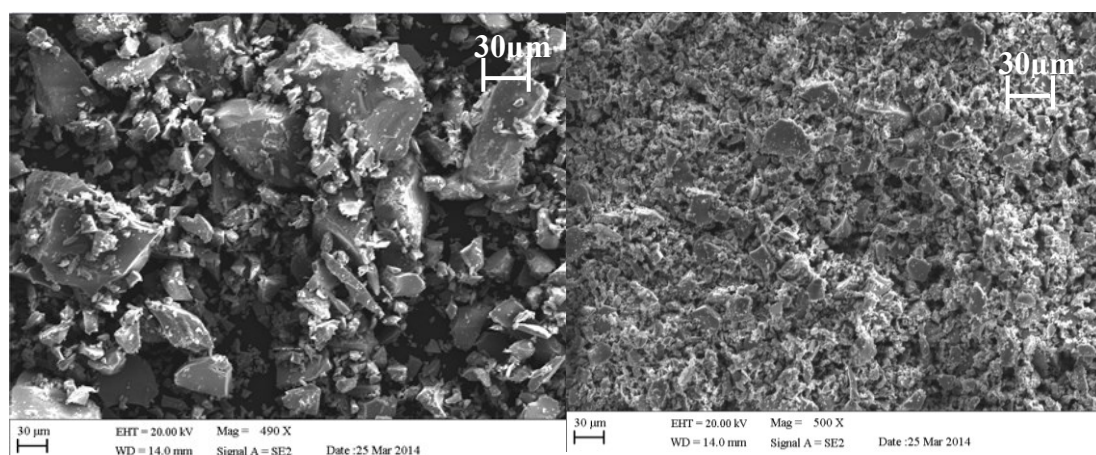
The use of titanium dioxide to break down T&O's is the main focus of this study, and so the type of TiO_2 to be used had to be considered. Magnetron sputtering presented a very convenient lab-based, that can easily be up-scaled method of producing thin films. TiO_2 nanoparticles were therefore synthesised and tested in the hope that they could be used as an alternative to the thin films for the degradation of both geosmin and MIB. TiO_2 nanoparticles were successfully synthesised and as can be seen, are bright white in pigment (Figure 69).



Figure 69: TiO_2 nanoparticles

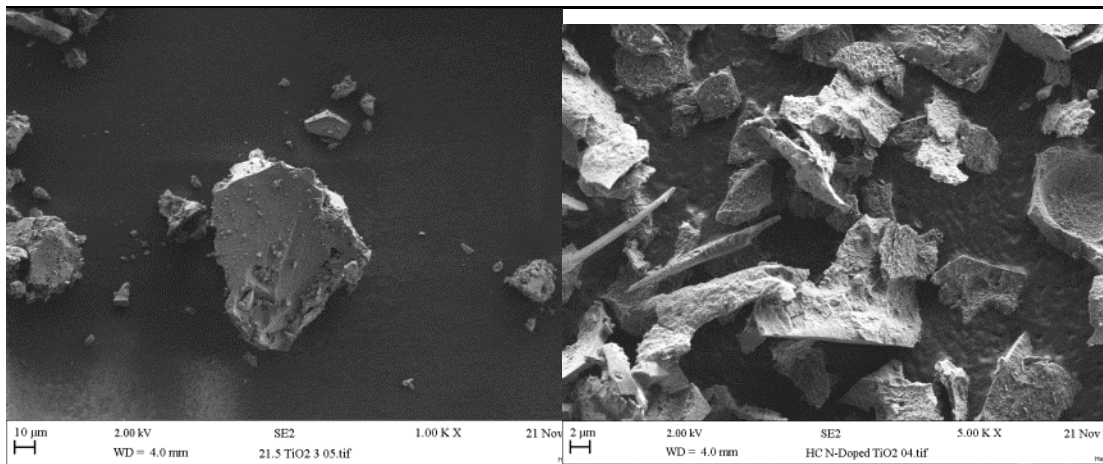
9.6 SEM RESULTS

Unlike the SEM results for titanium dioxide thin films, the nanoparticles are not as uniform, with many of the nanoparticles varying in size and shape, which can be seen from the images in Figure 70. It can also be seen that the titanium dioxide nanoparticles are much more angular, with high aspect ratios, compared to the spherical silica nanoparticles shown earlier. A cluster of tightly packed particles is visible in Np2 whereas the undoped Np3 were much more dispersed with greater size particles. The nitrogen doped nanoparticles took longer to synthesise, with more problems occurring in the annealing stage, but eventually, as seen in the SEM images, a cluster of nanoparticles were produced. The nanoparticles should have higher catalytic activity because they have a greater surface area, therefore more area will be exposed to the light.



A) TiO₂ Np1

B) TiO₂ Np2



C) TiO₂ Np3

D) N-doped TiO₂

Figure 70: Images A-D of the particles varying in shape and size

9.7 CONCLUSION

Unfortunately the nanoparticles did not produce enough evidence to advance this area of the study further as time constraints on the project meant that further focus on this idea would detract away from the main aims and objectives of the study. The titanium dioxide nanoparticles showed promise however thin film was the preferred material for up-scaling the project to industry. Titanium dioxide nanoparticles have a larger surface area so are promising as a catalyst however problems would arise in the drinking water treatment plant due to nanoparticles being flushed downstream. This would cause a problem particularly if these nanoparticles had been modified to contain the same dopants as the thin films e.g. Molybdenum; a potential heavy metal contaminant of drinking water and erbium oxide; a harmful contaminant if washed further in the treatment process. The use of nanoparticles could therefore, potentially

cause more problems than we started with, after all geosmin and MIB are non-toxic and not harmful on consumption.

Photocatalytic activity of the thin films coatings was recorded using the methylene blue test and results are presented in this chapter. The results and associated discussions are combined, with the conclusions at the end of the chapter.

10.1 PHOTOCATALYTIC ACTIVITY RESULTS

The natural rate of methylene blue dye degradation, was measured as a control, without contact to any photocatalytic surface, under both UV and visible light. In addition to this the rate of methylene blue dye degradation when in contact to a photocatalytic surface but without any light source irradiating the coating (i.e. in the dark) was also measured. In both these instances, the rate of degradation of methylene blue was of zero order (Figure 71) and so it can be deduced that any changes observed in the absorption peak height of methylene blue are instigated by the photocatalytic activity of the coating. As mentioned in section 7.13; the pH of the methylene blue solution was monitored and no or little change was observed in all tests.

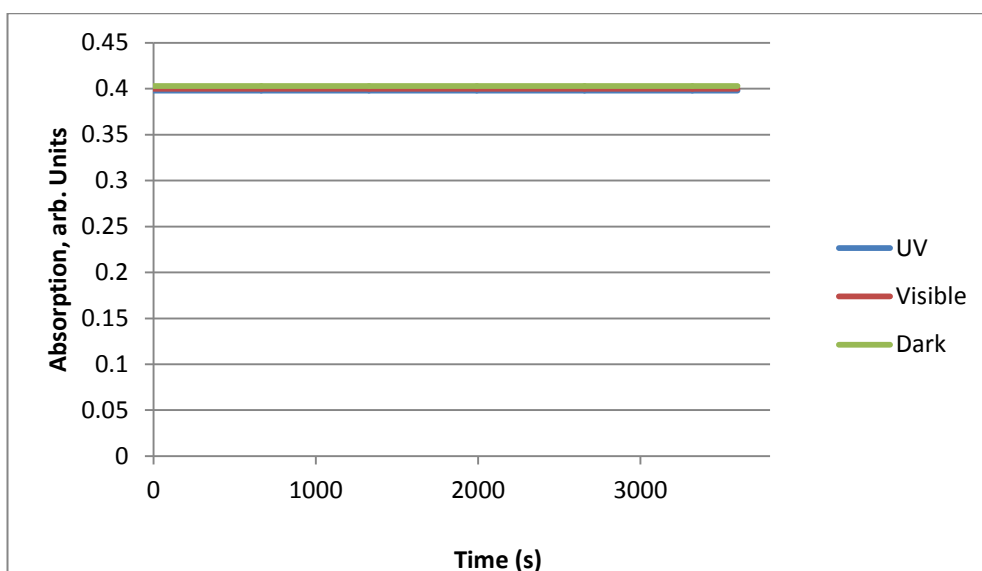


Figure 71: Degradation of methylene blue in the dark, under UV and Visible light

The Beer-Lambert law states:

$$A = \epsilon cl \quad \text{Eq.17}$$

Where ϵ is the molar extinction coefficient ($\text{mol}^{-1}\text{dm}^3 \text{cm}^{-1}$), c is the concentration (mol dm^{-3}) and l is the pathlength (cm). In the Beer-Lambert law the absorbance value is proportional to the concentration of the methylene blue dye. The Langmuir-Hinshelwood equation describes a heterogeneous catalysis process through the following equation:

$$\ln(C_0 / C) K_a t \quad \text{Eq.18}$$

Substituting (A_0/A_t) absorbance at time 0 and A_t – absorbance of methylene blue at 665nm at the time of the experiment gives a linear relationship where the gradient gives the K_a value. The K_a value is the first order rate constant for a chemical reaction known as dissociation in the context of reactions. The larger the K_a value, the more dissociation of the molecules in solution. Therefore, a higher K_a value shows high photocatalytic activity.

$$K_a = \ln(A_0 / A_t) \quad \text{Eq. 19}$$

In this study *Pilkington's AktivTM* was used as a control. This ensures that the test is reliable and provides a baseline study sample which provides a bench mark for thin films created in this study. The rate constant for the decomposition of methylene blue (K_a value) for this control was found to be $3 \times 10^{-5} \text{s}^{-1}$ under UV radiation and $2 \times 10^{-5} \text{s}^{-1}$ under visible light. Indicating that anything found higher or the same than this, would be considered to have good photocatalytic activity. The thin films studied for photocatalytic performance include N-TiO₂, Er-TiO₂ and undoped TiO₂. As for Mo-TiO₂ thin films a number of issues arose with the binding of the thin film to the substrate and therefore leaching into the methylene blue solution occurred. This leaching would prove disastrous in the drinking water treatment process as molybdenum would be considered a heavy metal contaminant in the water if leached from the film surface during the proposed photocatalytic treatment phase and so the testing of the Mo-TiO₂ films was taken no further.

10.2 TiO₂ RESULTS

Photocatalytic results for undoped TiO₂ reveal the K_a value under UV radiation to be $3 \times 10^{-6} \text{s}^{-1}$ and $5 \times 10^{-7} \text{s}^{-1}$ under visible light (Figure 72). These are significantly lower than the *Pilkingtons AktivTM*, which is to be expected. The value under UV light shows that although a small value, these TiO₂ thin films do possess photocatalytic ability under UV light. The photocatalytic ability under visible light is very small but still active.

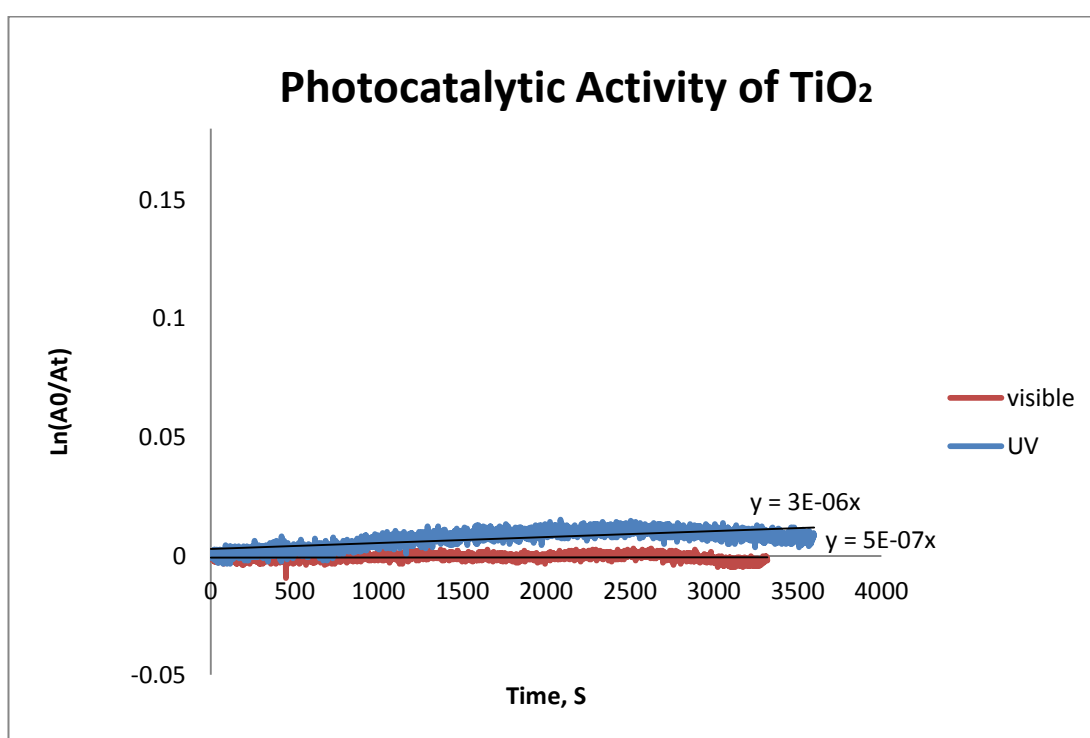


Figure 72: Methylene blue photocatalytic results for TiO₂

10.3 N- TiO₂ RESULTS

Photocatalytic results for N-TiO₂ reveal the K_a value under UV radiation to be $4 \times 10^{-5} \text{s}^{-1}$ and $3 \times 10^{-5} \text{s}^{-1}$ under visible light (Figure 73). These are significantly higher than the undoped TiO₂ and show the increase in photocatalytic activity due to the narrowing of the band gap observed in section 9.10. These values are also higher than *Pilkingtons AktivTM*, which indicates that a material with greater photocatalytic properties has successfully been produced and tested.

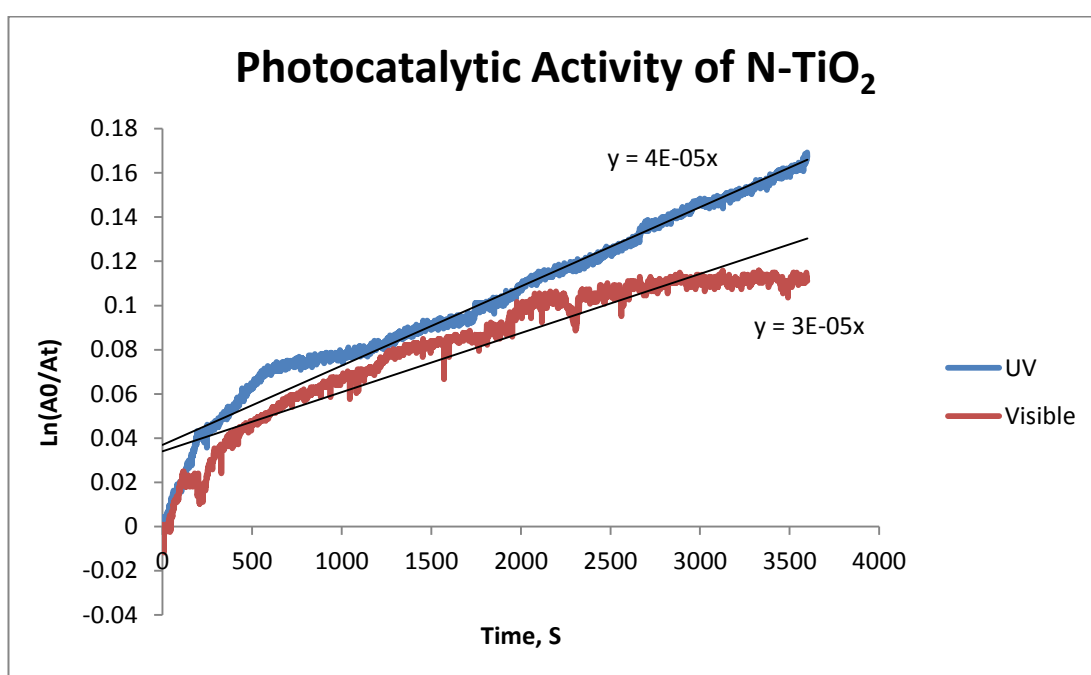


Figure 73: Methylene blue photocatalytic results for N-TiO₂

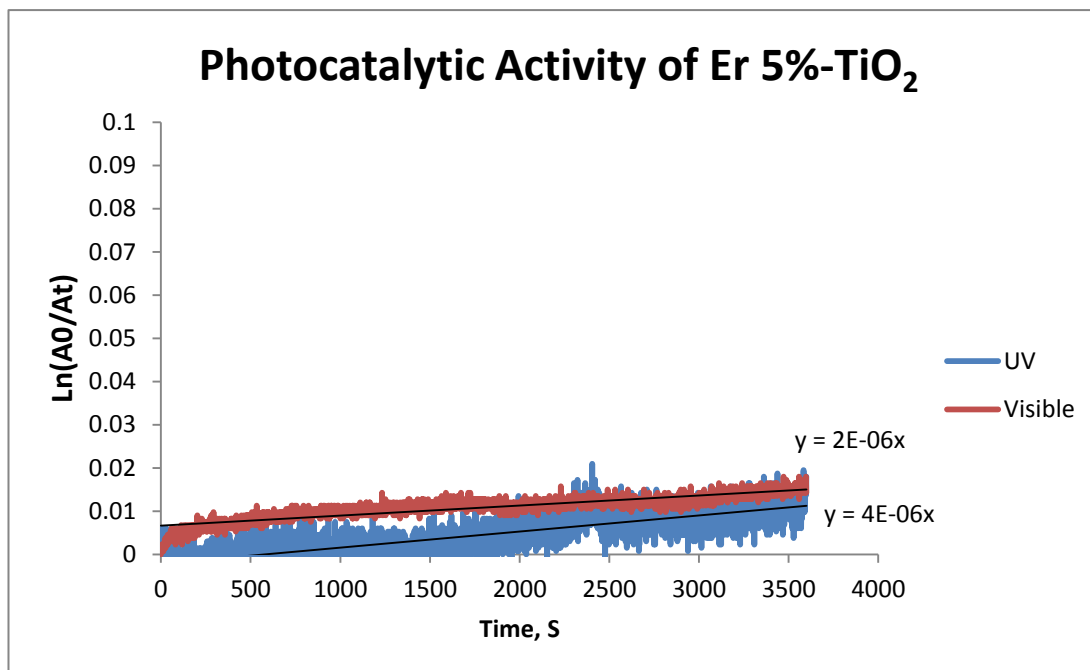


Figure 74: Methylene blue photocatalytic results for Er 5%-TiO₂

Photocatalytic results for Er 5%-TiO₂ reveal the K_a value under UV radiation to be $4 \times 10^{-6} \text{s}^{-1}$ and $2 \times 10^{-6} \text{s}^{-1}$ under visible light (Figure 74). Photocatalytic results for Er 7.5%-TiO₂ reveal the K_a value under UV radiation to be $8 \times 10^{-6} \text{s}^{-1}$ and $2 \times 10^{-6} \text{s}^{-1}$ under visible light (Figure 75).

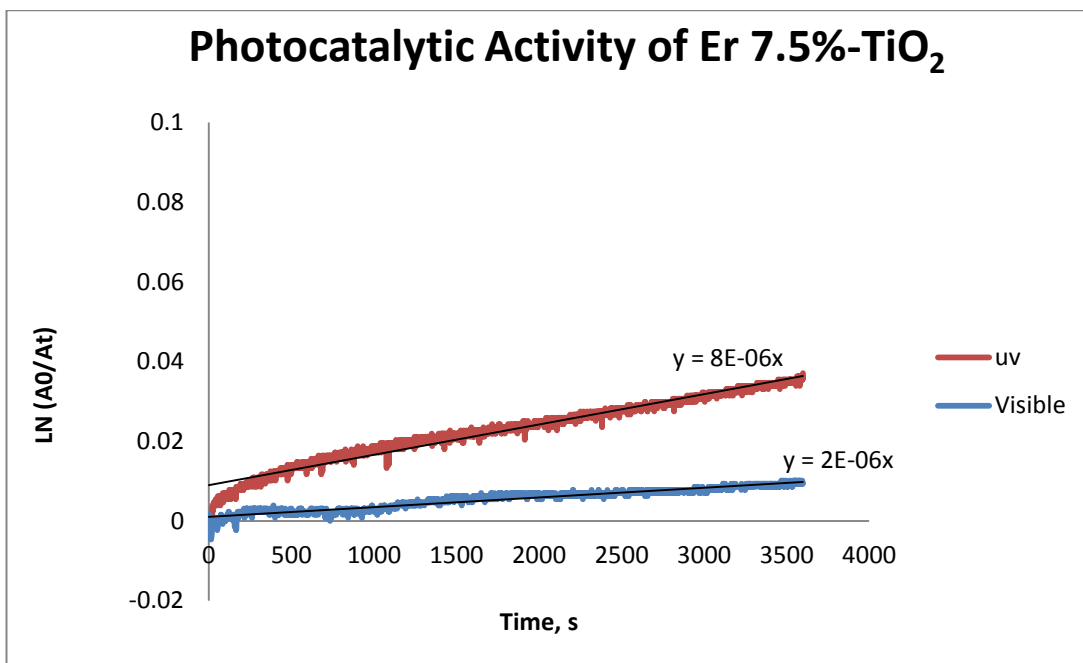


Figure 75: Methylene blue photocatalytic results for Er 7.5%-TiO₂

Photocatalytic results for Er 10%-TiO₂ reveal the K_a value under UV radiation to be $1 \times 10^{-5} \text{s}^{-1}$ and $2 \times 10^{-6} \text{s}^{-1}$ under visible light (Figure 76). Photocatalytic results for Er 12.5%-TiO₂ reveal the K_a value under UV radiation to be $6 \times 10^{-6} \text{s}^{-1}$ and $5 \times 10^{-6} \text{s}^{-1}$ under visible light (Figure 77).

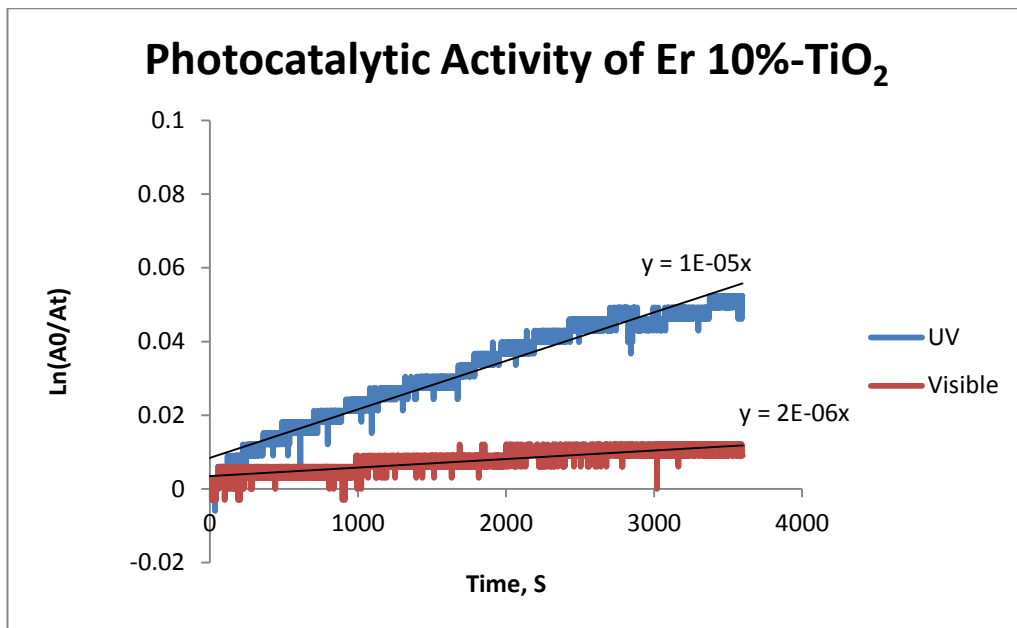


Figure 76: Methylene blue photocatalytic results for Er 10%-TiO₂

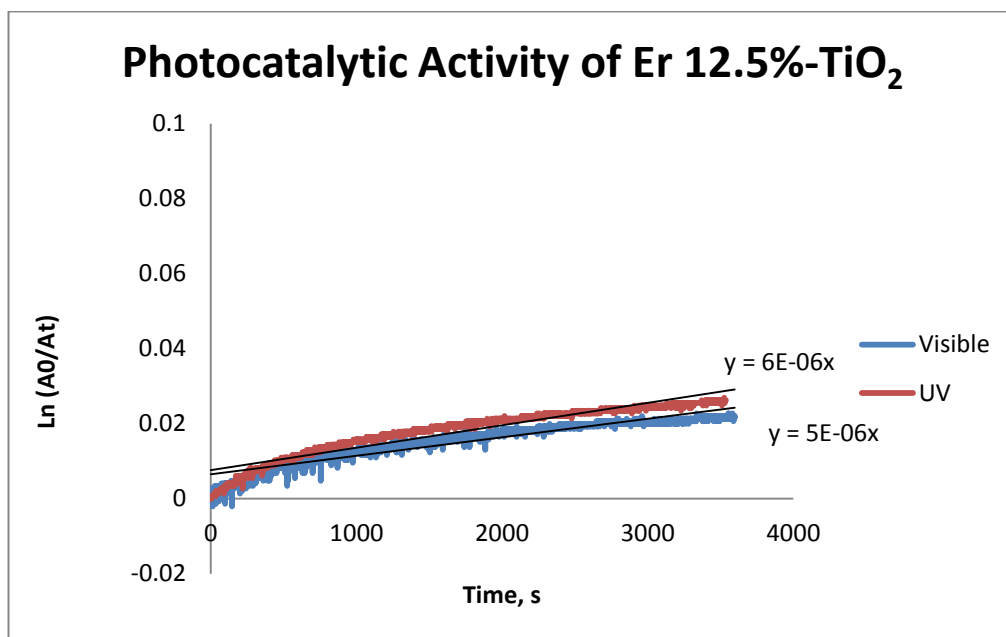


Figure 77: Methylene blue photocatalytic results for Er 12.5%-TiO₂

The Er-TiO₂ film with the most catalytic activity is the 10% target, under UV light, whereas the 12.5% target had the highest visible light activity. All of the erbia films had lower visible light activity than both the *pilkington AktivTM* and N-TiO₂. The dopant with the most photocatalytic ability is therefore, nitrogen doped titanium dioxide thin films. The erbia films do show an increased activity compared to undoped TiO₂, and so can be deemed a success in achieving photocatalytic breakdown of methylene blue. The reason for a worse photocatalytic performance compared to the N-TiO₂ thin films could be due to the high amount of erbia dopant. Problems can arise when changing the composition of TiO₂ so much. When there is a large amount of dopant it can prevent re-alignment of electrons and holes and thus causing the titanium dioxide to be rutile phase not anatase and therefore lowering the photocatalytic performance. Doping in high amounts can also promote the creation of charge-capture centres which act as hole-electron recombination centres and therefore lead to a loss in photocatalytic activity. The low photocatalytic activity observed in the erbia thin films could therefore be explained by any of the following explanations:

- Loss of crystallinity in the doped samples
- Large amounts of rutile phase titanium dioxide causing the low activity (confirmed by raman spectra section 8.6)
- Electron-hole recombination sites formed at dopant sites of the coating
- If the dopant becomes excessive, it can cover the surface of titania and thus reduce the photocatalytic activity.

The results of the rate constants have been converted to min^{-1} and the decomposition of methylene blue for the thin films produced are presented in Table 21 for direct comparison.

Table 21: Comparison of rate constants for the decomposition of methylene blue

Film	Rate constant	
	UV light	Visible light
	k_a (min^{-1})	k_a (min^{-1})
<i>Aktiv</i>	0.0018	0.0012
TiO₂	0.00018	0.00003
N-TiO₂	0.0024	0.0018
Er 5%-TiO₂	0.00024	0.00012
Er 7.5%-TiO₂	0.00048	0.00012
Er 10%-TiO₂	0.0006	0.00012
Er 12.5%-TiO₂	0.00036	0.0003

Photocatalytic activity is linked to anatase formation. Low temperature annealing allows the anatase phase to develop which then has a positive effect on the photocatalytic ability. When the coating has a significant red shift and the presence of anatase, an improvement on the photocatalytic properties can be observed and this is confirmed in the case of the N-TiO₂ thin films. Increasing the dopant material in the coating can be shown to increase the band gap shift however this can also inhibit anatase formation and so a balance of these two properties should be found. It is

therefore important to consider the optimum amount of dopant in future thin film creation.

10.5 CONCLUSION

Titanium dioxide thin films and thin films doped with N and Er were analysed via the degradation of methylene blue organic dye to test their photocatalytic properties and ability. Photocatalytic results revealed that the most photocatalytically active material was N-TiO₂. Erbium oxide doped thin film K_a results revealed a trend, the more of the oxide dopant, the better the photocatalytic performance under visible light. The same was true for UV light, to an optimum of 10%, as the 12.5% thin film's had decreased activity under UV light. The visible light experiments show an improvement in the photocatalytic properties of the TiO₂ coatings and show a significant red shift in the band gap value. Increasing the erbia dopant inhibits the anatase formation of the thin film. An optimum amount of dopant can capture photogenerated electrons and decrease electron hole recombination rate. N-TiO₂ photocatalytic results show promise for these films to be used in the water industry as there is a significant increase in photocatalytic activity under both visible and UV light. The measuring of photocatalytic activity of the materials allows for further study into breakdown of geosmin and MIB using the thin film materials. Such work and results are detailed in Chapter 11.

CHAPTER 11 GC-MS ANALYSIS AND THE DEGRADATION OF GEOSMIN AND MIB RESULTS

This chapter presents the results of GC-MS analysis on the two T&O compounds studied in this thesis, geosmin and MIB. The results and associated discussions are combined with the conclusions at the end of the chapter. Presented within these results; the determination of the rates of degradation of these two compounds under different reaction conditions along with the best reaction conditions found from this study. This chapter also discusses possible reaction pathways and degradation products.

11.1 GEOSMIN RETENTION TIME

Geosmin and MIB are identified by their retention time and their mass spectra. Geosmin has a retention time of 10 minutes (Figure 78). The extracted ion current for the parent ion of each compound exhibits one peak. Total ion current data was collected in the scan range from m/z 40 to 200. The product ions for geosmin have a m/z value of 112 (Figure 79).

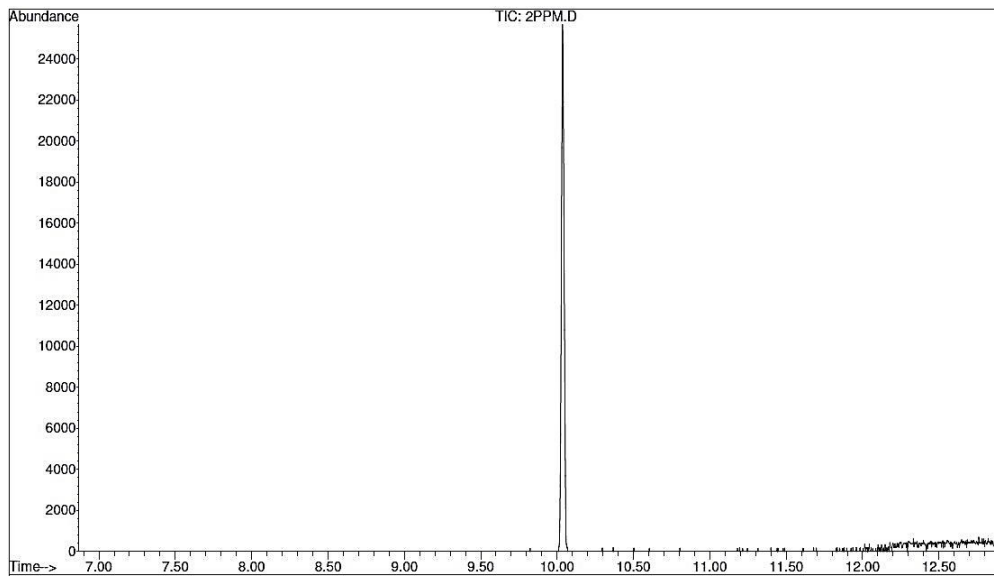


Figure 78: Example GC-MS spectrum for geosmin dissolved in methanol and water with a clear peak at 10minutes

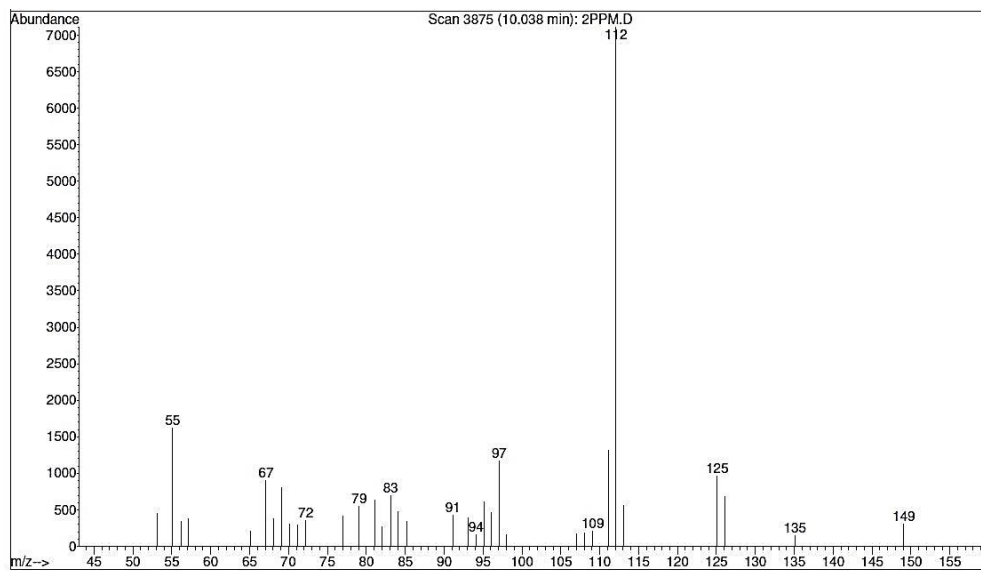


Figure 79: Geosmin product ions clear m/z 112 peak

11.1.1 GEOSMIN CALIBRATION

For quantifying the peak height of the geosmin peak calibration curves were carried out and equations fitted, standard deviations were between 1.5% and 3.2% for geosmin, the geosmin curve trended towards zero and excellent linearity of the peaks areas versus concentration was obtained for geosmin with $R^2 > 0.9992$ for twelve concentrations across a range from 0.25ppm to 2000ppm (Figure 80).

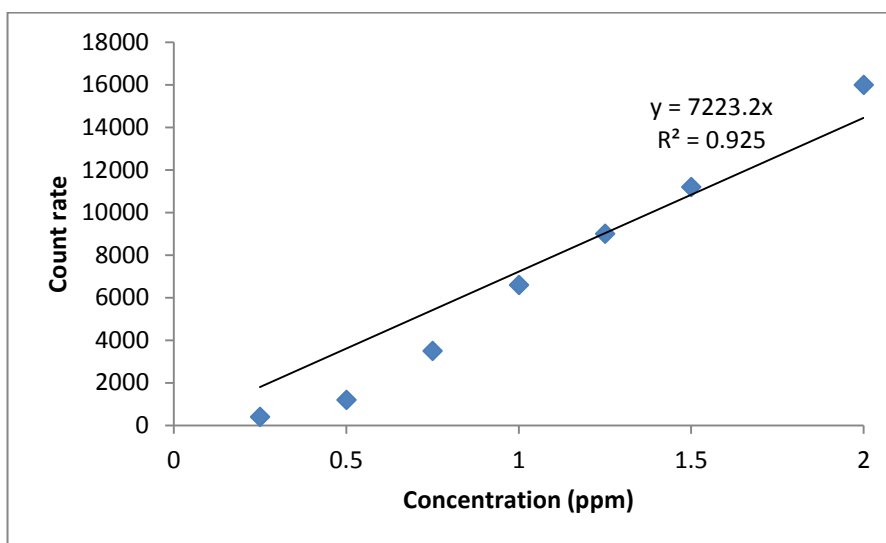


Figure 80: GC-MS geosmin calibration plot concentration up to 2ppm

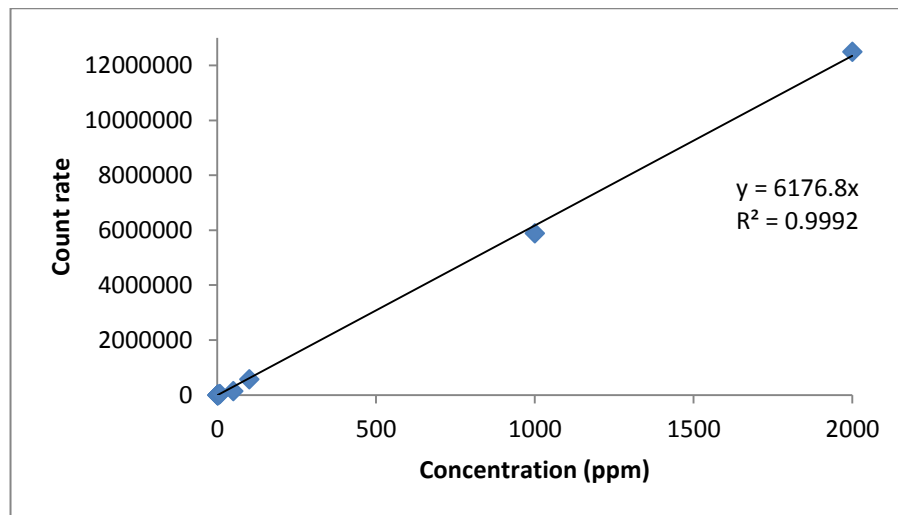


Figure 81: GC-MS geosmin calibration plot concentration up to 2000ppm

11.2 MIB RETENTION TIME

MIB has a retention time of 8 minutes (Figure 82). Total ion current data was collected in the scan range from m/z 40 to 200, product ions for MIB have a m/z value of 95 (Figure 83).

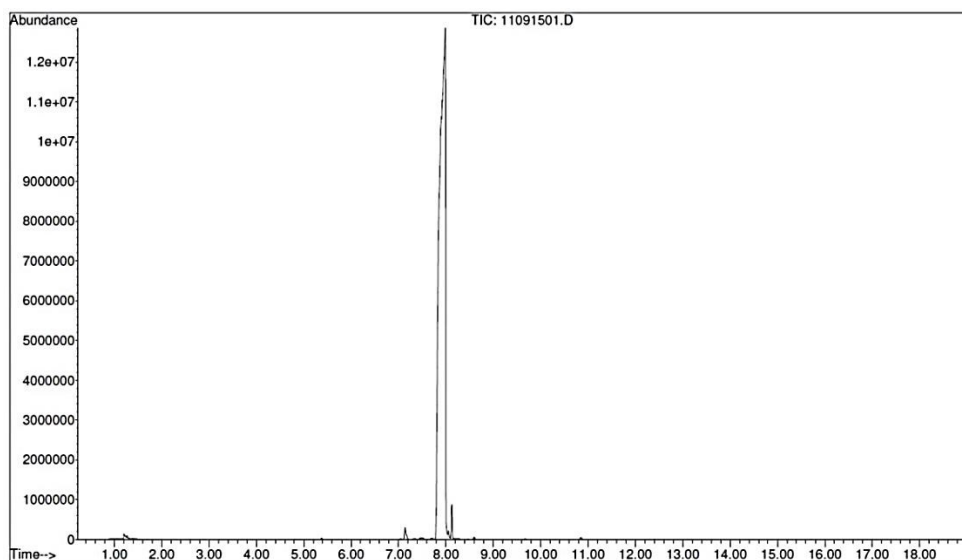


Figure 82: Example GC-MS spectrum for MIB dissolved in methanol and water with a clear peak at 8minutes

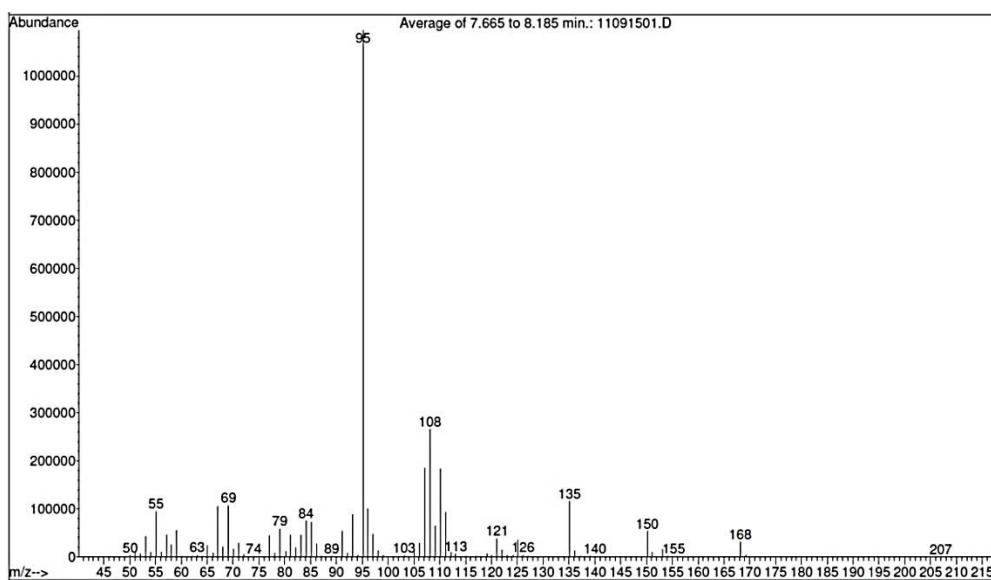


Figure 83: MIB product ions clear m/z 95 peak

11.2.1 MIB CALIBRATION

For quantifying the peak heights of MIB, calibration curves were carried out and equations fitted, standard deviations of MIB were between 2 to 4% average, the MIB curve trended towards zero and very good linearity of the peaks areas versus concentration was obtained for MIB with $R^2 > 0.9854$ for twelve concentrations across a range from 0.25ppm to 2000ppm (Figure 84).

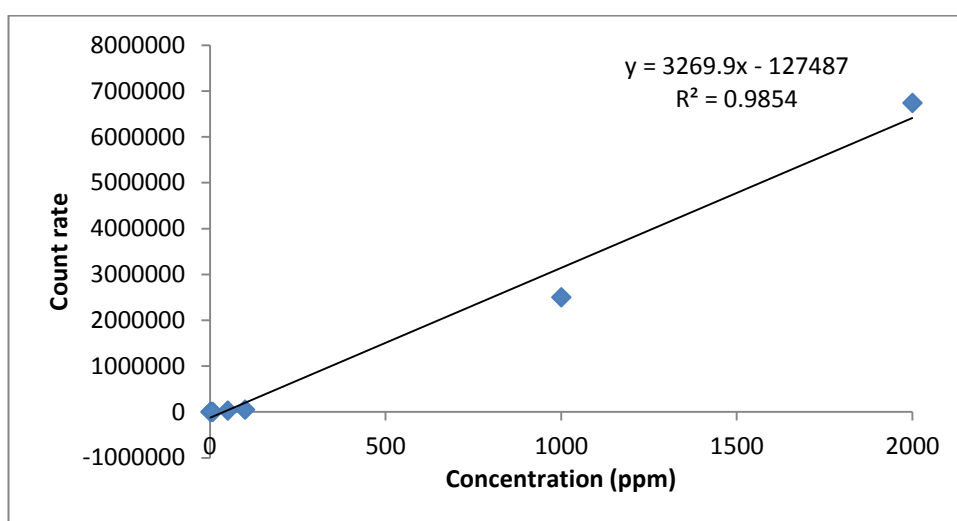


Figure 84: GC-MS calibration plot for MIB concentrations up to 2000ppm

This method therefore provides easy, accurate and sensitive odour compound analysis in drinking water.

11.3 REPRODUCIBILITY OF METHOD

Five runs of the same experimental conditions were observed and recorded and standard deviations were calculated. For each set of analysis, peak height and peak

areas were averaged and the standard deviation was calculated via the following equation:

$$\text{STD} = \sqrt{\sum \frac{(x - \bar{x})^2}{(n - 1)}} \quad \text{Eq. 20}$$

Where: x = each value in the set, n is the number of values and \bar{x} is the average (statistical mean) of the values.

Standard deviations were typically very small showing reproducibility in the method, with the average value for most data being less than 4%. It is important to note that the GC-MS was used by other users and at times, the first run of the day gave large variation in the results. In order to overcome this problem, when large variations were observed, ethanol was flushed through the column and the tests restarted so that runs were repeated and outliers omitted.

11.4 EFFECT OF UV LIGHT TREATMENT

The effect of UV light treatment on geosmin and MIB degradation was observed. The degradability of geosmin was tested in a range that is far higher than the odour threshold concentration for humans. OH radicals (described in section 3.2) are the reactive component in the presence of UV light. The intensity of the UV light determines the concentration of the photogenerated electron-hole pairs, which can then influence the degradation rate of the organic compounds. The duration of the

experiment (150mins) therefore is a contributing factor to the total energy emitted by the UV light. The energy emitted by the UV light is estimated by:

$$E = 60P\eta T \quad \text{Eq. 21}$$

Whereby E is the energy emitted from the lamp, P is the power of the lamp (W), η is the efficiency of the lamp in converting the electrical energy into UV light and T is the transmittance of the UV lamp through the cylinder of geosmin/MIB. This is multiplied by 60 in order to convert the value from J/s to J/min. For the 150 minute exposure time the UV dose was estimated to be 4000J/min. Previous studies¹²⁹ have indicated that the rate constant of the degradation for geosmin is increased with increasing UV intensity. In this study however, the UV intensity remains the same for all experiments carried out. Both UV and visible light were tested to degrade the geosmin and MIB with no photocatalyst present and results are presented within Table 22.

Table 22: Degradation results for geosmin and MIB under UV and visible light

Sample and light source	Geosmin		MIB	
	%	%	%	%
	Degradation 150 mins	Error (+/-)	Degradation 150 mins	Error (+/-)
UV alone	80.31	0.40	87.90	1.07
Visible alone	39.39	0.19	62.06	0.30

UV treatment proved effective however not very effective at removing geosmin and MIB from the samples, this is perhaps because both compounds have a low susceptibility to UV light and the combination of UV light and a photocatalyst is needed.

11.5 EFFECT OF UV AND VISIBLE LIGHT WITH TiO₂ TREATMENT

The combination of UV light with a TiO₂ thin film produced via magnetron sputtering to degrade the compound geosmin was observed. The effect of TiO₂ under visible light was also investigated, to see the effects of TiO₂ without the UV light and subsequently, with UV light. The peak area of the geosmin spectra recorded on the GC-MS degrades over time in the presence of UV light and TiO₂ thin film as is shown in Figure 85.

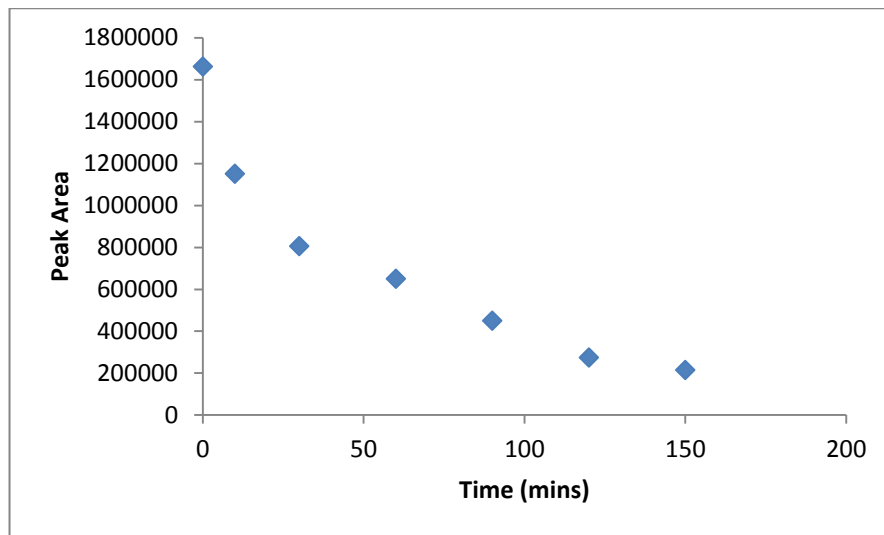


Figure 85: A graph to show degradation of geosmin in the presence of UV light and TiO₂.

11.6 DEGRADATION OF GEOSMIN WITH TiO₂ AND N- TiO₂ RESULTS

Testing of the degradation of geosmin with TiO₂ thin films and N-TiO₂ thin films produced the following results:

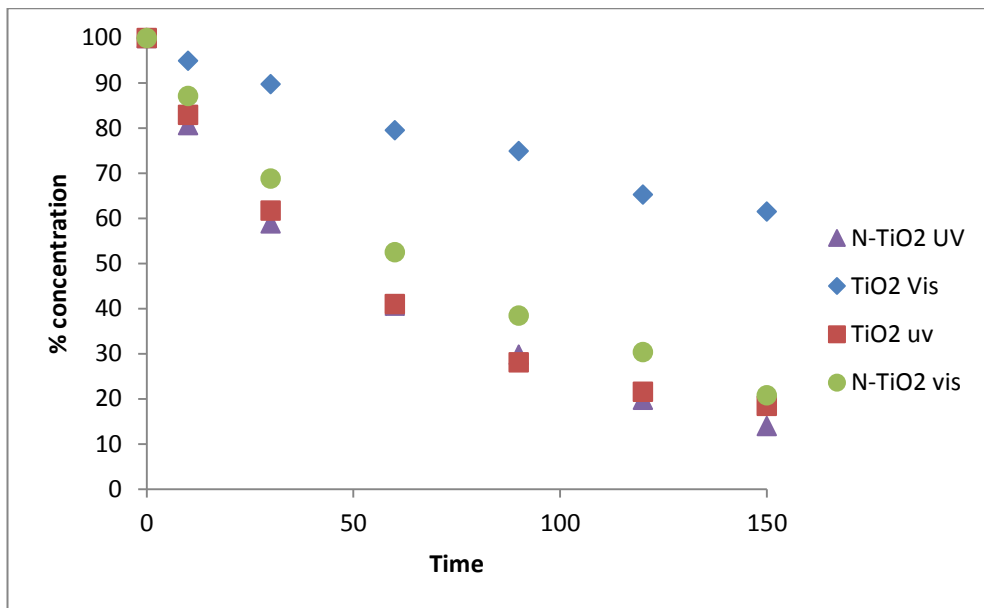


Figure 86: Geosmin % concentration degradation against time for TiO₂ and N-TiO₂

Interestingly geosmin degradation within the first half an hour follows a quicker trend than the last 120min of exposure to the photocatalyst, and although geosmin is not totally degraded, a 93.2% removal is achieved with N-TiO₂ thin film (Table 23).

Table 23: Percentage Geosmin degradation for TiO₂ and N-TiO₂

Sample and light source	% Degradation over	% Error (+/-)
	150min irradiation time	
N-Doped TiO₂ under UV	93.2%	0.03
TiO₂ under UV	88.3%	0.29
N-Doped TiO₂ under visible	80.2%	0.19
TiO₂ under Visible	39.1%	0.13

The first order rate constants for geosmin degradation with TiO₂ and N- TiO₂ thin films are determined in Figure 79. Plots of $\ln(C_0/C_t)$ vs time produced a straight line plot. This indicates that the degradation of geosmin follows first order kinetics with the equation:

$$\ln(C_o / C_t) = kt \quad \text{Eq. 22}$$

Where k is the rate constant, concentration at time 0 and C_t – concentration of geosmin at the time of the experiment gives a linear relationship where the gradient gives the rate constant.

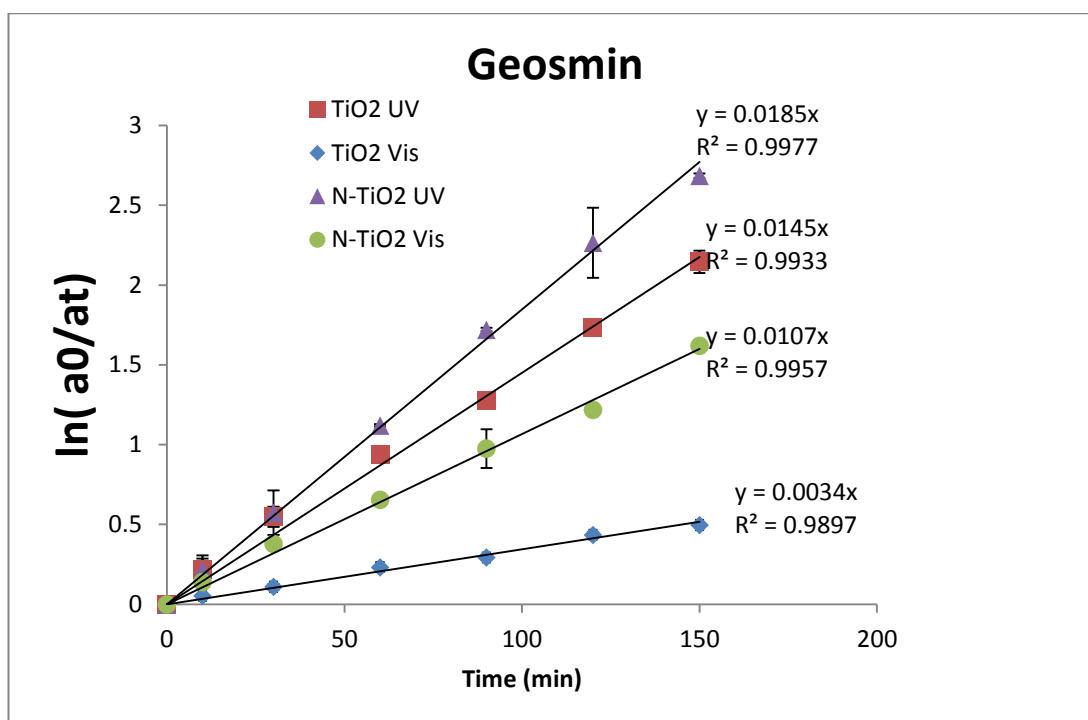


Figure 87: Geosmin rate of degradation calculation for TiO₂ and N-TiO₂

Linear plots were obtained in all cases with excellent correlation co-efficients ($R^2=0.9933-0.9977$) indicating the degradation follows pseudo first-order kinetics.

The highest decomposition rate constant was obtained with the UV and the N-TiO₂ film and was found to be 0.0185 min^{-1} , in comparison to UV excitation with the TiO₂ film which was 0.0145 min^{-1} . However, under visible light irradiation the rate for the N-TiO₂ film was found to be 0.0107 min^{-1} , whilst the lowest rate was found to be 0.0034 min^{-1} , indicating the nitrogen doping positively influences the photocatalytic activity under visible light illumination.

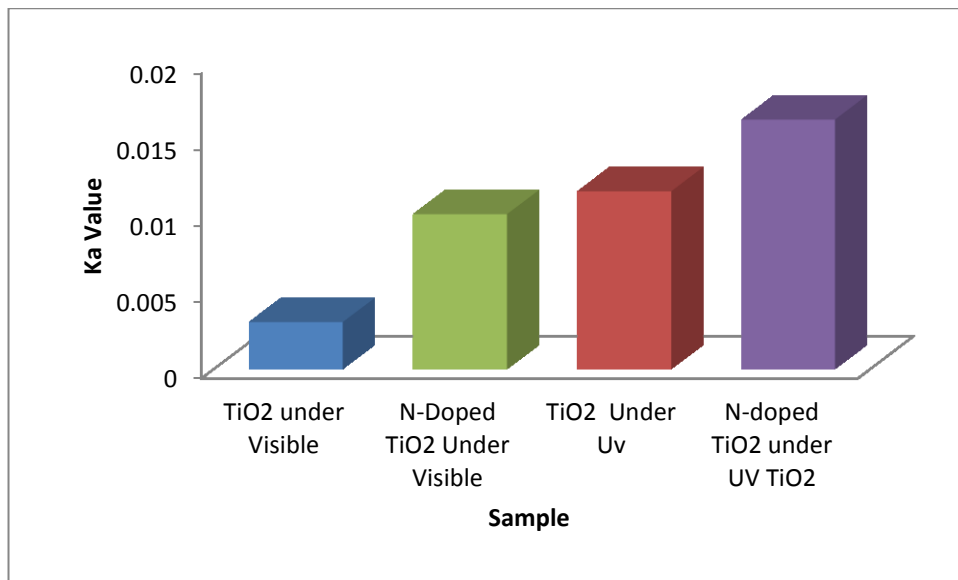


Figure 88: Comparison bar chart of Ka values for the degradation of geosmin for TiO₂ and N-TiO₂ thin films

Overall N- doped TiO₂ compared to TiO₂ performed better for the degradation of geosmin. As both films are anatase forms it can be concluded that the addition of a nitrogen dopant creates an enhancement in electron/hole separation and therefore increases the number of holes available for the degradation of geosmin and MIB, similar to the photocatalytic degradation of methylene blue described in section 10.3. BET surface area could also play an important role and therefore in this case a magnetron sputtered surface with higher surface roughness would be favoured to have a higher degradation rate for geosmin.

11.6.1 DEGRADATION OF MIB WITH TiO₂ AND N- TiO₂ RESULTS

Testing of the degradation of MIB with TiO₂ thin films and N-TiO₂ thin films produced the following results:

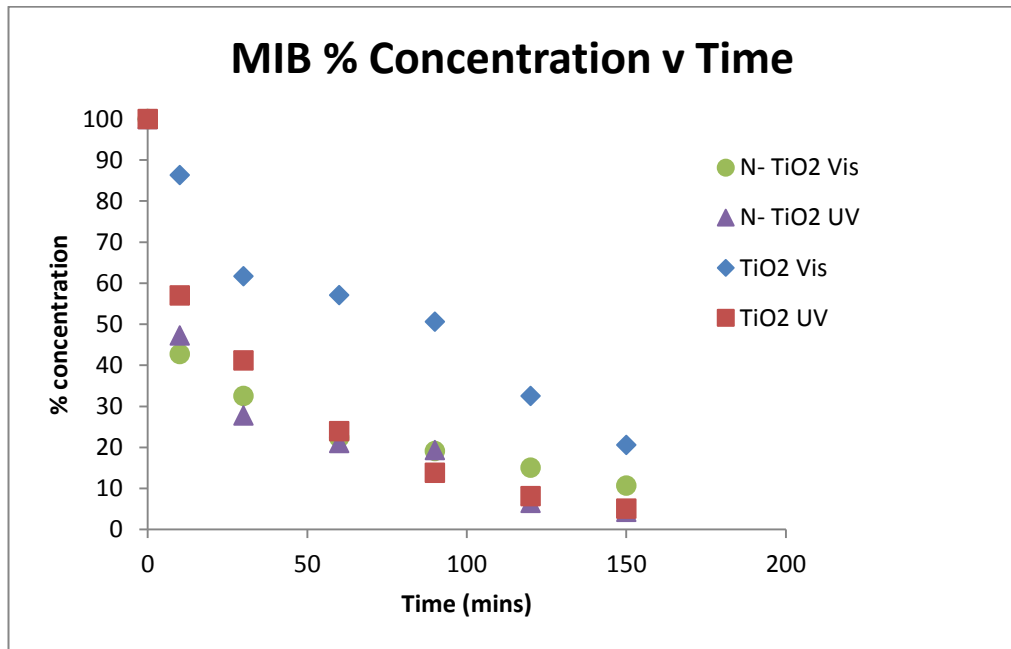


Figure 89: MIB %concentration degradation values against time for TiO₂ and N-TiO₂

Table 24 presents the removal rates for MIB using a photocatalyst and UV and visible light, with the greatest removal rate being 95.8%.

Table 24: Percentage degradation of MIB for TiO₂ and N-TiO₂

Sample and light source	% Degradation over	% Error (+/-)
	150min irradiation time	
N-Doped TiO₂ under UV	95.8%	2.5
TiO₂ under UV	94.9%	0.5
N-Doped TiO₂ under visible	89.5%	1.1
TiO₂ under Visible	79.8%	1.0

Linear plots were obtained with good correlation co-efficients ($R^2=0.6408-0.9639$) indicating the degradation follows pseudo first-order kinetics. The highest decomposition rate constant was obtained with the UV and the TiO₂ film and was found to be 0.0221 min^{-1} , in comparison to UV excitation with the N-TiO₂ film which was 0.0211 min^{-1} , this suggests that as long as there is a photocatalyst present, then MIB can degrade at a fast rate whilst under UV light. This is supported by the rate constants being very similar for both photocatalysts. Under visible light irradiation the rate for the N-TiO₂ film was found to be 0.0171 min^{-1} , whilst the lowest rate was found to be 0.0098 min^{-1} , indicating the nitrogen doping positively influences the photocatalytic activity under visible light illumination.

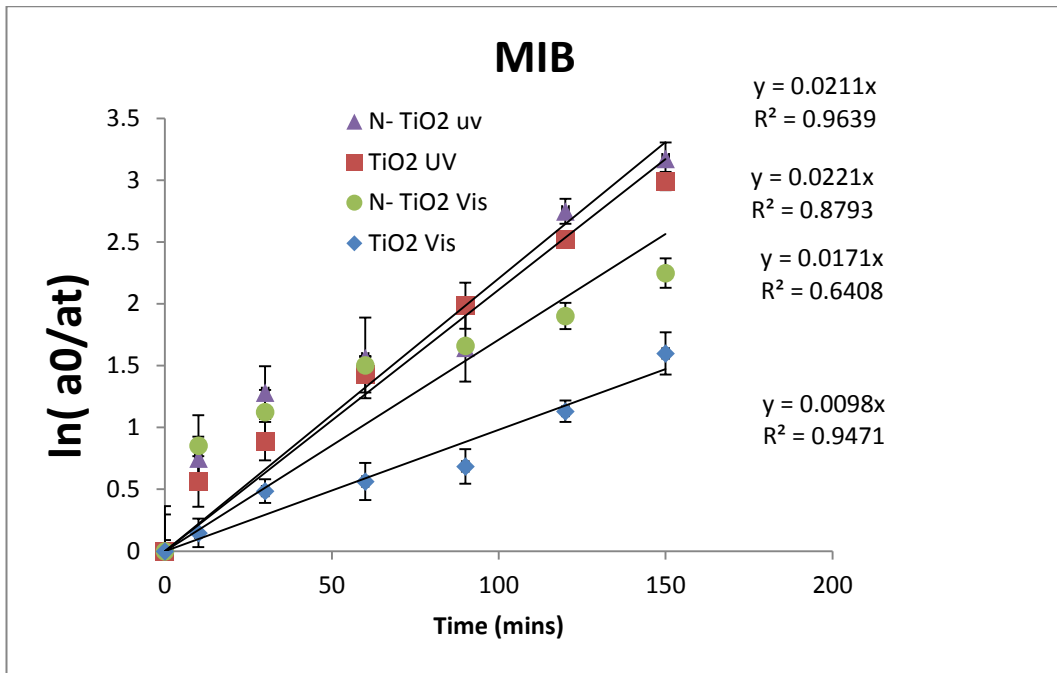


Figure 90: MIB rate of degradation calculation for TiO₂ and N-TiO₂

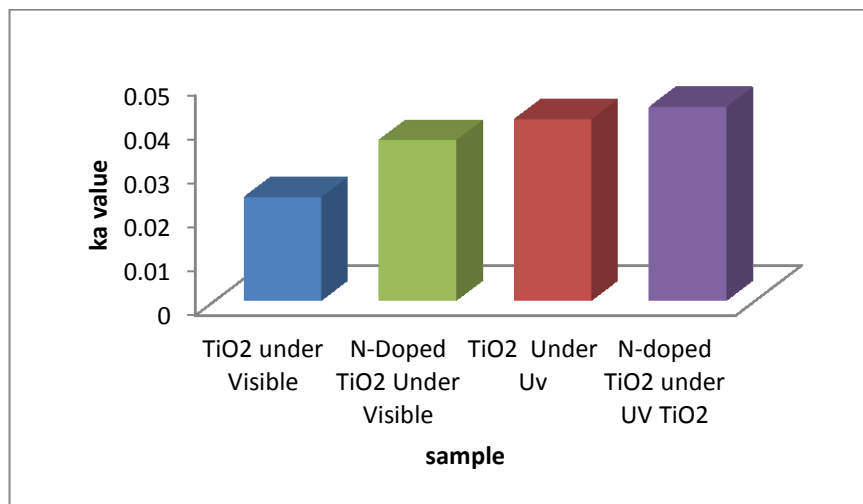


Figure 91: Comparison bar chart of ka values for the degradation of MIB for TiO₂ and N-TiO₂ thin films

11.7 DEGRADATION OF GEOSMIN USING UV LIGHT AND Er- TiO₂ RESULTS

Testing of the degradation of geosmin with Er-TiO₂ thin films under UV light produced the following results:

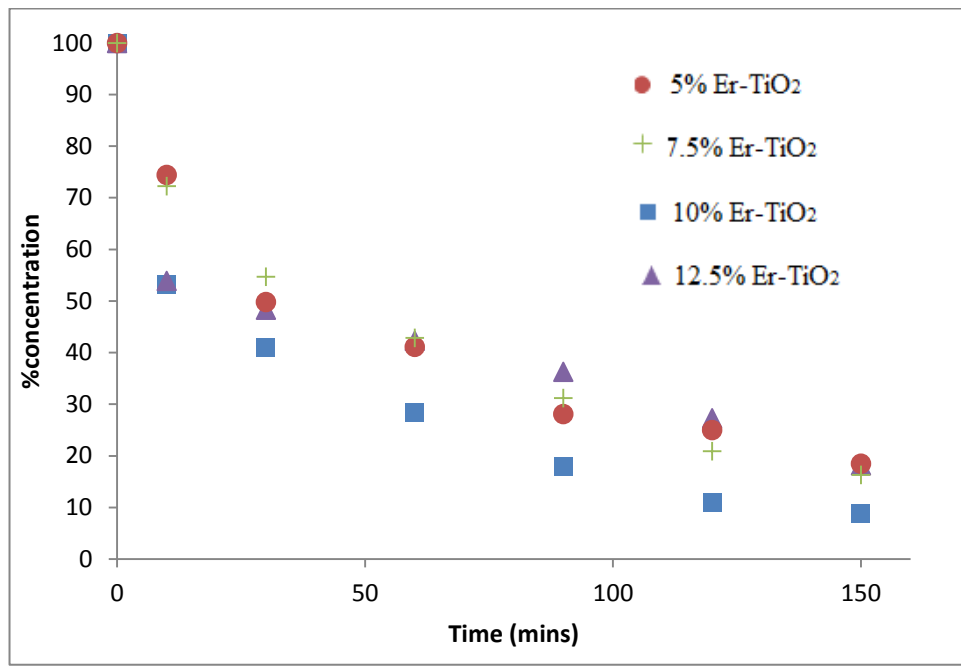


Figure 92: % concentration geosmin degradation values against time for Er-TiO₂ under UV light

Table 25 presents the removal rates for geosmin using a photocatalyst and UV light, with the greatest removal rate being 91.2%.

Table 25: Percentage degradation of geosmin under UV light for Er-TiO₂ thin films

Sample under UV	% Degradation over	% Error (+/-)
	150min irradiation time	
5% Er-TiO₂	85.9%	0.6
7.5% Er-TiO₂	86.1%	1.0
10% Er-TiO₂	91.2%	0.9
12.5% Er-TiO₂	83.8%	1.0

Linear plots were obtained with good correlation co-efficients ($R^2= 0.7277-0.9658$) indicating the degradation follows pseudo first-order kinetics.

The highest decomposition rate constant was obtained with the UV and the Er-TiO₂ film and was found to be 0.0179 min^{-1} from the 10% Er-TiO₂ thin film, in comparison to UV excitation with the TiO₂ film which was 0.0145 min^{-1} . whilst the lowest rate was found to be 0.0124 min^{-1} , which is worse than the performance with undoped thin film.

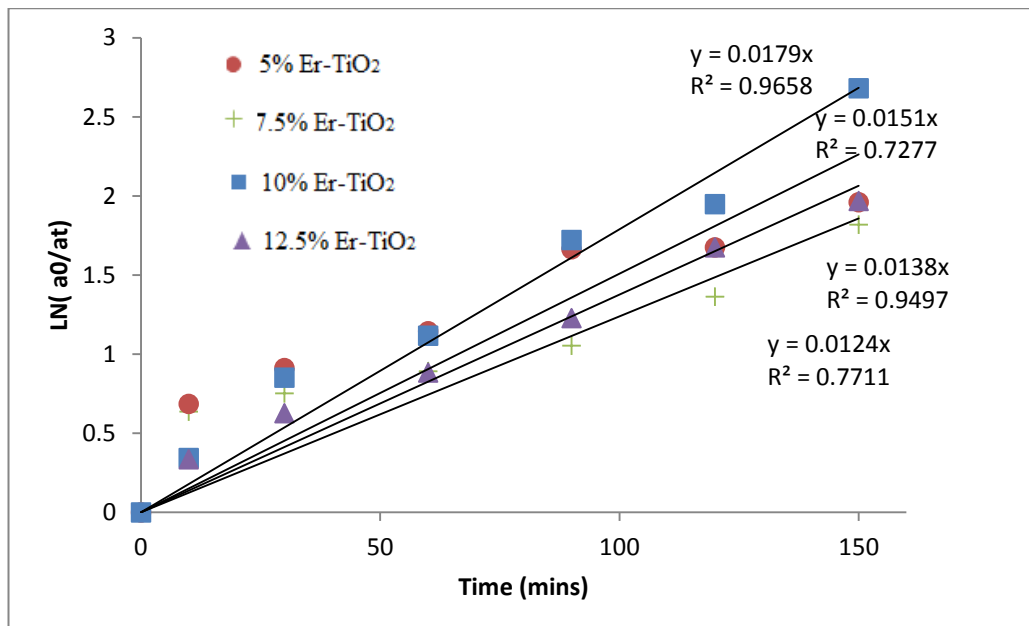


Figure 93: Geosmin rate of degradation calculation under UV light

11.7.1 DEGRADATION OF GEOSMIN USING VISIBLE LIGHT AND Er- TiO₂ RESULTS

Testing of the degradation of geosmin with Er-TiO₂ thin films under visible light produced the following results:

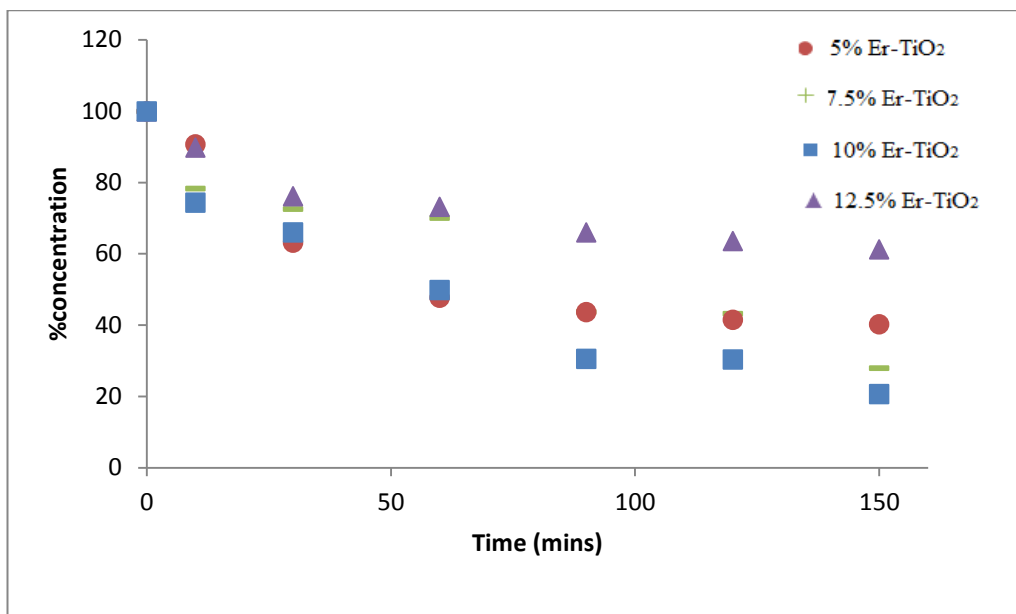


Figure 94: % Concentration geosmin degradation values against time for Er-TiO₂ under visible light

Table 26: Percentage degradation of geosmin under visible light for Er-TiO₂ thin films

Sample under visible light	% Degradation over	% Error (+/-)
150min irradiation time		
5% Er-TiO₂	67.4%	1.54
7.5% Er-TiO₂	74.9%	0.72
10% Er-TiO₂	77.1%	0.59
12.5% Er-TiO₂	39.4%	3.86

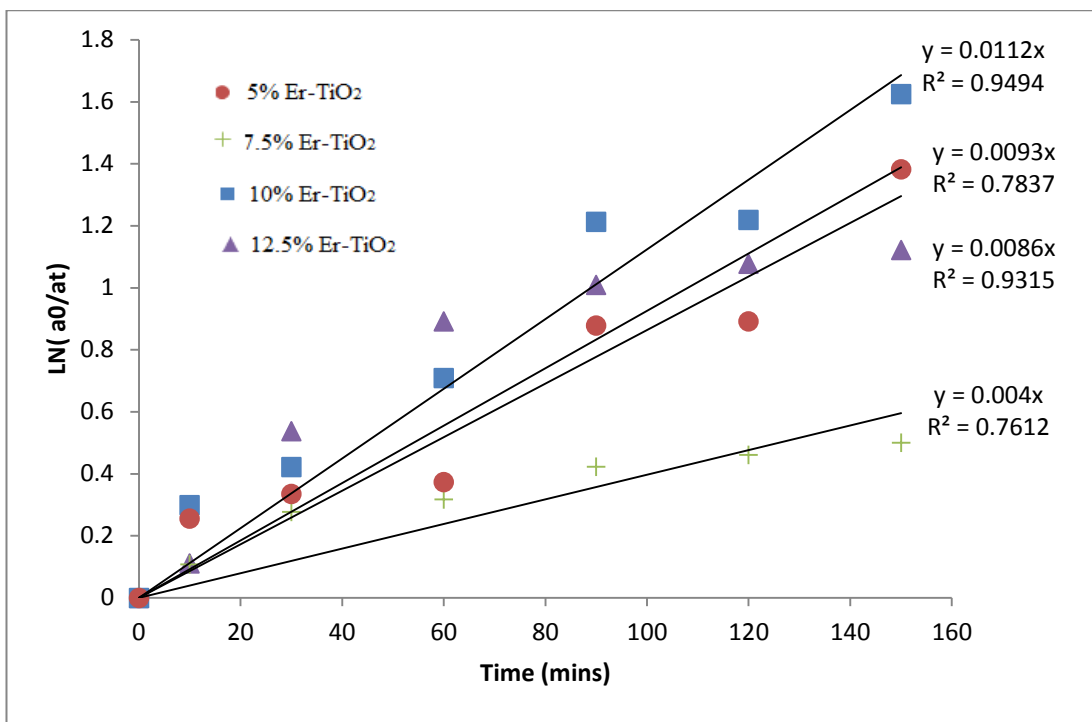


Figure 95: Geosmin rate of degradation calculation under visible light

Linear plots were obtained with good correlation co-efficients ($R^2=0.7612-0.9494$) indicating the degradation follows pseudo first-order kinetics.

The highest decomposition rate constant was obtained with the UV and the Er-TiO₂ film and was found to be 0.0112 min^{-1} from the 10% Er-TiO₂ thin film, whilst the lowest rate was found to be 0.0040 min^{-1} , which is worse than the performance with undoped thin film.

11.7.2 DEGRADATION OF MIB USING UV AND Er- TiO₂ RESULTS

Testing of the degradation of MIB with Er-TiO₂ thin films under UV light produced the following results:

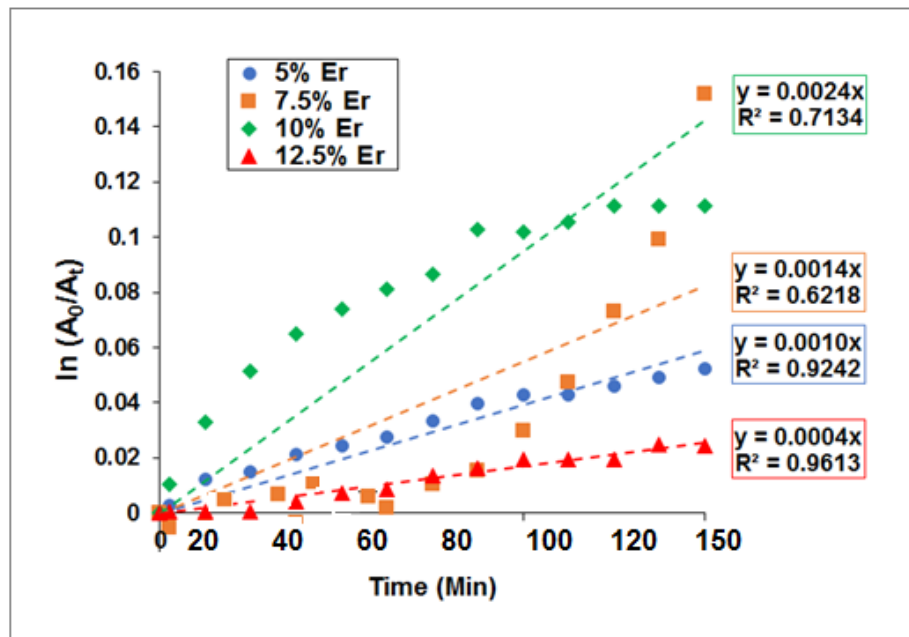


Figure 96: MIB rate of degradation calculation under UV light

The highest decomposition rate constant was obtained with the UV and the Er-TiO₂ film and was found to be 0.0024 min⁻¹ from the 10% Er-TiO₂ thin film, whilst the lowest rate was found to be 0.0004 min⁻¹.

11.7.3 DEGRADATION OF MIB USING VISIBLE LIGHT AND Er- TiO₂ RESULTS

Testing of the degradation of MIB with Er-TiO₂ thin films under visible light produced the following results:

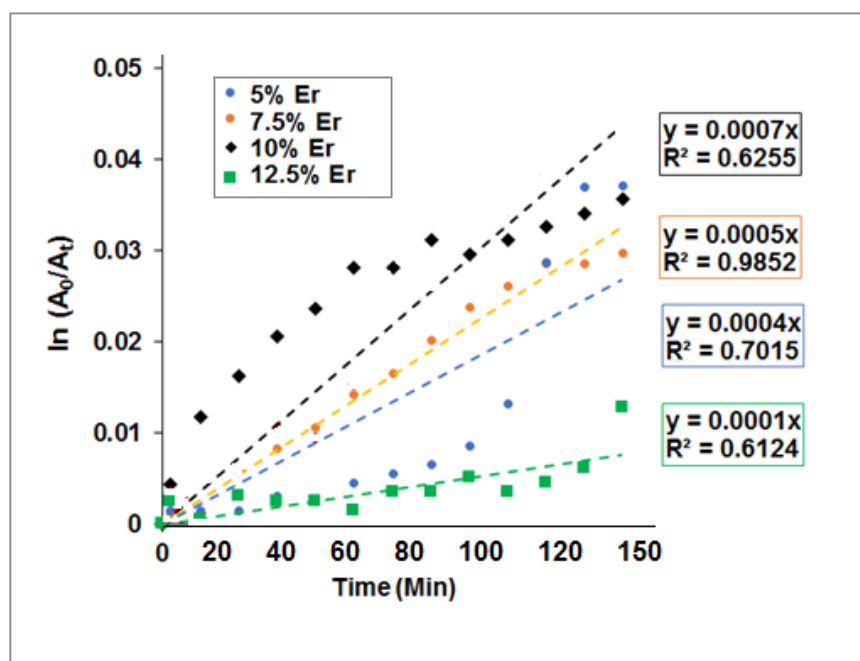


Figure 97: MIB rate of degradation calculation under visible light

The highest decomposition rate constant was obtained with the UV and the Er-TiO₂ film and was found to be 0.0007 min⁻¹ from the 10% Er-TiO₂ thin film, whilst the lowest rate was found to be 0.0001 min⁻¹.

Rate constant results for the degradation of geosmin under UV light (Table 27), reveal that the thin film coating to breakdown the most geosmin was the N-TiO₂ with a removal rate of 0.0185min⁻¹ under UV light and a removal rate of 0.0107 min⁻¹ under visible light. Removing 93.2% of the compound under UV and 80.2% of the compound under visible N-TiO₂ was also the most successful thin film coating at breaking down MIB (Table 28) removing 95.8% of the compound under UV light and 79.8% under visible light, with rate constant removal rate of 0.0189 min⁻¹ and 0.0122 min⁻¹ respectively.

Table 27: Comparison of rate constants for the degradation of geosmin using various thin films under UV and visible light

Film	Rate constant	Rate constant
	UV light	Visible light
	k_a (min ⁻¹)	k_a (min ⁻¹)
TiO ₂	0.0145	0.0034
N-TiO ₂	0.0185	0.0107
Er 5%-TiO ₂	0.0138	0.0086
Er 7.5%-TiO ₂	0.0124	0.0040
Er 10%-TiO ₂	0.0179	0.0112
Er 12.5%-TiO ₂	0.0151	0.0093

Table 28: Comparison of rate constants for the degradation of MIB using various thin films under UV and visible light

Film	Rate constant	Rate constant
	UV light	Visible light
	k_a (min ⁻¹)	k_a (min ⁻¹)
TiO ₂	0.0211	0.0098
N-TiO ₂	0.0221	0.0171
Er 5%-TiO ₂	0.0010	0.0004
Er 7.5%-TiO ₂	0.0014	0.0005
Er 10%-TiO ₂	0.0024	0.0007
Er 12.5%-TiO ₂	0.0004	0.0001

It has been reported by Lawton *et al* that decomposition of geosmin (10.98 nM) and MIB (11.90 nM) under UV irradiation (280W UV lamp source) and 1g of catalyst resulted in 100% degradation in 60 minutes at a rate of in 0.1979 and 0.0633 min⁻¹, respectively⁶⁶. Although the rate is faster than the rate in this study the amount of catalyst is substantially less as it is present as a 400.1nm - 425.1nm (0.000151-0.00016g) thick thin film on a 1cm² glass substrate. Additionally the concentration affects the rate of degradation and this study 2ppm was used equating to geosmin (10970 nM) and MIB (11885 nM) indicating that photocatalytic properties are exceptional. Furthermore, the decomposition of geosmin has been reported to be much faster than that of MIB under UV due to the greater steric hindrance, the decomposition rate in our study showed a slower decomposition rate for geosmin using the TiO₂ catalyst.

11.8 POSSIBLE DEGRADATION PATHWAY AND MECHANISM

As the degradation peaks were observed through GC-MS analysis, new peaks formed (perhaps intermediates in the reaction) or they could be the final degradation products of geosmin breaking down under UV light with TiO₂. These observed peaks are eluted at 6 and 7 minutes, and are identified as undecane and 2 ethyl hexanol. Geosmin appears at 11/12min and so after time with these peaks appearing the assumption is made that these are what geosmin is breaking down into:

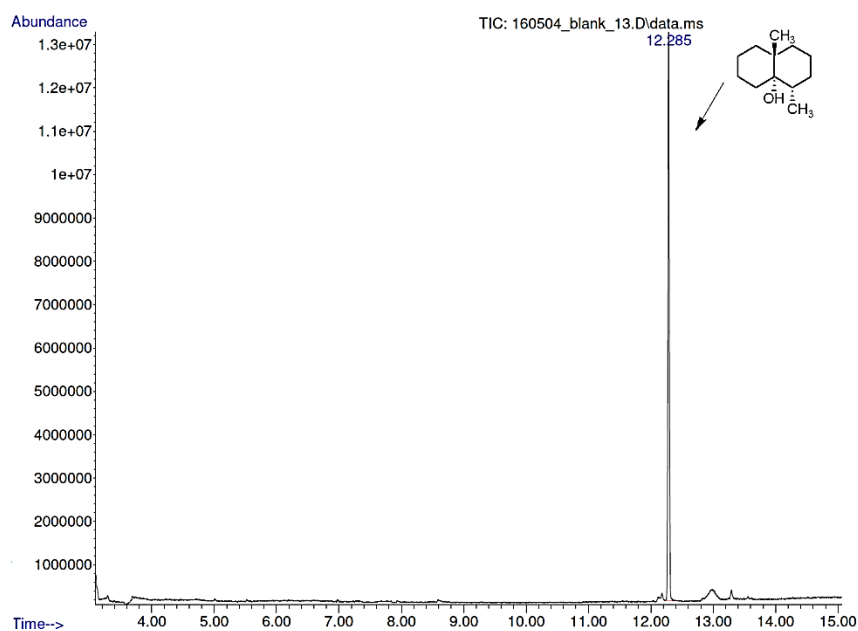


Figure 98: Chromatogram from GC-MS

There is a possibility that the observed peaks in Figure 99 are intermediates of a reaction rather than reaction products. As there are limited results into these it can be assumed they are products due to the short retention time of the two observed peaks.

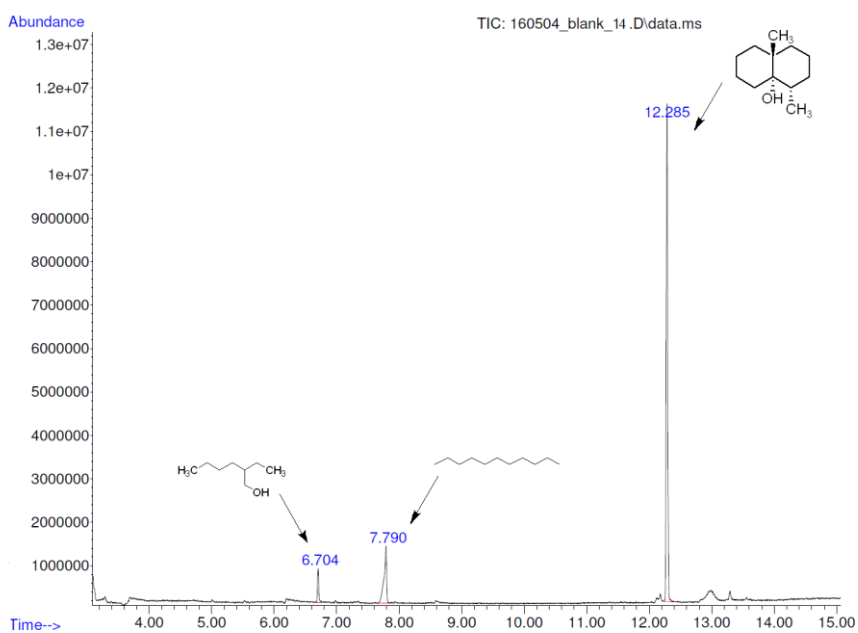


Figure 99: Chromatogram from GC-MS

The pathway presented (Figure 100) focuses on the GC-MS data obtained from this experiment and so does not include other possible degradation pathways or mechanisms.

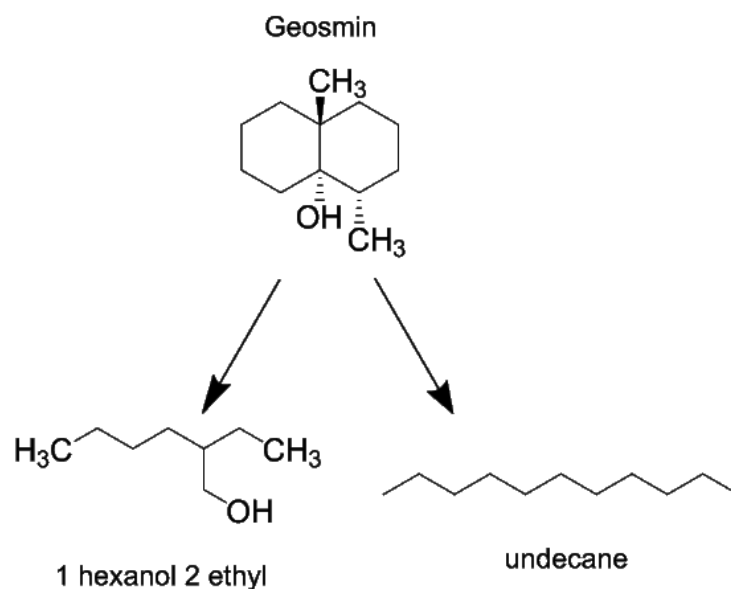


Figure 100: Breakdown products of geosmin observed from GC-MS analysis

MIB doesn't seem to form breakdown products, from the GC results the conclusion can be drawn that MIB takes part in a re-arrangement. Starting as 2-methylisoborneol and re-arranging to 2-methyleneborane and 2-methyl-2-borene. It is possible that the kinetics are influenced by Wagner–Meerwein rearrangement⁷¹ (Figure 101) of MIB which occurs in bicyclic terpenes¹¹⁷. This carbocation 1,2-rearrangement reaction in which a hydrogen, alkyl or aryl group migrates from one carbon to a neighbouring carbon and can be confirmed by GC-MS spectra.



Figure 102: Reservoir water sample before the treatment process

The water was then placed in the GC and the same method applied to the spiked lab geosmin samples was applied. As expected the chromatogram produced a spectrum with a wide variety of compounds present.

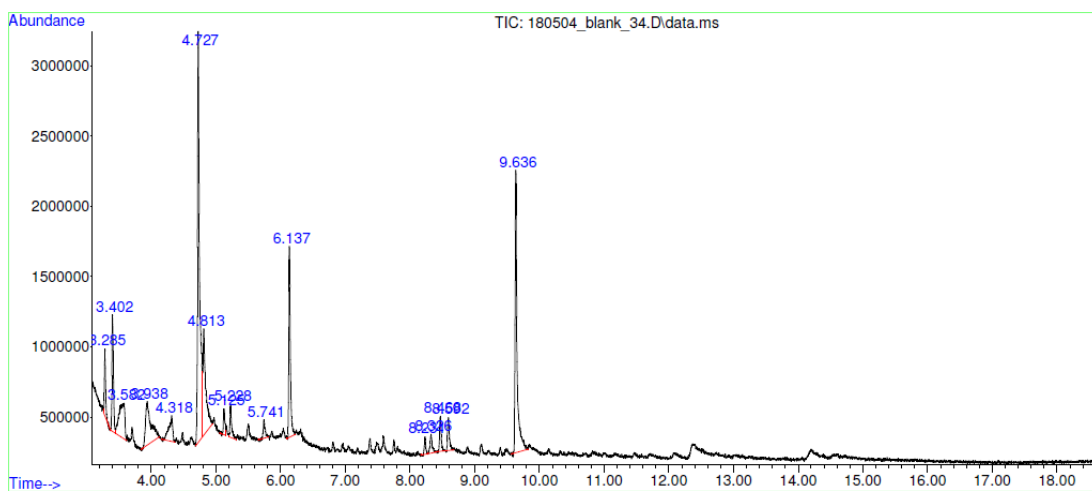


Figure 103: GC chromatogram for UU untreated water

Unfortunately, neither geosmin or MIB was identified in this sample. This could be due to the content of the taste and odour sample being below the limit of detection of this instrument or this particular sample could contain neither geosmin nor MIB.

11.10 CONCLUSION

Nitrogen doped titanium dioxide enabled degradation of two problem causing taste and odour compounds, geosmin and MIB. Degradation studies show 93% removal of geosmin under UV light and 80% removal of geosmin under visible light irradiation in 150 minutes. Although Er-TiO₂ compounds did degrade the compounds under both UV and visible light, N-TiO₂ proved more effective.

The concentration of the compounds affected the rate of degradation, this was found to increase with increasing concentration and when little concentration was used it was very hard to monitor the degradation, in order to repeat the tests with lower concentrations of the compounds present the GC-MS instrument used would need a better limit of detection.

The Langmuir adsorption isotherm is concentration dependent and so describes the decomposition of these compounds using TiO₂ well. Concentration therefore has a strong influence on the rate of destruction, this is important when considering future practical water treatment methods such as reactor design. There is promise for water treatment facilities to implement this technology, as N-TiO₂ have proved very successful in the degradation of both geosmin and MIB.

PART IV

CONCLUSIONS AND FUTURE WORK

This chapter contains a summary of the completed work and highlights conclusions of studies.

12.1 SUMMARY OF COMPLETED WORK

This thesis began with a summary of the taste and odour problem presented to water treatment companies. The relevant background material of possible treatment methods and detection techniques were investigated and ways to tackle this global problem was discussed.

In the approach adopted by this study, titanium dioxide was chosen as a photocatalytic material to degrade geosmin and MIB. It was therefore imperative to discuss the background of photocatalytic materials, including thin films and their deposition techniques. Titanium dioxide as a photocatalyst was discussed along with ways of improving the performance of the photocatalyst. Several ideas on how to implement this technology into the water industry arose along the way of the project, with some focus on using citrate functional nanoparticles to help the photocatalytic reaction by providing a plasmon boost effect. Unfortunately this area of the study presented many problems and was taken no further, however citrate functional nanoparticles (gold and silver) were successfully produced and tested for their fluorescent properties. The material chosen to degrade geosmin and MIB was titanium dioxide and therefore it was important to consider both nanoparticles and thin films in

this choice. TiO₂ nanoparticles were therefore successfully produced from a sol-gel method along with TiO₂ thin films from a magnetron sputtering technique. Highlights of the study also include successful doping of TiO₂ with nitrogen using magnetron sputtering via incorporation of nitrogen within the argon sputtering gas in the chamber, producing N-TiO₂ thin film. Adaptation of the magnetron method has led to doping of titanium dioxide thin films with molybdenum (Mo-TiO₂). A series of erbia doped titania (Er-TiO₂) thin films were deposited by powder magnetron sputtering method. Erbia powder precursor ranging from 5 to 12.5 % were used to dope the titania films. Full characterisation of all of the materials produced has led to quantifying the chemical composition of the thin films, band gap values, surface properties and crystalline phases present. The standard methylene blue test was used to study the photocatalytic performance of the thin films. A GC-MS method was developed in order to detect geosmin and MIB .Testing of the degradation of geosmin and MIB under visible and UV light using the photocatalysts was conducted and quantified using GC-MS.

12.2 OVERALL CONCLUSIONS

This project was undertaken in order to develop a material to breakdown geosmin and MIB in drinking water and to develop a method in order to test this breakdown. Geosmin and MIB alter consumer acceptability of drinking water due to their off-taste and can cause problems to drinking water treatment companies all over the world.

This study has led to a number of research findings. The development of methodology to quantify geosmin and MIB in a solution (using GC-MS) led to degradation experiments performed using a variety of photocatalysts, all produced via a magnetron sputtering technique. Er-TiO₂ thin films were successfully produced, and characterised. Raman spectroscopy showed that the films were not crystalline and the broad peak positions obtained corresponded to a mixture of anatase and brookite crystalline forms. XPS analysis revealed that erbium was present in the form of an oxide. The experiments demonstrated that geosmin and 2-MIB in aqueous solutions was successfully degraded under visible light (> 450 nm) using Er-TiO₂. The results demonstrate the feasibility of utilising the magnetron sputtering technique to grow films for industrial applications in new solar powered elimination technology for implementation in water treatment facilities

There was a distinctive shift of the absorption band in the N-TiO₂ to longer visible regions of the electromagnetic spectrum. Clear evidence of nitrogen incorporation was obtained from the XPS N 1s analysis with a concentration of 1% nitrogen doping calculated. The absorption band of the N-TiO₂ thin film was found to shift toward visible wavelengths, the corresponding band gap edge was calculated to be shifted to 3.14 eV from 3.20 eV consistent with substitutional N-doped anatase. The N-TiO₂ thin films were found to exhibit effective and efficient visible light photocatalytic activity for the liquid-phase degradation of geosmin at 80.2% and MIB at 90% after 150 min. From these results, it is clear that nitrogen-substituted TiO₂ thin films can be easily prepared by the magnetron sputtering method for industrial scale

up, for relatively cheap photocatalytic material production and implementation for possible water purification carried out under sunlight irradiation.

12.3 FUTURE WORK

The discovery that the best photocatalyst for the degradation of geosmin and MIB is a nitrogen doped titania material will prove influential to future studies, as it opens doors for new materials to be studied in a similar way. There is scope for improving the efficiency of the TiO₂ material, this can be done through either modification of the methods mentioned in this thesis, or creation of a new material.

Real samples of drinking water before and after treatment were secured from *united utilities* and tested using the method developed in this thesis but unfortunately, a GC with a better limit of detection is needed in order to test these samples using this method. Testing on a GC-MS with a better limit of detection would also allow for tests at much lower concentrations of geosmin and MIB. Samples obtained were from one reservoir only, and so subsequent measurements from a number of reservoirs would be required. An interesting way of developing the testing methods for geosmin and MIB would be to look into the effect of temperature on the proposed degradation reaction. For example looking into the possibility of this technology working better in hotter or colder climates.

1. T. C. Jagadale, S. P. Takale, R. S. Sonawane, H. M. Joshi, S. I. Patil, B. B. Kale and S. B. Ogale, *The Journal of Physical Chemistry C*, 2008, **112**, 14595-14602.
2. M. Lu and P. Pichat, *Photocatalysis and water purification: from fundamentals to recent applications*, John Wiley & Sons, 2013.
3. S. Sakuma, H. Amano and M. Ohkochi, *Journal of the American Society of Brewing Chemists*, 2000, **58**, 26-29.
4. C. Ng, J. N. Losso, W. E. Marshall and R. M. Rao, *Bioresource technology*, 2002, **85**, 131-135.
5. R. Robertson, A. Hammond, K. Jauncey, M. Beveridge and L. Lawton, *Aquaculture*, 2006, **259**, 153-163.
6. B. Zhou, R. Yuan, C. Shi, L. Yu, J. Gu and C. Zhang, *Journal of Environmental Sciences*, 2011, **23**, 816-823.
7. N. Gerber and H. Lechevalier, *Applied microbiology*, 1965, **13**, 935-938.
8. L. L. Medsker, D. Jenkins and J. F. Thomas, *Environmental Science & Technology*, 1968, **2**, 461-464.
9. R. Srinivasan and G. A. Sorial, *Journal of Environmental Sciences*, 2011, **23**, 1-13.

10. West Lake USA, Geosmin Report, www.westlake-tx.org/DocumentCenter/View/682.
11. J. L. Graham and K. A. Loftin, *CYANOBACTERIA IN LAKES AND 7.5 RESERVOIRS: TOXIN AND TASTE-AND-ODOR SAMPLING GUIDELINES*.
12. A. Wnorowski, *Water S. A.*, 1992, **18**, 203-214.
13. P. Piriou, R. Devesa, M. De Lalande and K. Glucina, *Journal of Water Supply: Research and Technology—AQUA*, 2009, **58**, 532-538.
14. B. Hurlburt, S. W. Lloyd and C. C. Grimm, *J Chromatogr Sci*, 2009, **47**, 670-673.
15. E. Oestman, L. Schweitzer, P. Tomboulian, A. Corado and I. Suffet, *Water Science & Technology*, 2004, **49**, 153-159.
16. E. Butakova, *Russian journal of plant physiology*, 2013, **60**, 507-510.
17. M. Yurkowski and J.-A. L. Tabachek, *Canadian Journal of Fisheries and Aquatic Sciences*, 1980, **37**, 1449-1450.
18. D. Bruce, P. Westerhoff and A. Brawley-Chesworth, *Aqua*, 2002, **51**, 183-198.
19. C. P. Dionigi, T. E. Lawlor, J. E. McFarland and P. B. Johnsen, *Water Research*, 1993, **27**, 1615-1618.
20. Sigma Aldrich, Geosmin MSDS, <http://www.sigmaaldrich.com/MSDS/MSDS/DisplayMSDSPage.do?country=GB&language=en&productNumber=717932&brand=ALDRICH&PageToG>

[oToURL=http%3A%2F%2Fwww.sigmaaldrich.com%2Fcatalog%2Fproduct%2Faldrich%2F717932%3Flang%3Den.](http://www.sigmaaldrich.com/catalog/product/aldrich/717932)

21. Sigma Aldrich, 2-methylisoborneol MSDS, <http://www.sigmaaldrich.com/MSDS/MSDS/PleaseWaitMSDSPage.do?language=&country=GB&brand=ALDRICH&productNumber=743364&PageToGoToURL=http%3A%2F%2Fwww.sigmaaldrich.com%2Fcatalog%2Fsearch%3Fterm%3D2-Methylisoborneol%26interface%3DProduct%2520Name%26N%3D0%2B%26mode%3Dmode%2520matchpartialmax%26lang%3Den%26region%3DGB%26focus%3DproductN%3D0%2520220003048%2520219853286%2520219853121>.
22. Institute of Environment and Health, *National assessment of the risks to water supplies posed by low taste and odour threshold compounds*, 2014.
23. G. C. Lee, Y. S. Kim, M. J. Kim, S. A. Oh, I. Choi, J. Choi, J. G. Park, C. K. Chong, Y. Y. Kim, K. Lee and C. H. Lee, *Water science and technology : a journal of the International Association on Water Pollution Research*, 2011, **63**, 2745-2751.
24. H. Marcussen, P. E. Holm and H. C. B. Hansen, *Comprehensive Reviews in Food Science and Food Safety*, 2013, **12**, 333-352.
25. H. Marcussen, P. E. Holm and H. C. Hansen, *Comprehensive Reviews in Food Science and Food Safety*, 2013, **12**, 333-352.

26. T.-F. Lin, J.-Y. Wong and H.-P. Kao, *Science of the Total Environment*, 2002, **289**, 225-235.
27. K. Meyer, R. Summers, P. Westerhoff and D. Wetz, Biofiltration for geosmin and MIB removal, 2005.
28. S. Watson, M. Charlton, Y. Rao, T. Howell, J. Ridal, B. Brownlee, C. Marvin and S. Millard, *Water Science & Technology*, 2007, **55**, 1-8.
29. V. H. Smith, J. Sieber-Denlinger, F. deNoyelles Jr, S. Campbell, S. Pan, S. J. Randtke, G. T. Blain and V. A. Strasser, *Lake and Reservoir Management*, 2002, **18**, 319-323.
30. W. D. Taylor, *Early warning and management of surface water taste-and-odor events*, Water Environment Research Foundation, 2006.
31. P. Omur-Ozbek, J. Little and A. Dietrich, *Water Science & Technology*, 2007, **55**, 249-256.
32. L. D. Tyler, T. E. Acree and R. M. Butts, *Journal of Agricultural and Food Chemistry*, 1978, **26**, 1415-1417.
33. R. Sävenhed, H. Borén and A. Grimvall, *Journal of Chromatography A*, 1985, **328**, 219-231.
34. M. J. McGuire, S. W. Krasner, C. J. Hwang and G. Izaguirre, *Journal (American Water Works Association)*, 1981, 530-537.

35. P. B. Johnsen and J.-C. W. Kuan, *Journal of Chromatography A*, 1987, **409**, 337-342.
36. J. Bartels, B. Brady and I. Suffet, *AWWA Res. Found*, 1989.
37. T. Kajino, *J. Japan Water Supply Association*, 1984, **53**.
38. S. W. Lloyd, J. M. Lea, P. V. Zimba and C. C. Grimm, *Water Research*, 1998, **32**, 2140-2146.
39. E. D. Conte, S. C. Conway, D. W. Miller and P. W. Perschbacher, *Water Research*, 1996, **30**, 2125-2127.
40. E. D. Conte, C.-Y. Shen, D. W. Miller and P. W. Perschbacher, *Analytical chemistry*, 1996, **68**, 2713-2716.
41. R. Eisert and K. Levsen, *Journal of Chromatography A*, 1996, **733**, 143-157.
42. K. Saito, K. Okamura and H. Kataoka, *Journal of Chromatography A*, 2008, **1186**, 434-437.
43. J. Chang, R. Biniakewitz and G. Harkey, *LC GC North America*, 2008, **40**, 24.
44. Agilent Technologies, Sensitive Detection of 2-MIB and Geosmin in drinking water, <http://www.chem.agilent.com/Library/applications/5991-1031EN.pdf>.
45. S. B. Watson, B. Brownlee, T. Satchwill and E. E. Hargesheimer, *Water Research*, 2000, **34**, 2818-2828.
46. X. Ma, N. Gao, B. Chen, Q. Li, Q. Zhang and G. Gu, *Frontiers of Environmental Science & Engineering in China*, 2007, **1**, 286-291.

47. National Environmental Methods Index,
https://www.nemi.gov/methods/method_summary/5720/.
48. C. online, <http://www.chromatographyonline.com/analysis-geosmin-and-2-methylisoborneol-mib-solid-phase-micro-extraction-spme-and-ci-ms-ms-using-var?id=&sk=&date=&%0A%09%09%09&pageID=2>.
49. Agilent technologies, Sub-ppt detection of geosmin and other odorants in drinking water with ion trap MS,
<http://www.chem.agilent.com/Library/flyers/Public/5991-0636EN.pdf>.
50. J.-F. Liu, Y. Tao, J. Sun and G.-B. Jiang, *Analytical Methods*, 2011, **3**, 696-702.
51. G. S. Braga, L. G. Paterno and F. J. Fonseca, *AIP Conference Proceedings*, 2011, **1362**, 287-288.
52. Edward Staples, Detection of 2-methylisoborneol and Geosmin in pond water,
http://www.estcal.com/tech_papers/papers/Environmental/Detection%20of%202-Methylisoborneol%20&%20Geosmin%20in%20Pond%20Water.pdf.
53. Watts and Crane Associates, *Desk Based Review of Current Knowledge on Pharmaceuticals in Drinking Water and Estimation of Potential Levels: Final Report to DWI (Defra Project Code: CSA 7184/WT02046/DWI70/2/213)*, Faringdon, UK, 2007.
54. L. Ho, D. Hoefel, F. Bock, C. P. Saint and G. Newcombe, *Chemosphere*, 2007, **66**, 2210-2218.

55. M. Antonopoulou, E. Evgenidou, D. Lambropoulou and I. Konstantinou, *Water research*, 2014, **53**, 215-234.
56. L. Ho, E. Sawade and G. Newcombe, *Water Research*, 2012, **46**, 1536-1548.
57. S. Suurnäkki, G. V. Gomez-Saez, A. Rantala-Ylinen, J. Jokela, D. P. Fewer and K. Sivonen, *Water Research*, 2015, **68**, 56-66.
58. P. Huck, S. Kenefick, S. Hrudey and S. Zhang, *Water Science and Technology*, 1995, **31**, 203-209.
59. L. Ho, E. Sawade and G. Newcombe, *Water Research*, 2012, **46**, 1536-1548.
60. K. Kutschera, H. Börnick and E. Worch, *Water research*, 2009, **43**, 2224-2232.
61. E. Rosenfeldt, K. Linden and B. Melcher, *Aqua*, 2005, **54**, 423-434.
62. TrojanUV, Taste and Odor Ontario case study, http://www.trojanuv.com/resources//casestudies/ECT/Taste_and_Odor_Treatment_Cornwall_Ontario_Case_Study_Environmental_Contaminant_Treatment.pdf.
63. M. Leach, A. Festger, A. Royce and C. Williamson, *IUVA News*, 2006, **8**, 11-16.
64. L. Lawton and P. J. Robertson, *Chemical Society Reviews*, 1999, **28**, 217-224.
65. M. N. Chong, B. Jin, C. W. Chow and C. Saint, *Water research*, 2010, **44**, 2997-3027.

66. L. A. Lawton, P. K. Robertson, R. F. Robertson and F. G. Bruce, *Applied Catalysis B: Environmental*, 2003, **44**, 9-13.
67. H. Tran, G. Evans, Y. Yan and A. Nguyen, Photocatalytic removal of Geosmin and MIB for drinking water treatment, 2009.
68. E. E. Bamuza-Pemu and E. Chirwa, *Water SA*, 2012, **38**, 689-696.
69. L. H. Wee, N. Janssens, J. Vercammen, L. Tamaraschi, L. C. Thomassen and J. A. Martens, *Journal of Materials Chemistry A*, 2015, **3**, 2258-2264.
70. W. Song and K. E. O'Shea, *Water research*, 2007, **41**, 2672-2678.
71. L. Birladeanu, *J. Chem. Educ*, 2000, **77**, 858.
72. A. O. Ibadon and P. Fitzpatrick, *Catalysts*, 2013, **3**, 189-218.
73. N. Dhiman, B. P. Singh and A. K. Gathania, *Journal of Nanophotonics*, 2012, **6**, 063511-063511-063511-063510.
74. T. Luttrell, S. Halpegamage, J. Tao, A. Kramer, E. Sutter and M. Batzill, *Scientific reports*, 2014, **4**.
75. A. Fujishima, T. N. Rao and D. A. Tryk, *Journal of Photochemistry and Photobiology C: Photochemistry Reviews*, 2000, **1**, 1-21.
76. U. I. Gaya and A. H. Abdullah, *Journal of Photochemistry and Photobiology C: Photochemistry Reviews*, 2008, **9**, 1-12.
77. A. Vidal, *Chemosphere*, 1998, **36**, 2593-2606.

78. V. Augugliaro, V. Loddo, G. Palmisano, M. Pagliaro and L. Palmisano, *Clean by light irradiation: Practical applications of supported TiO₂*, Royal Society of Chemistry, 2010.
79. K. Nakata and A. Fujishima, *Journal of Photochemistry and Photobiology C: Photochemistry Reviews*, 2012, **13**, 169-189.
80. C. Lettmann, K. Hildenbrand, H. Kisch, W. Macyk and W. F. Maier, *Applied Catalysis B: Environmental*, 2001, **32**, 215-227.
81. V. Štengl, S. Bakardjieva and N. Murafa, *Materials Chemistry and Physics*, 2009, **114**, 217-226.
82. A. Zaleska, *Recent Patents on Engineering*, 2008, **2**, 157-164.
83. P. J. Kelly, P. M. Barker, S. Ostovarpour, M. Ratova, G. T. West, I. Iordanova and J. W. Bradley, *Vacuum*, 2012, **86**, 1880-1882.
84. F. Peng, L. Cai, H. Yu, H. Wang and J. Yang, *Journal of Solid State Chemistry*, 2008, **181**, 130-136.
85. C. J. Tavares, S. M. Marques, T. Viseu, V. Teixeira, J. O. Carneiro, E. Alves, N. P. Barradas, F. Munnik, T. Girardeau and J.-P. Rivière, *Journal of Applied Physics*, 2009, **106**, -.
86. S.-M. Chiu, Z.-S. Chen, K.-Y. Yang, Y.-L. Hsu and D. Gan, *Journal of Materials Processing Technology*, 2007, **192–193**, 60-67.

87. S. Sakthivel, M. Janczarek and H. Kisch, *The Journal of Physical Chemistry B*, 2004, **108**, 19384-19387.
88. R. Asahi, T. Morikawa, T. Ohwaki, K. Aoki and Y. Taga, *science*, 2001, **293**, 269-271.
89. N. M. Nursam, X. Wang, J. Z. Tan and R. A. Caruso, *ACS applied materials & interfaces*, 2016, **8**, 17194-17204.
90. M. Ratova, G. West, P. Kelly, X. Xia and Y. Gao, *Vacuum*, 2015, **114**, 205-212.
91. D. Depla, S. Mahieu and J. Greene, in *Handbook of deposition technologies for films and coatings: science, applications and technology*, William Andrew, 2010, pp. 253-296.
92. M. Ratova, P. Kelly, G. West and I. Iordanova, *Surface and Coatings Technology*, 2013, **228**, S544-S549.
93. K. Wasa, M. Kitabatake and H. Adachi, *Thin film materials technology: sputtering of control compound materials*, Springer Science & Business Media, 2004.
94. H. Cui, J.-Z. Guo, N. Li and L.-J. Liu, *The Journal of Physical Chemistry C*, 2008, **112**, 11319-11323.
95. A. Farooq, R. Al-Jowder, R. Narayanaswamy, M. Azzawi, P. J. R. Roche and D. E. Whitehead, *Sensors and Actuators B: Chemical*, 2013, **183**, 230-238.

96. J. Qian, X. Li, M. Wei, X. Gao, Z. Xu and S. He, *Optics express*, 2008, **16**, 19568-19578.
97. J. Zhang, Y. Fu and J. R. Lakowicz, *The journal of physical chemistry C*, 2007, **111**, 50-56.
98. K. Awazu, M. Fujimaki, C. Rockstuhl, J. Tominaga, H. Murakami, Y. Ohki, N. Yoshida and T. Watanabe, *Journal of the American Chemical Society*, 2008, **130**, 1676-1680.
99. Y. Sun and Y. Xia, *Science*, 2002, **298**, 2176-2179.
100. M. Grzelczak, J. Pérez-Juste, P. Mulvaney and L. M. Liz-Marzán, *Chemical Society Reviews*, 2008, **37**, 1783-1791.
101. J. Turkevich, P. C. Stevenson and J. Hillier, *The Journal of Physical Chemistry*, 1953, **57**, 670-673.
102. J. Kimling, M. Maier, B. Okenve, V. Kotaidis, H. Ballot and A. Plech, *The Journal of Physical Chemistry B*, 2006, **110**, 15700-15707.
103. C. Graf, D. L. J. Vossen, A. Imhof and A. van Blaaderen, *Langmuir*, 2003, **19**, 6693-6700.
104. Z. S. Pillai and P. V. Kamat, *The Journal of Physical Chemistry B*, 2003, **108**, 945-951.
105. Y. Kobayashi, H. Katakami, E. Mine, D. Nagao, M. Konno and L. M. Liz-Marzán, *Journal of Colloid and Interface Science*, 2005, **283**, 392-396.

106. K. J. Qian, L. Zhang, M. L. Yang, P. G. He and Y. Z. Fang, *Chinese Journal of Chemistry*, 2004, **22**, 702-707.
107. S. Zheng, T. Wang, G. Xiang and C. Wang, *Vacuum*, 2001, **62**, 361-366.
108. P. J. Kelly, G. T. West, M. Ratova, L. Fisher, S. Ostovarpour and J. Verran, *Molecules*, 2014, **19**, 16327-16348.
109. Z. Y. Banyamin, P. J. Kelly, G. West and J. Boardman, *Coatings*, 2014, **4**, 732-746.
110. T. Marino, M. Boerrigter, M. Faccini, C. Chaumette, L. Arockiasamy, J. Bundschuh and A. Figoli, *Application of Nanotechnology in Membranes for Water Treatment*, 2017, 127.
111. M. Ratova, Manchester Metropolitan University, 2013.
112. I. M. Clegg, N. J. Everall, B. King, H. Melvin and C. Norton, *Applied Spectroscopy*, 2001, **55**, 1138-1150.
113. H. Tang, K. Prasad, R. Sanjines, P. Schmid and F. Levy, *Journal of applied physics*, 1994, **75**, 2042-2047.
114. S.-Y. Chen, C.-C. Ting and W.-F. Hsieh, *Thin Solid Films*, 2003, **434**, 171-177.
115. R. Pecora, *Dynamic light scattering: applications of photon correlation spectroscopy*, Springer Science & Business Media, 1985.

116. J. Tauc, R. Grigorovici and A. Vancu, *physica status solidi (b)*, 1966, **15**, 627-637.
117. A. Schiffrin, Y. Khatri, P. Kirsch, V. Thiel, S. Schulz and R. Bernhardt, *Organic & biomolecular chemistry*, 2016, **14**, 3385-3393.
118. P. Aktiv, <https://www.pilkington.com/en-gb/uk/householders/types-of-glass/self-cleaning-glass>.
119. Gas chromatography mass spectrometry schematic, https://chem.libretexts.org/Core/Analytical_Chemistry/Instrumental_Analysis/Chromatography/Gas_Chromatography.
120. A. Moses Ezhil Raj, V. Agnes, V. Bena Jothy and C. Sanjeeviraja, *Materials Science in Semiconductor Processing*, 2010, **13**, 389-394.
121. M. Kitano, K. Funatsu, M. Matsuoka, M. Ueshima and M. Anpo, *The Journal of Physical Chemistry B*, 2006, **110**, 25266-25272.
122. J. Rodriguez, M. Gomez, S.-E. Lindquist and C. Granqvist, *Thin Solid Films*, 2000, **360**, 250-255.
123. T. Ohsaka, F. Izumi and Y. Fujiki, *Journal of Raman spectroscopy*, 1978, **7**, 321-324.
124. M. Sathish, B. Viswanathan, R. Viswanath and C. S. Gopinath, *Chemistry of materials*, 2005, **17**, 6349-6353.

125. N. C. Saha and H. G. Tompkins, *Journal of Applied Physics*, 1992, **72**, 3072-3079.
126. C. W. Dunnill and I. P. Parkin, *Dalton Transactions*, 2011, **40**, 1635-1640.
127. X. Chen and C. Burda, *The Journal of Physical Chemistry B*, 2004, **108**, 15446-15449.
128. R. L. Johnston, *Atomic and molecular clusters*, CRC Press, 2002.
129. H. Tran, G. M. Evans, Y. Yan and A. V. Nguyen, *Chemeca 2008: Towards a Sustainable Australasia*, 2008, 696.